TECHNISCHE UNIVERSITÄT MÜNCHEN

Lehrstuhl für Nanoelektronik

Nanoimprinting Techniques for Polymeric Electronic Devices

Anandi Yadav

Vollständiger Abdruck der von der Fakultät für Elektrotechnik und Informationstechnik der Technischen Universität München zur Erlangung des akademischen Grades eines

Doktor-Ingenieurs

genehmigten Dissertation.

Vorsitzender:		Univ.-Prof. Dr. techn., Dr. h. c. Josef A. Nossek
Prüfer der Dissertation:	1.	Univ.-Prof. Paolo Lugli, Ph.D.
	2.	Prof. Dr. rer. nat. Wolfgang Porod University of Notre Dame, Indiana/USA

Die Dissertation wurde am 07.05.2014 bei der Technischen Universität München eingereicht und durch die Fakultät für Elektrotechnik und Informationstechnik am 28.09.2014 angenommen.

To my mother, Renu Yadav

my father, D. K. Yadav

and my brother, Shyam Yadav

Thank you for your unconditional love, encouragement and patience.

Abstract

In keeping with changing times and the increasing demand for miniaturization, technological advances have been made in every field which has generated a vast interest among researchers. When it comes to semiconductor fabrication, the current technique used at the industrial scale is photolithography for its ability to go down into the nanometer scale and its cost effectiveness when being compared to electron beam lithography (EBL). The disadvantage of photolithography is that its components are limited by the wavelength of light. The work of this thesis deals with another fabrication technique called Nanoimprint lithography (NIL). It is a low cost, high throughput fabrication technique which is viable on an industrial level for large scale production without having to deal with the disadvantages of the other techniques. It has numerous applications ranging from electrical, magnetic to optical. This thesis aims at demonstrating that NIL can and should be used as an alternative to other lithographic techniques by focusing on various applications just mentioned above. NIL is used in conjunction with Nanomagnetic Logic (NML) circuits as one of the main technologies for the future. It is also shown to aid in the growth of nanowires for electrical applications. Fabricating metallic grating structures for device efficiency and patterning extremely hard organic polymers are another of the many utilizations of NIL. Lastly, NIL is shown to be used with metasurfaces to fabricate quasi 3D double layer nanoantenna structures for an application of a polarization rotator. These are just a few of the many ways in which NIL can be utilized making it a fabrication technique to be reckoned with and implemented industrially for large scale production.

Table of Contents

1. Introduction **1**

1.1 Aim of the thesis 3

2. Nanoimprint Lithography and Nanotransfer Printing **5**

2.1 Photolithography 5

2.2 Moore's Law 7

2.3 Nanoimprint Lithography 9

2.3.1 Working Principle of NIL 10

2.4 Important Parameters for NIL 12

2.5 Types of NIL 15

2.6 Defect Control In NIL 17

2.7 Nanotransfer Printing 20

2.7.1 Working principle of nTP 20

2.7.2 NIL vs. nTP 20

3. NIL for Nanomagnetic Logic **23**

3.1 Introduction 24

3.1.1 Nanomagnetic Logic 24

3.1.2 Magnetic Material 26

3.1.3 Anisotropy 26

3.2 Fabrication Process 26

3.2.1 NIL and Lift-off 27

3.2.2 Electrodeposition 29

3.2.3 Nanotransfer and Electrodeposition 34

3.3 Results and Discussion 37

3.3.1 Focused Ion Beam Cutting........38
3.4 Summary........40

4. NIL for Nanowire Growth........41
4.1 Introduction........42
4.2 Fabrication of NWs using NIL and MBE........42
4.3 Results and Discussion........48
4.3.1 HRXRD Measurement........48
4.3.2 Raman Spectroscopy........51
4.3.3 Photoluminescence........52
4.4 Summary........53

5. NIL for Plasmonic Devices........55
5.1 Introduction........56
5.2 Device Stack........57
5.3 Fabrication........57
5.4 Results and Discussion........63
5.4.1 Simulation Results........63
5.4.2 Experimental Results........73
5.5 Summary........79

6. NIL for Organic Optoelectronic Devices........81
6.1 Introduction........81
6.2 PEDOT:PSS........82
6.2.1 Glycerol Doped PEDOT:PSS........84
6.3 Materials........85
6.3.1 Substrate........85
6.3.2 PEDOT:PSS........85
6.3.3 NIL Thermal Resist........86
6.3.4 Master Mold........86

6.3.5 PDMS 86
6.4 Fabrication 87
6.4.1 Stamp Preparation 87
6.4.1.1 Replica Molding 87
6.4.1.2 PDMS Dilution with Solvent 91
6.4.1.3 h-PDMS Stamp Replication 94
6.4.2 Problems faced during the use of PDMS/h-PDMS 96
6.4.3 Stamp Surface Modification 97
6.5 Results and Discussion 98
6.5.1 Direct Imprints with Si Stamps 98
6.5.1.1 Imprints on Silicon 98
6.5.1.2 Imprints on Glass 99
6.5.1.3 Imprints on Quartz Wafers 100
6.5.1.4 Imprints on G-PEDOT:PSS on Quartz Wafers 101
6.5.2 Improved NIL Process on Quartz Substrates 102
6.5.3 Soft Lithography 105
6.5.3.1 Soft Lithography using DVD Stamp 107
6.5.3.2 Soft Lithography with Nanometer Structures in PDMS 107
6.5.3.3 Soft Lithography with h-PDMS Stamps 109
6.5.3.4 Soft Lithography with Thermal Imprint Polymer 109
6.6 Characterization 110
6.6.1 Sheet Resistance Measurements 110
6.6.1 Transmission Measurements 113
6.7 Summary 113

7. NIL for Metasurfaces 115
7.1 Introduction 116
7.2 Fabrication Methods 118
7.3 Results and Discussion 124
7.4 Summary and Outlook 127

8. Conclusion and Outlook **129**

8.1 Conclusion 129

8.2 Outlook 130

References **133**

Publications **145**

Acknowledgement **147**

Chapter 1

Introduction

When we talk of semiconductor fabrication, the foremost words that come to mind are lithography, patterning, mask etc. There are various methods which are available and used today for lithography. One of the techniques which is widely prevalent commercially today is photolithography or optical lithography. As the name suggests, this process uses light to transfer the pattern of a mask onto the substrate using chemical processes [1]. There are a number of steps involved in this which will be discussed later on in the next chapter. Another technique is the Electron Beam Lithography (EBL) which uses a focused beam of electrons to pattern a surface covered with electron sensitive film [2].

With time, there has been an increasing interest in developing new methods for semiconductor manufacturing which could be industrially viable. This thesis focuses on using one such method for patterning called as Nanoimprint Lithography (NIL). Unfortunately this technique has not been commercially accepted on a large scale yet and therefore, the purpose of this research is to highlight the advantages of NIL over other fabrication techniques. The outcome achieved by all the patterning methods are similar in nature and differ in the actual process steps involved. Nanoimprint Lithography has been used as the core technology to fabricate nanostructures for various applications in this thesis.

1 INTRODUCTION

By using NIL, we want to put forth another fabrication technique in the market which boasts of various advantages over the conventional techniques so far. Another fabrication technique called as Nanotransfer Printing (nTP) has also been used in certain cases. As mentioned earlier, EBL is another commonly used fabrication tool these days but there are certain disadvantages to it which are not present in NIL [3, 4]. EBL is a slow process with very high costs of the machine and writing time. On the other hand, NIL is a high throughput, low cost technique meant for large area fabrication of structures. It is an industrially viable process with high precision and this thesis focuses on using NIL over EBL.

A lot of work has already been done on NIL and using it for a lot of applications mainly to show its large scale patterning advantage [5, 6]. There are 3 main applications mentioned in this work which are electrical, magnetic and optical.

The chapters in this thesis are defined as follows:

Chapter 2 gives details of NIL and nTP with regards to the principle of working, important factors which contribute to them and brief history. The various types of imprint technologies are also discussed in detail with another section focusing on the disadvantages and defect control in NIL.

Chapter 3 discusses about Nano Magnetic Logic (NML) and using NIL to fabricate nanostructures which are magnetic in nature and to show coupling between them. The fabrication steps of producing metal nanopillars are shown which are used as a seeding layer or base for another process step called as electrodeposition. The aim is to deposit a magnetic material on top of the metal nanopillars in order to show coupling between them using a magnetic force microscope. Apart from nanopillars, nanolines are also used as structures for electrodeposition. A Focused Ion Beam (FIB) is used to cut the electrodeposited nanolines in oval shapes such that the magnet has clearly defined opposite poles.

Chapter 4 presents how NIL is used to fabricate and grow Indium Arsenide nanowires as opposed to using Molecular Beam Epitaxy (MBE). This chapter focuses on the advantage of NIL used for large scale, periodic growth of the nanowires as compared to the random self assembled growth by MBE. HRXRD, Raman spectroscopy and photoluminescence measurements are performed to characterize the nanowires grown via these two methods.

Chapter 5 focuses on depicting NIL as a tool for making optoelectronic devices. A basic schematic of an organic photodetector (OPD) is shown with the aim of patterning its lowest layer with metal gratings. Optical properties of this patterned layer are measured in terms of transmittance and reflectance. Simulations are also performed to correlate the obtained results from the experimental data. In order to confirm the results, different dimensions are used of the nanostructures for making the metal gratings and the metal coverage over the gratings explained.

Chapter 6 moves onto the next layer in the device stack of the OPD to the organic polymer layer. This chapter deals with pure fabrication in terms of patterning the organic PEDOT:PSS layer using NIL. It gives details of the fabrication process, the different techniques of imprinting involved, the problems and challenges faced in the project as well sums up a new technique developed to pattern the otherwise hard PEDOT:PSS layer.

Chapter 7 details using metasurfaces in conjunction with NIL for a potential optical application in terms of a polarization rotator. Metamaterials are explained briefly at first after which the working principle of a conventional polarization rotator is described. NIL is factored in the process of generating a metallic double layer 'C' shaped antenna structure which is shown to have coupling between the nanostructures. The fabrication details consist of using EBL as well as NIL for the project. Fourier Transform Infrared (FTIR) measurements are done to observe the optical phenomena over a broad range of the spectrum.

Chapter 8 gives a conclusion to the various projects undertaken in this thesis and a possible future outlook. Each project is summarized with the main objectives and results. The future outlook describes certain improvements to the current processes used in the thesis with the focus on optimizing the parameters and using NIL for further applications as have been done already.

1.1 Aim of the thesis

The constant need for miniaturization in today's world has led to the innovation of various lithographic techniques. Starting from optical lithography, e-beam lithography to imprint lithography, all forms try and reduce the size of the interconnects required on a chip in one way or another.

1 INTRODUCTION

Within imprint lithography, there are two variations again: step and flash imprint lithography and nanoimprint lithography. Step and flash imprint lithography always makes use of a transparent mold which is pressed onto a polymer coated substrate and UV light is shined on top to harden the polymer around the structures. It differs from nanoimprint lithography in the polymer dispensing technique. In step and flash imprint lithography the polymer is dispensed in a customized pattern matching the template using a drop pattern generator whereas in NIL, the polymer is typically spin coated on top. Step and flash imprint lithography also takes place at room temperature and low pressure whereas NIL generally requires high temperatures [36].

Nanoimprint lithography is one of the relatively more recent lithographic techniques with possible feature sizes down to 10nm and less. The aim of this thesis is to investigate the various applications that NIL can be used for and to promote NIL for industrially viable processes considering its advantages. The applications aimed at in this thesis are:

- Magnetic: Fabrication of nanomagnetic logic components using NIL
- Electrical: Nanowire growth on homogeneously patterned substrates using NIL
- Optical: Metasurface fabrication using NIL
- Optoelectronic: Fabrication of sub wavelength grating structures for possible plasmonic applications using NIL

There are numerous other applications pertaining to NIL but this thesis focuses only on the above mentioned four. The main objective is to experimentally prove that fabrication of nanostructures for the listed applications is possible and more viable with NIL as compared to other lithographic techniques and that these structures can further be used for analysis and measurements.

Chapter 2

Nanoimprint Lithography and Nanotransfer Printing

This chapter is an introduction to the core technology used in this research work- NIL. In the first part of the chapter we will talk about NIL in detail-its working process as well as some of the important factors that affect NIL. The second part will focus on another similar technology called the Nanotransfer Printing (nTP) and its basic concepts.

2.1 Photolithography

Before we move onto discuss NIL and nTP and their working principle, let us take a look into the most conventional form of lithography being used today in industries which is photolithography. As mentioned before, photolithography involves using light to transfer the pattern on a mask onto a substrate coated with light sensitive resist or polymer. The basic steps involved in the entire steps are explained as follows:

Cleaning

The substrates usually silicon are first cleaned by going through a standard cleaning procedure called the RCA clean which is a solution of hydrogen peroxide and ammonium hydroxide. This step is done to remove any organic or inorganic contaminants which may be on the surface of the substrates before starting any further processing on them.

Preparation

The wafers are first heated to remove any moisture they may have after cleaning. They are then coated with a gaseous or liquid adhesion promoter such as Bis(trimethylsilyl)amine ("hexamethyldisilazane", HMDS) to improve the adhesion of the resist to the surface of the substrate.

Photoresist coating

The wafers are coated with the resist by spin coating where the resist is dispensed onto the surface and spun rapidly to form a uniform layer. They are spun from 1200 to 4800 rpm for 30 to 60 seconds which results in a thickness of about 0.5 to 2.5 micrometers. The coated wafer is then prebaked to remove any excess solvent at a temperature of 90 to 100 degrees for 30 to 60 seconds.

Exposure and Developing

After prebaking, the substrate is exposed to light through a chrome mask which contains the desired pattern to be transferred to the substrate. The light causes a reaction in the resist which allows some of the resist to dissolve or be removed in a developer solution. Positive photoresist, the most common, becomes soluble in developer when exposed to light whereas in the negative photoresist, the unexposed areas become soluble. The resulting wafers are then hard baked usually at a temperature of 120 to 180 degrees for 20 to 30 minutes.

Etching

Etching refers to removing the uppermost layer of substrate in areas where there is no photoresist. For etching, a chemical (wet) or plasma (dry) is used to remove the layer. in semiconductor fabrication, usually dry etching is used as it offers the advantage of anisotropy to avoid the undercuts in the photoresist pattern.

Photoresist removal

After etching, the photoresist is removed as it is no longer needed. This is done by dipping it in something called as a resist stripper which reacts with the resist in such a way that it no longer adheres to the substrate.

Figure 2.1 depicts the schematic involved in a standard photolithography process.

Photolithography is the most commonly used fabrication technique used in the industry but it also has certain limitations. Due to the dependence on light, photolithography is limited by the wavelength of light. Firstly, the cost involved in photolithography for the optical tool is very high. Optical lithography is dependent on excimer lasers and requires stacks of high precision ground lens to achieve nanometer scale resolution. The cost of a nanoimprint tool is a one time cost bringing the overall expenditure on NIL extremely low as compared to photolithography. NIL also does not need any high powered optics or specific tailored resists designed for resolution and sensitivity at a given wavelength. A broader range of materials with varying properties are available for use with NIL. The throughout in NIL is higher as many wafers can be printed with a single stamp over a large area and the time required is also very low as compared to optical lithography. These are some of the benefits of NIL over photolithography which make it a commercially more viable option.

2.2 Moore's Law

One of the most important factors to promote micro and nanotechnology is the ability to successfully fabricate such structures in a scalable environment and at the same time be industrially viable. Gordon Moore [7] gave a statistical prediction in 1965 that the number of components per integrated function would exponentially increase with time. He co-founded Intel in 1968 and the term "Moore's Law" was coined in 1970 which became the backbone for all semiconductor research that followed. Figure 2.2 shows Moore's prediction [7].

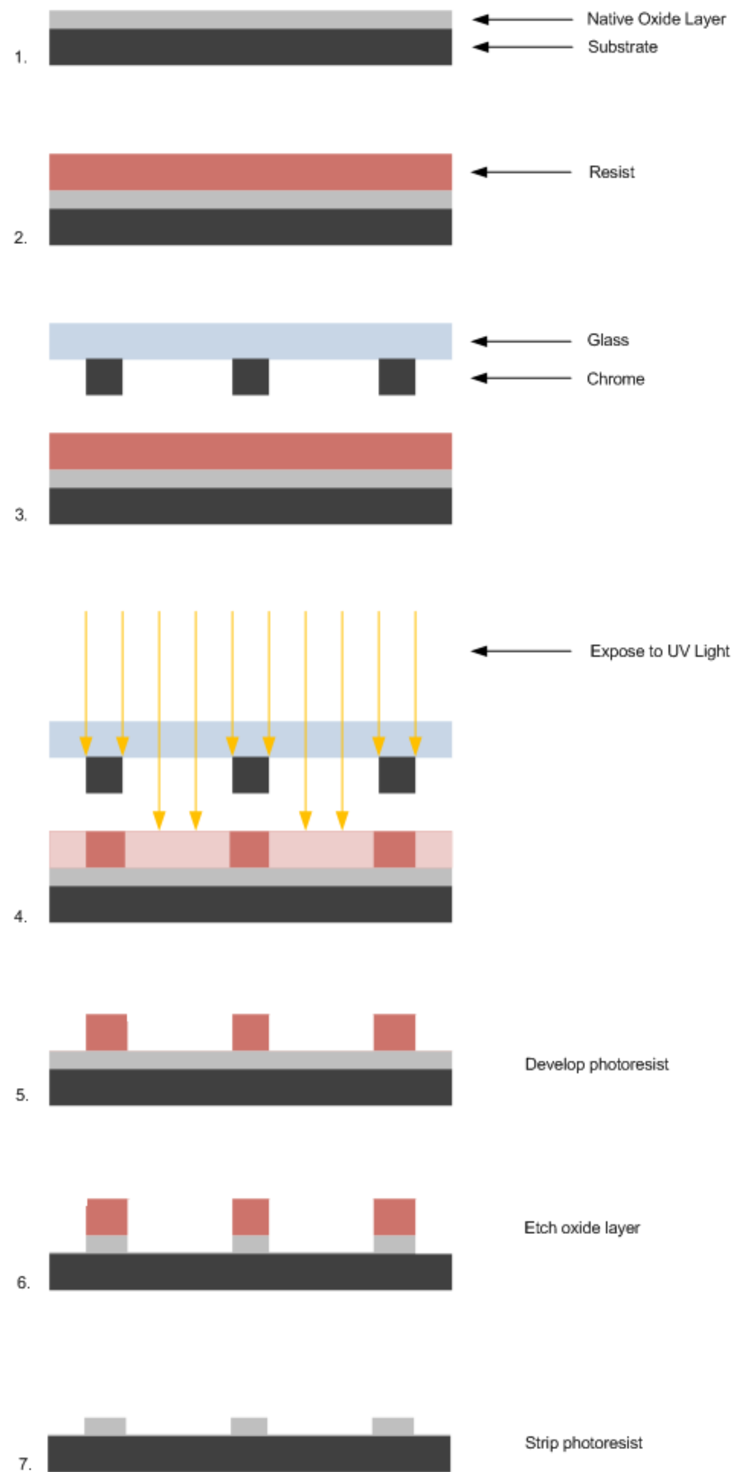

Figure 2.1 Schematic of a photolithography process showing 1) the substrate and oxide layer 2) the resist spin coated on the substrate 3) the alignment of the chrome mask 4) exposure with UV light 5) resist development 6) etching the oxide layer and 7) stripping the photoresist.

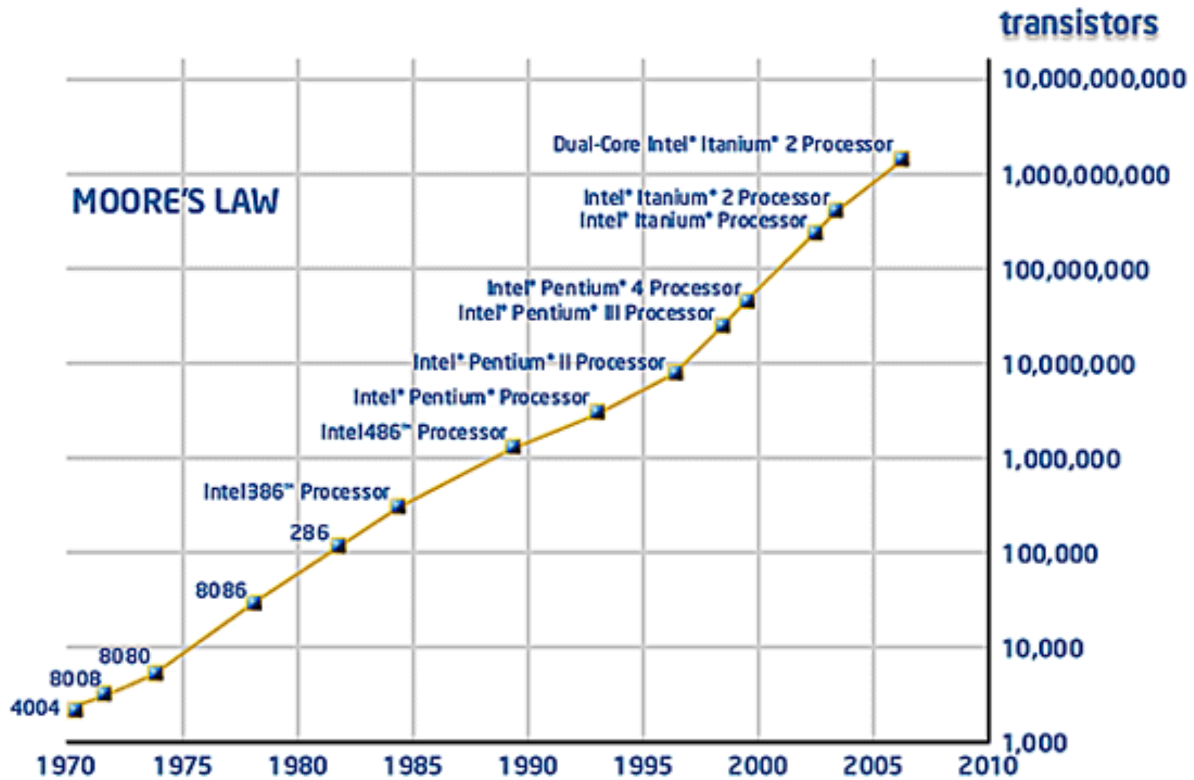

Figure 2.2 Moore's Law

The key factor to keep up with Moore's law was miniaturization. In order to increase the number of components on an IC, the size of the transistor had to be scaled down. The scaling had to be done in an industrially viable process therefore, keeping the costs low, with a high throughput and high precision were some of the other important factors to keep in mind. Optical lithography was on the forefront of semiconductor fabrication earlier as a commercial process but with time miniaturization became an issue due to scaling down of transistors. Thus, it was increasingly difficult to stick to optical lithography as the standard tool due to its physical limitations. As mentioned in the International Technology Roadmap for Semiconductors, NIL fulfilled the requirements of scalability [8].

2.3 Nanoimprint Lithography

Nanoimprint Lithography (NIL), first introduced by Chou et. al., [9, 10] represents one of most promising lithographic techniques with high throughput and low cost for

patterning nanostructures reproducibly. In contrast to photolithographic techniques, the achievable resolution of NIL is not limited by diffraction. It is a parallel process which is more suitable and has an advantage over the sequential electron beam lithographic processes which can also achieve similar resolutions. Over the years, NIL has been used for making nanostructures for various applications [11, 12].

L.J. Guo is another pioneer in the field of NIL and has demonstrated many aspects of it in his work [13]. The definition of NIL as given by Guo is as follows:

"Nanoimprint Lithography (NIL) is a non-conventional lithographic technique for high throughput patterning of polymer nanostructures at great precision and at low costs".

2.3.1 Working Principle of NIL

The working principle of NIL is very simple and relies on reproducing the topography of a mold which has micro/nano surface relief structures onto a polymer or resist. It can be thought of as a simple hot embossing technique used in the olden days where the impression of the mold was left in hot wax. Here the hot wax can be thought of as the resist which is heated to a certain temperature.

In the case of NIL, a mold with micro or nano structures is pressed into a polymer spin coated onto a substrate. A controlled temperature and pressure is maintained such that the polymer flows into the protrusions of the structures on the mold [14, 15, 16]. This creates a negative impression of the mold into the polymer. After the process is completed, the mold is removed from the substrate. This is called demolding. Typically, a thin layer of polymer called as the residual layer is left behind between the imprinted polymer and the substrate. For most applications, this layer is removed by reactive ion etching to complete the process of pattern transfer. Further work involves steps of metal deposition etc. Fig 2.3 shows the basic schematic of NIL.

Most imprints presented here are preformed in a commercially available state-of-the-art 2.5" NIL tool (Obducat, Sweden). The imprints presented in chapter 5 are performed in a commercially available "air cushion" enabled NIL tool NX-2000 (Nanonex Corporation, USA). As can be seen from the schematic, mold and substrate is stacked together with the polymer facing the structures. The smaller of the two goes on the top to avoid any undue damage caused by applying pressure to the stack. The mold and substrate is covered with aluminum foils in order to evenly displace the pressure. This stack is then heated above the glass transition temperature of the polymer T_g at which the polymer starts flowing into the structures of the mold [17, 18].

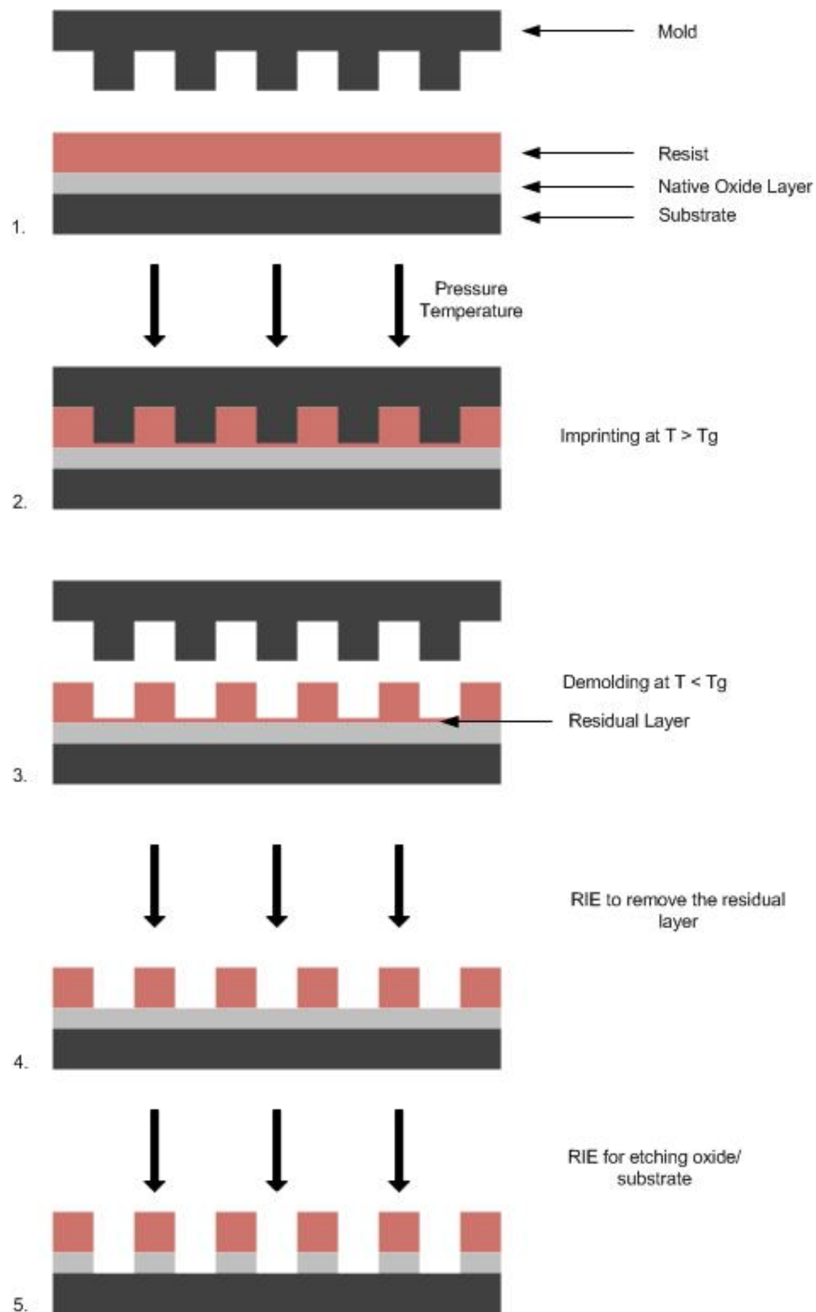

Figure 2.3: Working principle of NIL showing 1) the basic components 2) the imprint process under the conditions of temperature and pressure 3) demolding step resulting in a residual layer 4) RIE to remove the residual layer followed by 5) RIE to remove the oxide layer in order to etch the substrate.

After heating, a constant pressure is applied to the stack for a certain time for the imprint to happen. Once the imprint is done, the stack is cooled down below T_g in order to harden the polymer around the structures of the mold while maintaining the same pressure as before [19, 20]. Then the mold is removed from the substrate leaving the imprint behind in the polymer.

In comparison to Optical Lithography, the expensive light source and mask used there is replaced by a simple heat and pressure source and an imprint mold. The mold although expensive to manufacture is still cheaper than the light source used in Optical Lithography.

2.4 Important Parameters for NIL

This section details the important factors that affect the NIL process and their functioning. There are 3 basic types of NIL- thermal, UV and roll-to-roll depending on the type of resist and substrate used. These will be discussed in the next section.

2.4.1 Imprint Mold

The most common imprint molds are made out of Silicon or certain metals like Nickel. These are generally used for Thermal NIL. In case of UV-NIL, molds made out of Quartz are generally used since they are transparent. Quartz molds can also be used for thermal imprints.

Imprint molds are fabricated by e-beam lithography (EBL). The required pattern is written onto the resist by a focused beam of electrons. The pattern is etched into silicon by following the standard process of developing it first and then dry etching it. The way a mold is designed is very crucial to the imprint process. The structures should be fabricated in the center of the mold proceeding outwards such that when the pressure is applied during the imprint it is distributed evenly all over the mold. It is also beneficial to have some dummy structures or markers along the outer edges of the active structures for better grip between the mold and substrate. The different kinds of mold used in this thesis will be detailed in the coming chapters.

2.4.2 Imprint Resist

The imprint resist plays an important role in printing the structures of the mold into the substrate. There are different kinds of resists being used depending on the type of NIL which will be mentioned as they are used in the next chapters.

The mold structures get transferred to the substrate under heat and pressure treatment but the transfer also depends on another factor called the Glass Transition Temperature of the resist T_g. The T_g as the name suggests is the temperature above which the resist goes through a transition in its state from solid to viscous. The solid state is referred to as the glass state where the molecules of the resist are closely packed together and cannot move around. The resist in the glass state is hard and brittle. Above the Glass Transition Temperature, the molecules are mobile and the resist is viscous such that it can flow around freely into the structures of the mold.

The following physical properties undergo a drastic change at the T_g of any resist:

a) hardness

b) volume

c) Young's modulus

d) percent elongation-to-break

Figure 2.4 shows the dependence of the properties of the resist on temperature.

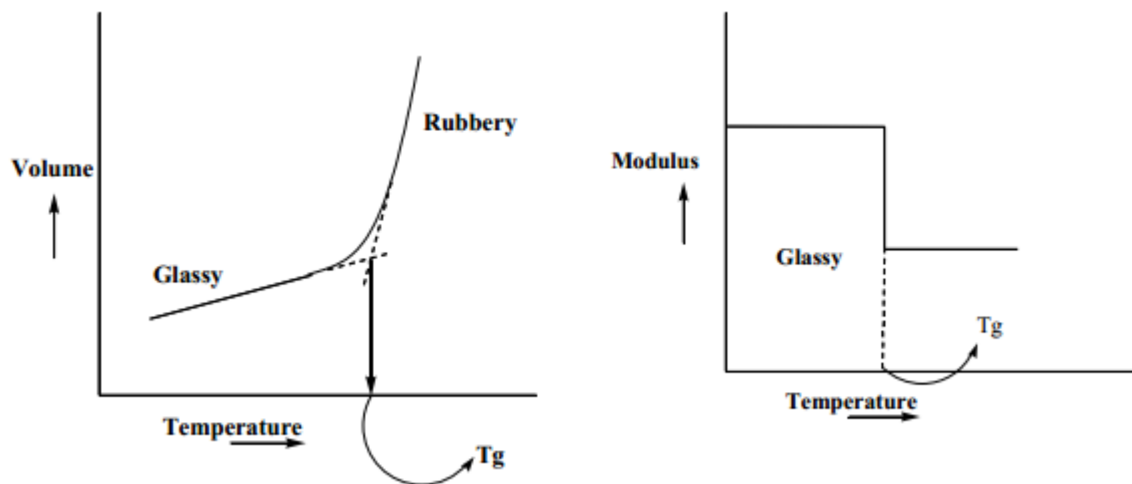

Figure 2.4: Change in various properties of a resist depending on the Glass Transition Temperature (T_g)

The Young's modulus E may be written as:

$$\sigma = E\varepsilon$$

$\sigma =$ Tensile stress; $\varepsilon =$ Tensile strain

Young's modulus is a fundamental measure of the stiffness of the material. The higher its value, the more resistant the material is to being stretched.

NIL is highly dependent on T_g. It is performed by heating the resist above the T_g to make it less viscous such that it flows into the trenches and in between structures of the mold. Before demolding, the resist is cooled down below the T_g so that the resist hardens around the structures of the mold and keeps the form of the mold.

The T_g of most thermal resists is between 100-130° C whereas for UV-NIL the T_g is around room temperature.

2.4.3 Adhesive Forces

The adhesive forces between the different components such as the substrate, mold and resist play an important role in the demolding process of NIL. The forces between the substrate and resist naturally have to be stronger than the forces between the mold and resist so that during demolding the resist does not come off and stick to the mold and damage the structures on the mold.

To reduce the adhesive forces between the resist and mold, an anti sticking layer is used on the mold. It is a self assembled monolayer of fluorocarbons to make the surface of the mold hydrophobic [21].

Apart from this, molds made of generally hydrophobic materials can also be used for NIL. Surface treatment of substrates and molds is an important factor in the imprint process. [22, 23, 24]

2.4.4 Residual Layer

After the imprint process is complete, there is always some polymer left behind between the imprinted resist and the substrate. This is called as the residual layer. Even if the resist thickness is lesser than the height of the structures on the mold, there will still be some residual layer left behind. This is due to the confinement of a liquid between two solid spaces which leads to a liquid to glass transition [25]. This layer is generally a minimum of 5 – 10 nm in height [26].

This residual layer is removed for further processes usually by Reactive Ion Etching (RIE). The uniformity of this layer is very important for homogenous etching or removal of the layer. However, due to uneven imprint or mold heights, the residual layer thickness can vary.

2.5 Types of NIL

This section will focus on the three different types of NIL which in turn depends on the type of resist being used.

2.5.1 Thermal NIL

Thermal NIL is the same as the general working principle explained before. In this case, the resist is heated to above the Glass Transition Temperature (T_g) to make it less viscous so that it flows into the structures of the mold. A constant pressure is maintained for a particular duration of time for the imprint to take place. Before demolding, the temperature of the resist is decreased to below the T_g to harden the resist around the structures of the mold and retain the shape. As the name suggests, heat is the major factor in this type of imprint. Figure 2.3 shows the basic working principle of thermal imprint.

2.5.2 UV-NIL

In the case of UV-NIL, the general working principle is the same as thermal NIL but for the difference of exposing the resist to UV light. After the heat and pressure treatment, the resist is exposed to UV light which hardens it thereby curing the resist before demolding. The mold in this case is transparent generally made of Quartz because UV light has to be shined through the mold to expose the resist.

The temperature in UV-NIL is kept lower than in thermal NIL and is around room temperature. Therefore, UV-NIL finds its advantages in imprints where high temperatures may damage the structures to be patterned such as DNA etc. Since the mold is transparent, UV-NIL is also appropriate for alignment purposes. Figure 2.5 shows the basic working principle of UV-NIL.

2.5.3 Roll-to-Roll NIL

This is the most commercial type of NIL used for imprinting flexible or rigid substrates. The concept is similar to how newspapers are printed. Roll-to-Roll NIL incorporates the high throughput and large area factor which is very crucial for commercial purposes. It

combines all the steps of thermal NIL in an assembly line manner for high speed manufacturing [27, 28]. Figure 2.6 shows the two different types of Roll-to-Roll NIL used for flexible as well as rigid substrates.

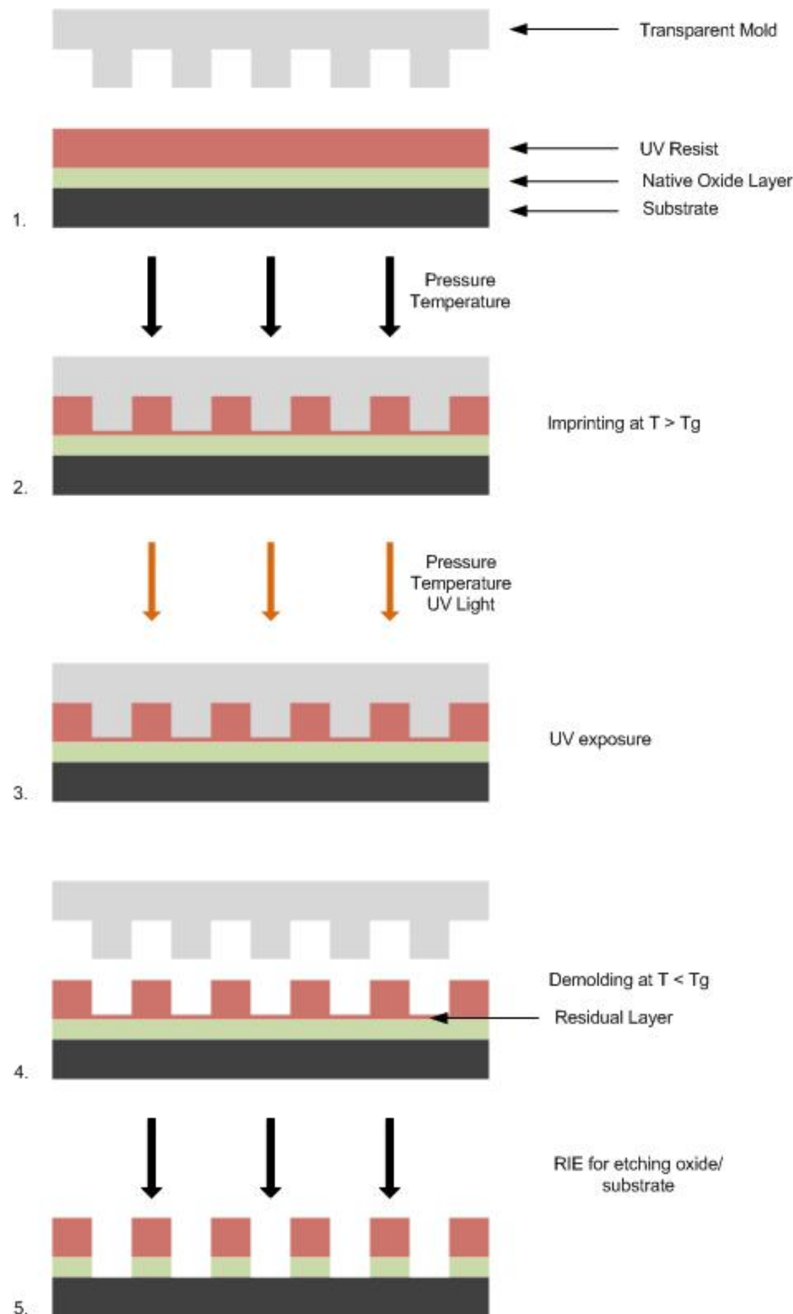

Figure 2.5: Working principle of UV NIL showing 1) various components including a transparent mold 2) imprint process under conditions of temperature and pressure followed by 3) exposure to UV light to cure the resist 4) demolding process leaving behind a residual layer and finally 5) RIE to etch away the oxide and substrate.

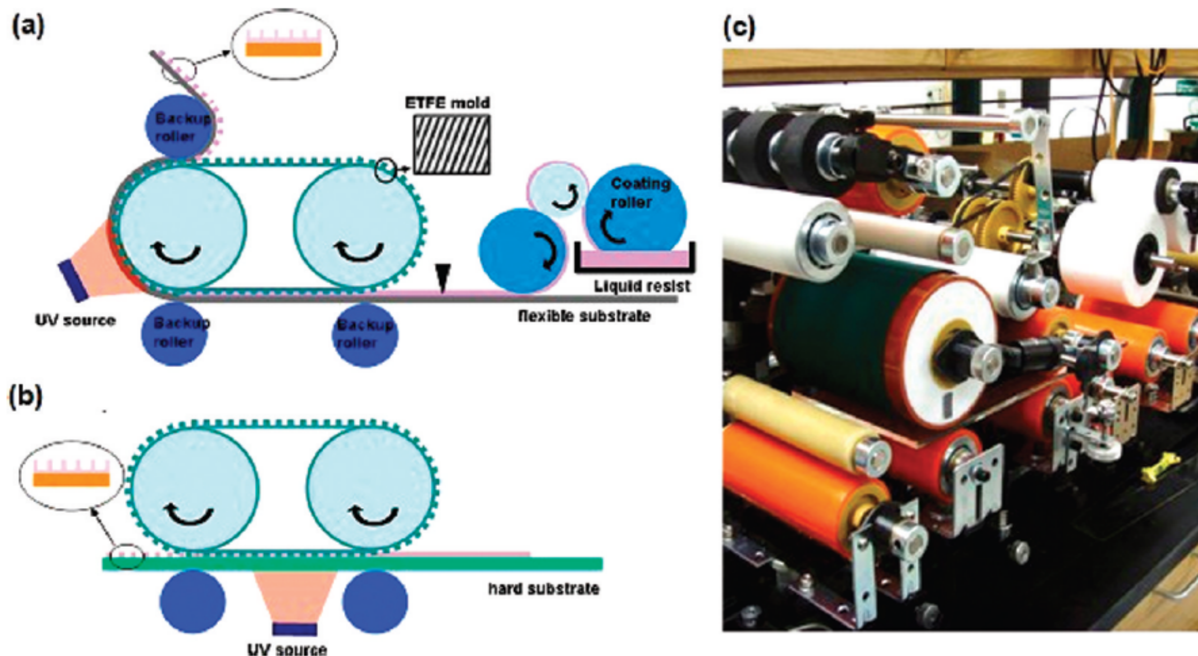

Figure 2.6: Schematics of (a) R2RNIL and (b) R2PNIL process (c) Photograph of 6 inch capable R2R/R2PNIL apparatus [29].

2.6 Defect Control in NIL

As with all the technologies, NIL also brings us many challenges, such as imprint pressure uniformity, large area mold separation, multiplayer NIL alignment and defect issues. In fact, defects have been one of the biggest obstacles for NIL to be the real nanofabrication tool in the industry. In NIL, defects can be roughly divided into two groups: random defects and repeatedly occurring ones. Repeated defects include the existing defects on the mold and substrate which are repeated in every process and imprint. Randomly distributed defects include particles, incomplete contact during imprint and the residual layer after imprints which are not repeatable in terms of area and amount [30].

2.6.1 Particle associated Defect

A particle associated defect is generally a particle amplified defect as it constitutes the particle itself, the void area surrounding the particle and the polymer incomplete filled area. The size of the impact is related to the particle size, hardness, substrate and mold stiffness, applied pressure and polymer surface properties. In order to clean the particles from the surface of the mold, a dry deep clean process was developed. Figure

2.7 shows the process details. A polymer adhesive is formulated which is spin coated on a flat surface such as a Silicon wafer to form a thin film. The formed polymer film is sticky to the particle, deformable under the pressure and releasable from the mold. The film can be squeezed into the trenches of the nanostructures to do the deep clean. It is a non destructive process which can be applied to any kind of particle or surface. The deep clean is also a room temperature process therefore it does not require thermal heating or UV curing and it is also repeatable according to the needs.

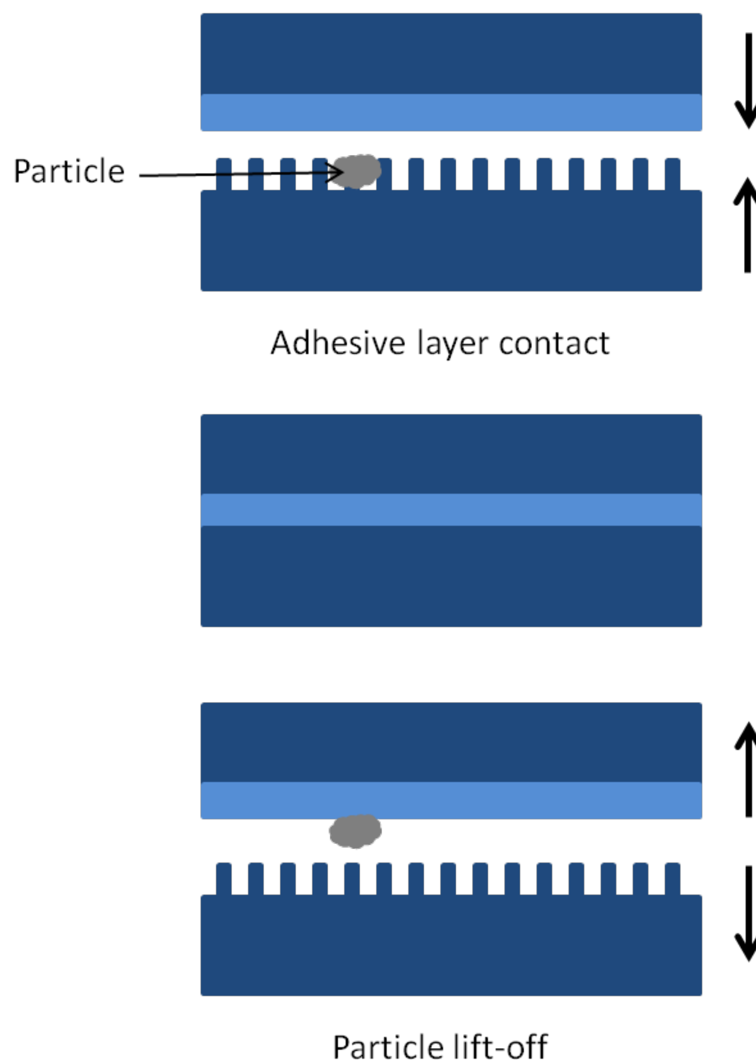

Figure 2.7: Dry Deep Clean (DDC) process; a) Adhesive layer coating b) Mounting c) Particle lift-off.

2.6.2 Gap Associated Defect

There is another common defect called the gap associated defect which as the name suggests is related with the gap between the mold and resist during the process. It is generated by wafer/mold irregularities or bad process control such as vacuum or pressure. Gap associated defects do not have a clear boundary but are normally incomplete pattern structures with variable sizes. The incomplete pattern structures are due to the polymer shortage when filling between the mold and substrate. According to previous studies, the surface charge on the mold tends to pull the polymer up, if not contacted, to form unique polymer patterns [31]. The interesting part is when the gap between the polymer and the mold surface is controlled, the 'defects' induced by the gap are regular polymer arrays [32].

Generally wafer/mold flatness and the pressure to flatten the wafers are out of control. Wafers can bow up or down to a certain degree by the wafer type or the coating on top. For example, wafer bowing could be 10μm on bare glass, but increased to over 100μm after SiN coating. To calculate the force to flatten the wafer bowing, a limiting case of Roark's formula is used,

$$q = \frac{yEt^3}{3a^4(1-v^2)[\frac{3+v}{8(1+v)} - \frac{1}{16}]}$$

where uniform pressure q bends a dished or bowed area of radius a. The predicted relationship between the maximum deflection y and q is considered to be accurate when the maximum deflection is not more than half the wafer thickness, and the transverse dimensions (of order a) are at least four times the wafer thickness. For typical wafer dimensions this means that the model is expected to be accurate for dished regions as small as 2mm in radius.

According to the above equation, the pressure required to flatten a dished region varies inversely with the fourth power of the radius of the region. So while it is easy to flatten the wafer scale bow, flattening smaller irregularities in the wafer becomes rapidly more difficult.

To a fixed gap between mold and substrate, the polymer resist filling rate depends on the substrate/mold surface tension, resist surface tension, viscosity etc. Generally, increasing the surface tension of the fluid and solid surfaces maximizes the rate of fill.

The rate of fluid displacement during the capillary fill is inversely proportional to the viscosity of the fluid.

However, for the NIL resist, its surface tension is usually low in order to realize the mold separation after the imprint. Therefore, viscosity becomes an important parameter to adjust during the material development. Low viscosity is preferred to avoid gap associated defects.

2.7 Nanotransfer Printing

We have discussed Nanoimprint lithography and important factors related to it in terms of parameters and defects in detail in the earlier sections. We know that in conventional NIL, a mold is pressed into a substrate coated with resist and under pressure and temperature the features of the mold are imprinted into the resist. In this section we will discuss about another similar lithographic technique called as nanotransfer printing (nTP).

2.7.1 Working Principle of Nanotransfer Printing

Nanotransfer printing is analogous to stamping on paper where the stamp can be thought of as the mold and the paper is the substrate. Nanotransfer printing is a two phase concept consisting of inking and stamping. During the inking step, a thin film of metal is evaporated over the stamp. Note that the metal film gets structured according to the contours of the stamp. The stamping step consists of pressing down the mold onto a substrate under temperature and pressure such that the metal film detaches itself from the mold and gets transferred onto the substrate. Before metal deposition on the mold, it is treated with an anti sticking layer such that the metal films can come off easily from the mold. The substrate on the other hand is treated with oxygen plasma to make it more adhesive. After the required metal is deposited on the mold, a very thin layer of Titanium or Chrome is evaporated on top. This is an adhesive layer which helps in the contact process of the mold and the substrate when they are brought together. Other adhesive treatments are also used in different experiments which help us understand the nanotransfer process [33, 34, 35]. Figure 2.8 depicts the schematic of nanotransfer printing.

2.7.2 NIL vs. nTP

The basic difference between NIL and nTP is that there is no need for a polymer in the nanotransfer printing process. The eventual step of having metallic structures on the

substrate after imprinting and subsequent lift-off is produced in the nanotransfer printing step by directly depositing metal films onto the desired structured mold. Therefore the additional step of spin coating a polymer and imprinting onto a polymer is removed. Nanotransfer printing is also a dry process which does not require any etching as there is no polymer involved therefore, there is nothing to etch.

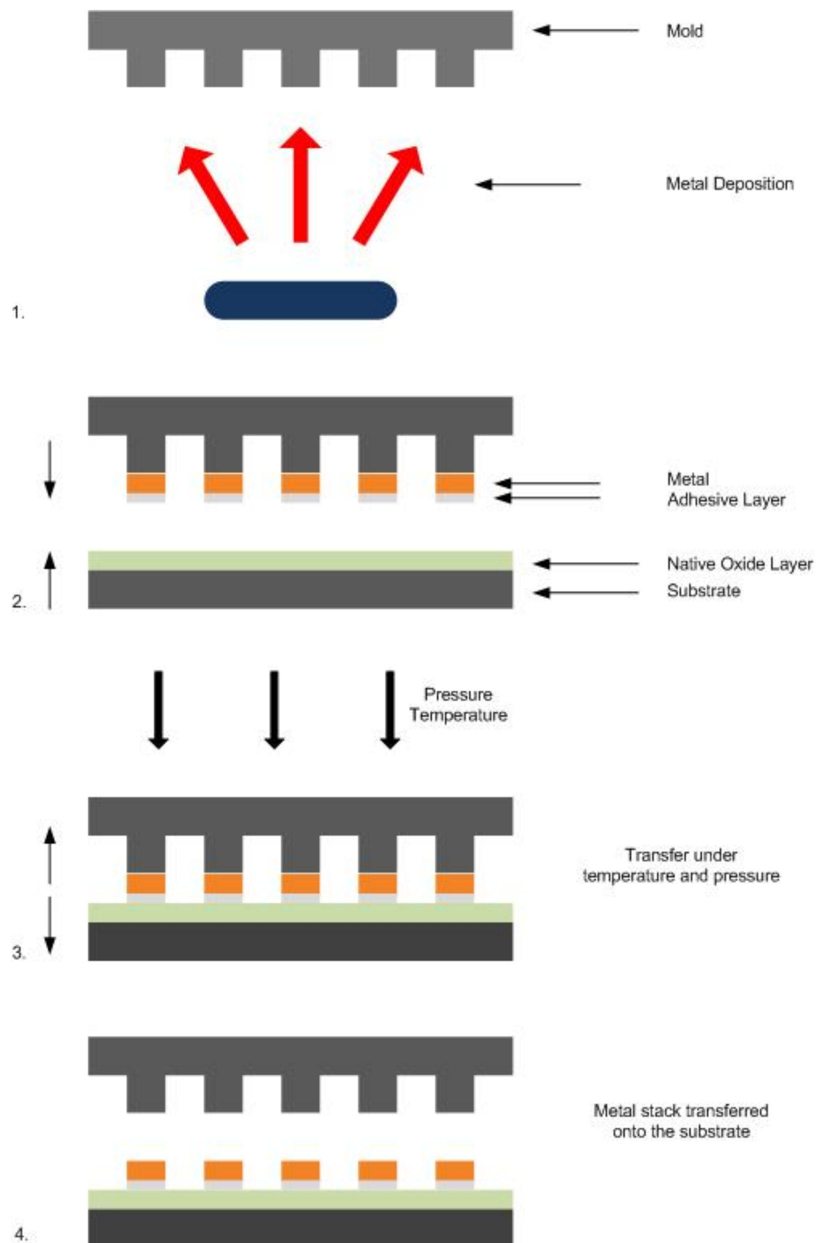

Figure 2.8: Schematic of nanotransfer printing depicting 1) metal deposition on mold 2) mold and substrate after surface treatment and deposition 3) nanotransfer process under temperature and pressure 4) demolding step with the metal stack transferred onto the substrate.

Chapter 3

NIL for Nanomagnetic Logic

In this chapter we talk about using Nanoimprint Lithography as a technique for fabricating Nanomagnetic Logic (NML) structures and to show coupling between them. Magnetic Quantum dot Cellular Automata (MQCA) is based on the interaction between magnetic nanoparticles. The term “Quantum” refers to the quantum-mechanical nature of magnetic exchange interactions and not to the electron-tunneling effects [37]. Nanomagnetic Logic is a derivative of this MQCA. A lot of work has been done on the simulation[38, 39, 40] and fabrication[41, 42] of NML circuits as they are one of the many alternative technologies proposed as a replacement solution to the fundamental limits CMOS technology will impose in the years to come[43, 44]. The work in this chapter is inspired from the PhD research done by Csaba [45] and Imre [46] on simulations and fabrication respectively. The results presented here are part of the PhD research of Muhammd Atyab Imtaar.

3.1 Introduction

Due to reasons such as increasing switching speeds, increasing complexity and decreasing power consumption, all which are consequences of miniaturization of devices, CMOS technology has been the industry standard for implementing Very Large Scale Integrated (VLSI) devices for the last two decades. As stated above, MQCA is one of the alternative technologies to replace the CMOS technology as it has the advantage of power efficiency and can incorporate both memory and logic. This chapter focuses on how we fabricate such metal magnetic nanostructures using nanoimprint lithography and electrodeposition. Gold nanostructures are fabricated using NIL and act as a seeding layer for electrodeposition wherein another magnetic material is deposited onto the gold structures. This novel process has many applications in Nanomagnetic Logic circuits as well as surface enhanced electro chemistry. Both NIL and electrodeposition are industrially viable processes for large scale fabrication. We fabricate nanopillars and nanolines using this technique which are then analyzed using an Atomic Force Microscope (AFM) for the topography and Scanning Electron Microscopy (SEM). A Magnetic Force Microscope (MFM) is used to measure the magnetic properties of the structures. To understand further about magnetic structures we need to first understand how these magnets work, what are their different states, the type of material used for fabrication and a few other aspects related to NML which are discussed below.

3.1.1 Nanomagnetic Logic

Before we proceed further to talk about magnetic materials and various important factors to keep in mind regarding magnets, we should have a basic understanding of how magnets work. Nanomagnetic logic is based on magnetic interaction between the two different poles of a magnet. It is common knowledge that like poles repel each other and unlike poles attract. Now there are two basic states of a magnet which need to be kept in mind when discussing magnets. We will talk about a simple case of using bar magnets to understand how the different poles behave around one another. If we keep two bar magnets both of whose north poles are pointing in the same direction, then they are said to be in an unstable state also called as ferromagnetic coupling where the two magnets repel each other. Now if we were to place the magnets in such a way that their north poles are pointing in opposite directions from each other then this state is called as the stable state of a magnet or anti-ferromagnetic coupling where the two magnets attract each other[47].

For all logical operations, the magnets are supposed to be in their stable state. If they are not so then an external field is applied to put these magnets in their stable state. In another scenario, if there are more than two magnets placed next to each other such that each pole of a magnet is placed in an opposite direction from that of its neighbor, then we have something called as a nanowire. In order to orient the magnets in a stable state, there is usually an input magnet placed horizontally at the beginning of the nanowire. According to this input wire's state, all the other magnets orient themselves in an anti-ferromagnetic coupling. Figure 3.1 depicts the two states of a magnet as well as a nanowire.

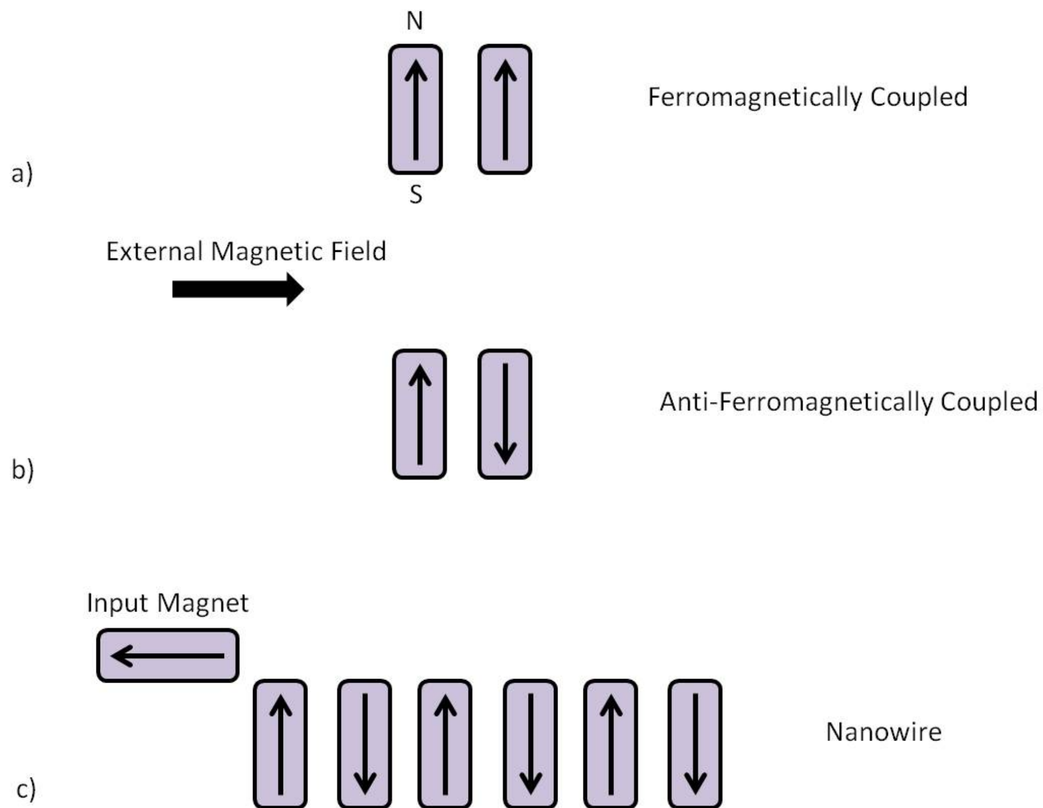

Figure 3.1 a) Ferromagnetically coupled magnets with the two poles pointing in the same direction b) Anti-ferromagnetically coupled magnets with the two poles oriented in opposite directions with the help of an external field and c) a nanowire with the input magnet deciding the orientation of the other magnets.

3.1.2 Magnetic Material

There are two types of magnetizations that exist for doing logical operations-in plane and out of plane magnetization. The materials used for both types are also different. Permalloy (80% Ni, 20% Fe) is used for in plane magnetization and a CoPt multilayer stack is used for out of plane magnetization. In our experiments we deal with in plane magnetization therefore, we use Permalloy.

3.1.3 Anisotropy

In plane magnetization has a characteristic of shape anisotropy which means that the direction of magnetization is decided by the shape of the magnet. The shape needs to be asymmetric in case of permalloy. The longer length is called the easy axis and the shorter length is called the hard axis. It is obvious that the hard axis needs a stronger magnetic field to magnetize as compared to the easy axis.

3.2 Fabrication Process

The fabrication of the metal nanostructures starts with a highly doped p-type Si substrate coated with a thermal resist which is imprinted upon using NIL. After lift-off, the metal nanostructures act as the seeding layer for electrodeposition of a further magnetic layer which selectively deposits over the gold nanopillars and nanolines where the substrate is the electrical contact to the gold cathode. Since the nanolines are too long to show any coupling effect in an MFM, we use the Focused Ion Beam (FIB) to cut the nanolines into small rectangles which can be imaged easily and show coupling.

EBL is the most commonly used technique for fabrication as such but it is slow and costly as compared to our combined technique of NIL and electrodeposition.

The basic schematic of the fabrication process is illustrated in figure 3.2.

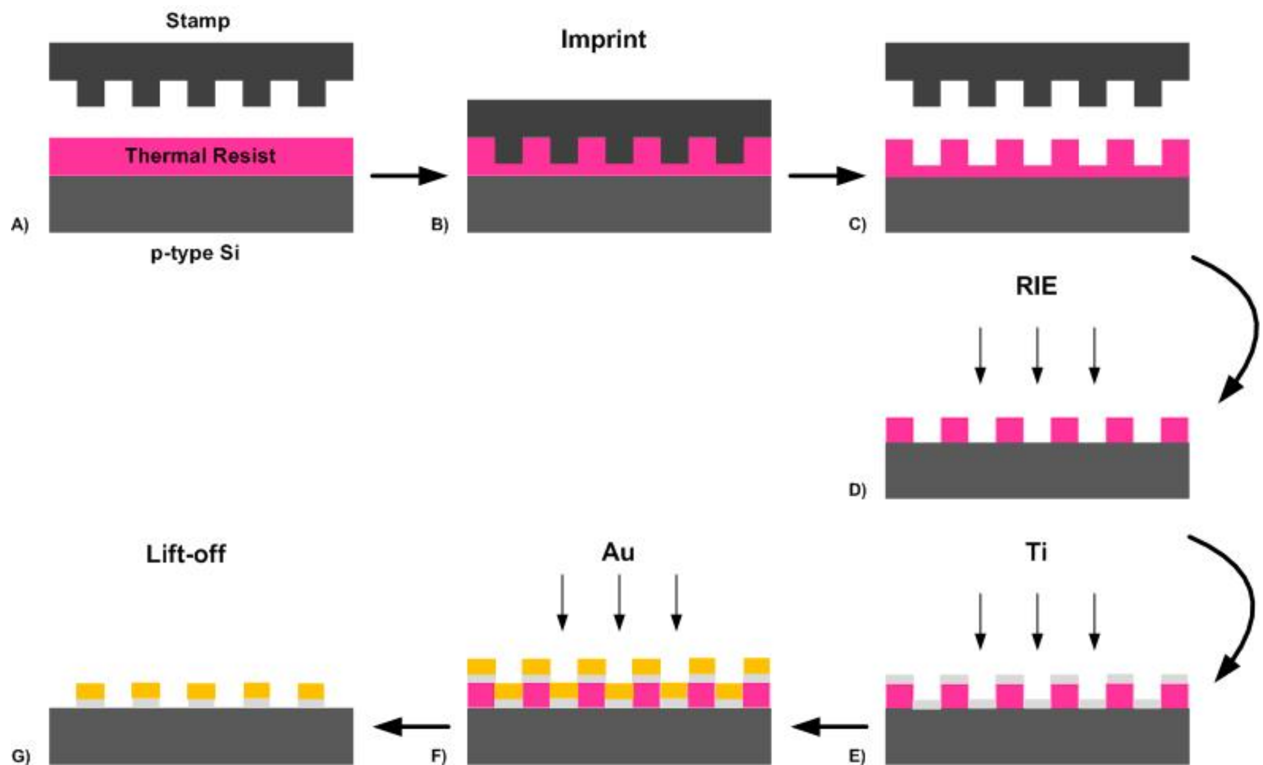

Figure 3.2 Schematic of the steps involved in fabricating metal nanostructures via NIL; A) highly doped p-type wafer coated with a thermal resist B) imprint step C) demolding of the stamp from the substrate D) reactive ion etching to remove the residual layer E) thermal deposition of Ti F) and Au G) resulting in final metal structures after lift-off.

3.2.1 Nanoimprint Lithography & Lift-off

We use two silicon stamps for the imprint each with a different structure. One consists of pillars with a diameter of 60 nm and a pitch of 240 nm over an area of 8 mm x 8 mm. The other consists of lines with a width of 60 nm and again a pitch of 240 nm covering an area of 12 mm x 6 mm. The height of the structures on the stamp is approximately 90nm. These stamps were fabricated by IMS Stuttgart, Germany. The thermal imprint resist used in our case is the mrI 8010R bought from Microresist, Germany which has a spin coated height of approximately 100nm. Figure 3.3 shows the images of the two stamps with the pillars and lines. A two inch highly doped p-type silicon wafer (boron doped to 1018 cm^3) is used as the substrate. The reason for this is explained in the next sections. For the actual imprint a commercially available Obducat 2.5" Nanoimprinter bought from Obducat, Sweden is used.

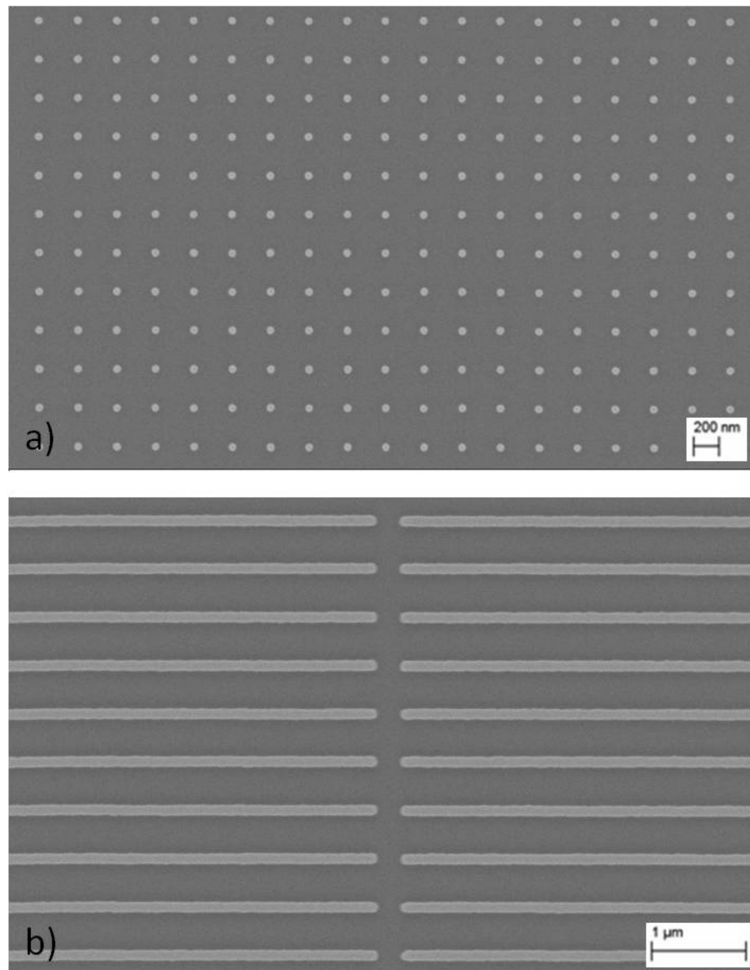

Figure 3.3 SEM images showing a) pillar stamp with a diameter of 60 nm and pitch of 240 nm and b) lines stamp with a diameter of 60 nm and pitch of 240 nm.

After removing the residual layer in a Reactive Ion Etcher (RIE), titanium and gold are deposited thermally onto the structures which result in the nanopilars and nanolines after lift-off. We used an AFM to measure the topography of the metal structures before proceeding further to the electrodeposition step.

Figure 3.4 and 3.5 show AFM images of gold nanopillars and nanolines fabricated using NIL and lift-off respectively. For the lift-off, the samples were kept in acetone and then the ultrasonic bath for 2 to 3 minutes. The height of the nanopillars and the nanolines was about 23 nm. These gold nanostructures were then used as a seeding layer for electrodeposition of permalloy which is explained in the next section.

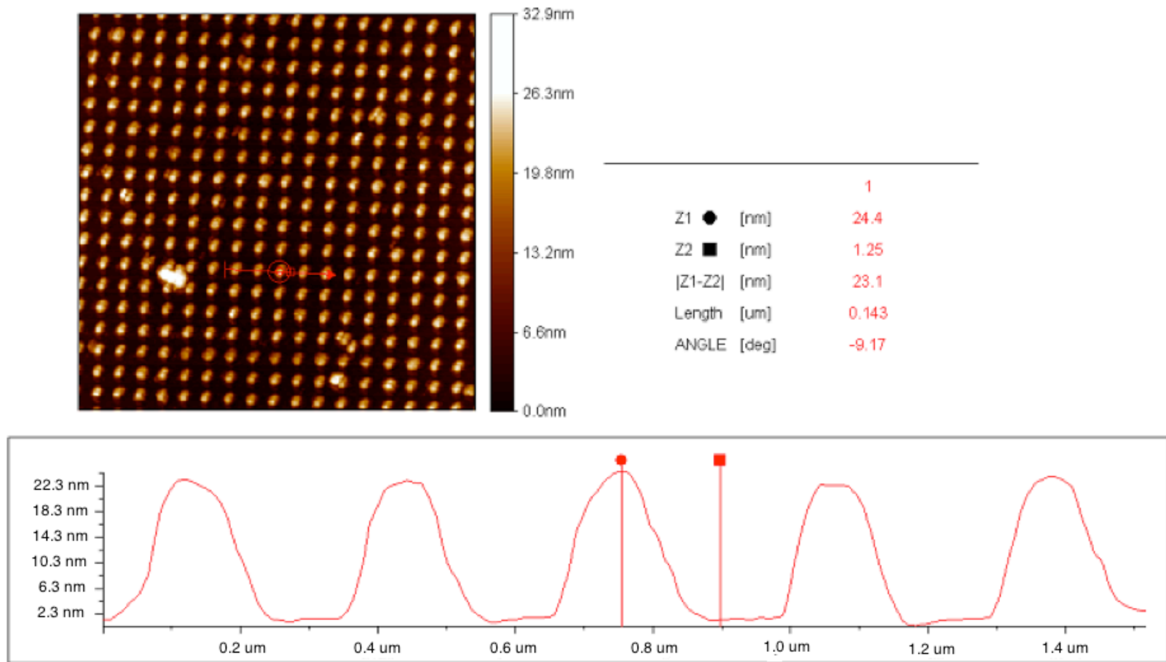

Figure 3.4 AFM image depicting the Au nanopillars after NIL and lift-off.

3.2.2 Electrodeposition

Electrodeposition was the last step in the fabrication process to deposit magnetic material on the metal nano structures obtained after lift-off. Electrodeposition has been used in conjunction with EBL quite a lot in the past but it is an unfeasible process when it comes to large scale manufacturing for the industry [48, 49]. It has been used in the microelectromechanical systems (MEMS) [50, 51] industry as well as for data storage in the hard disk drive industry. Some researchers have also used electrodeposition with EBL to fabricate nanomagnets.

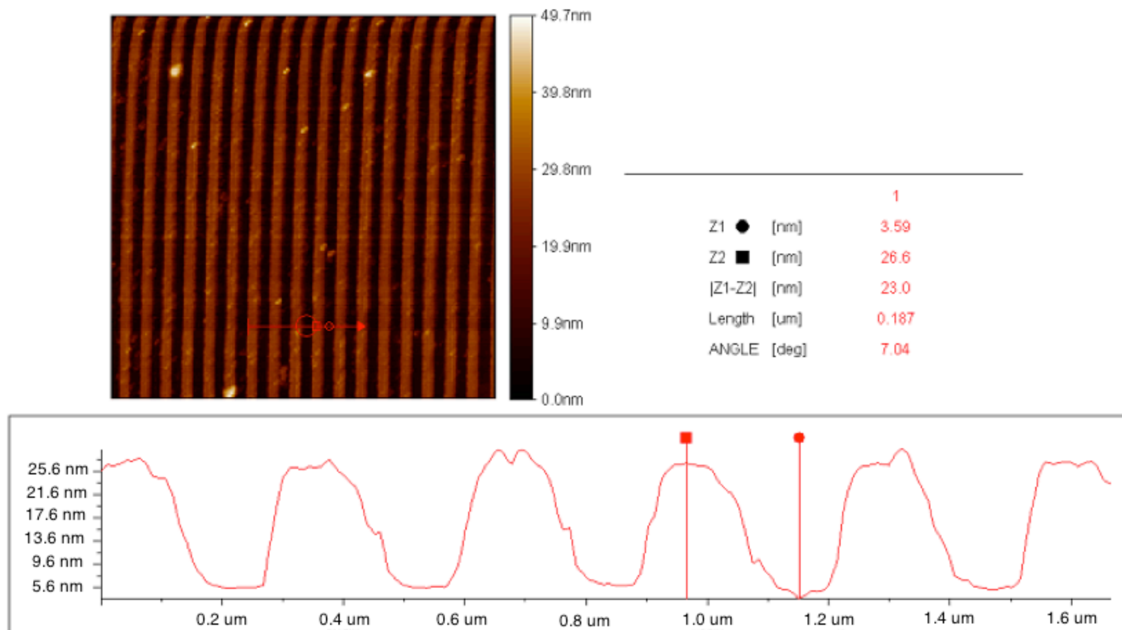

Figure 3.5 AFM image of Au nanolines after NIL and lift-off.

Our process encompasses NIL with electrodeposition for high precision fabrication for many applications which is fast, cheaper as compares to EBL and is suitable commercially. The application in this context is making magnetic nanostructures using Permalloy as the material. Permalloy has already been studied for magnetic properties therefore we will not be going into details of that [52, 53]. Figure 3.6 shows the last 2 steps involved in the electrodeposition step where Permalloy is deposited onto the gold nanostructu
res.

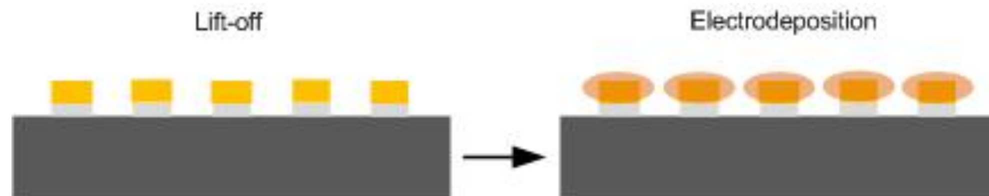

Figure 3.6 Final step of electrodeposition of magnetic material Permalloy onto the gold nanostructures.

A two electrode system is used for electrodeposition. In order to deposit Permalloy, a commercially available electrolyte of Nickel (bought from Conrad) is used and mixed with $FeSO_4$ and saccharine. The solution is stirred for 24 hours to get a proper mix. Experiments showed that adding saccharine to the solution made the deposition of

permalloy more homogenous and more adhesive to the gold structures below acting as seeding layer [54]. Details of electrodepositing permalloy can be found in the literature [55]. Figure 3.7 shows the set up for electrodeposition.

The gold nanostructures act as the cathode whereas a 5 cm x 5 cm platinum wire mesh acts as the anode in the set up. The reason why we use a highly doped p-type substrate is explained as follows. The gold nano structures have an excess of electrons while the p-type silicon substrate has a deficiency of electrons, therefore, the permalloy is only deposited onto the gold nanostructures as we want and not on the entire substrate. Both the anode and cathode are connected to a Keithley 2602 current source which provides 6 mA and it takes about 7 min to electrodeposit.

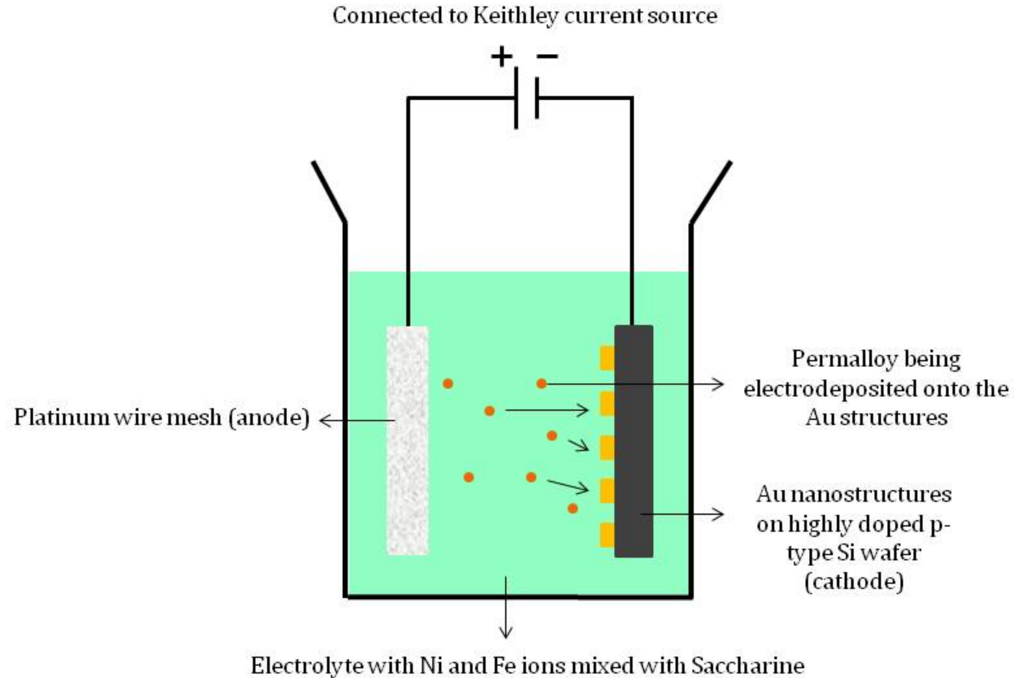

Figure 3.7 Set up for electrodeposition of Permalloy.

After understanding how electrodeposition works, let us now take a look at our results so far. The pillar stamp was used for the imprint and lift-off was done to obtain the metallic gold nanopillars. An AFM measurement was done after lift-off in order to precisely obtain the height of the gold nanopillars which came out to be 23nm as seen in the cross section in figure 3.4 and also to see the topography of the area before doing any electrodeposition on these structures.

Now we move on to the nanolines. The same procedure was applied to fabricate the gold nanolines after lift-off and an AFM measurement was also performed to check the quality of the structures obtained. The height of the structures came out to be 23 nm as shown in figure 3.5 above. There occurred to be slight defects in the samples when they were measured. This is due to some residual resist left over after lift-off. But the majority of the area was uniform.

After checking the quality of the samples, we proceeded to the electrodeposition step which was explained above. Now we will take a look at some SEM and AFM images of the electrodeposited samples with Permalloy. An SEM measurement was done to get a large overview of the structures after electrodeposition and an AFM measurement was also done again to get an estimate on the height of the material electrodeposited. Figure 3.8 depicts and SEM image of the nanopillars after electrodeposition which shows that the nanodots are approximately 200 nm wide. Figure 3.9 depicts an AFM image of the same nanopillars showing a height of about 90 nm. The standard height of the gold and titanium deposited on the nanopillars for lift-off was 20 nm therefore, we can safely say that the remaining height of 70 nm is that of Permalloy electrodeposited onto the nanopillars.

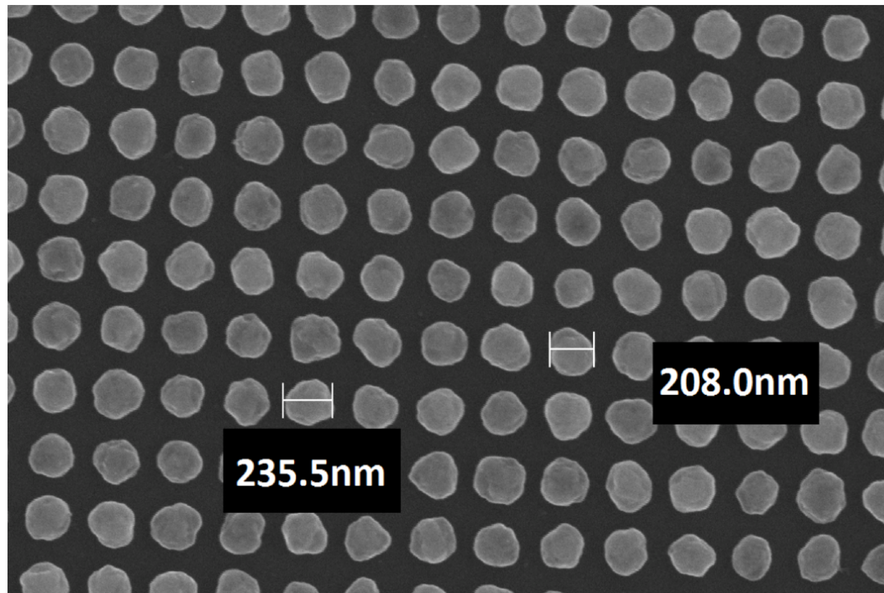

Figure 3.8 SEM image of electrodeposited nanopillars

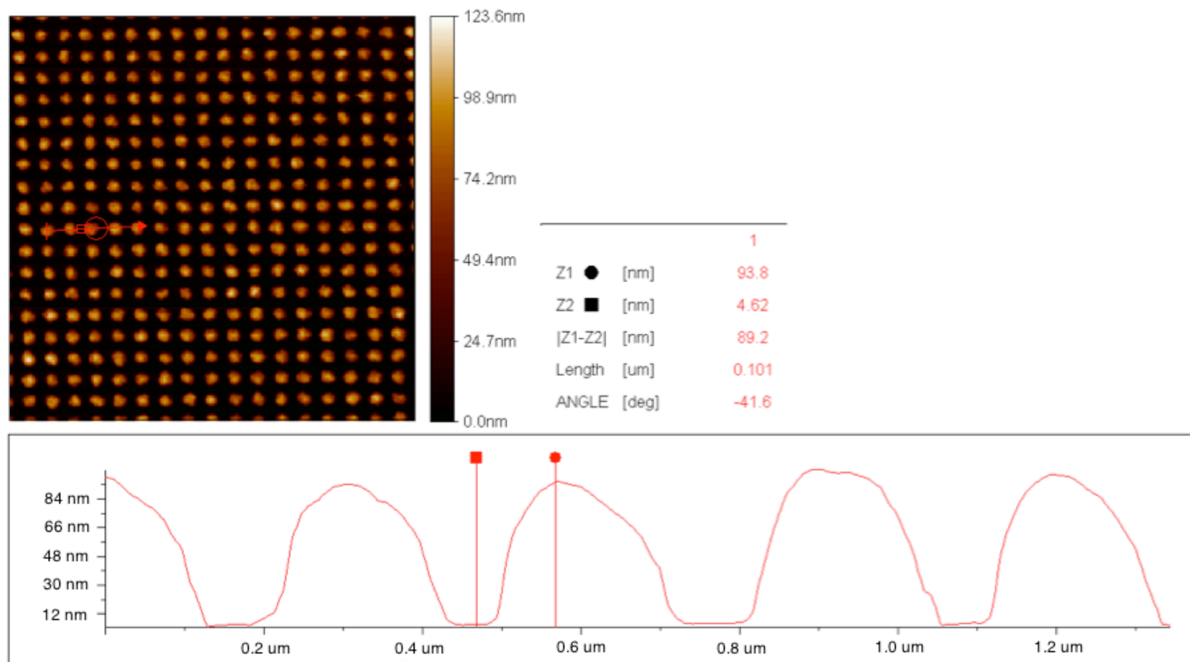

Figure 3.9 AFM image of the electrodeposited nanopillars showing a height of about 90 nm.

Now we take a look at the nanolines. Figure 3.10 shows an SEM image again showing the top view of the electrodeposited nanolines. According to the image, the lines are approximately 140 nm wide. Figure 3.11 shows an AFM image of the same nanolines showing a height of about 45 nm. The original height of the gold nanolines was found to be 23 nm therefore, the remaining height of 22 nm is that of Permalloy on top.

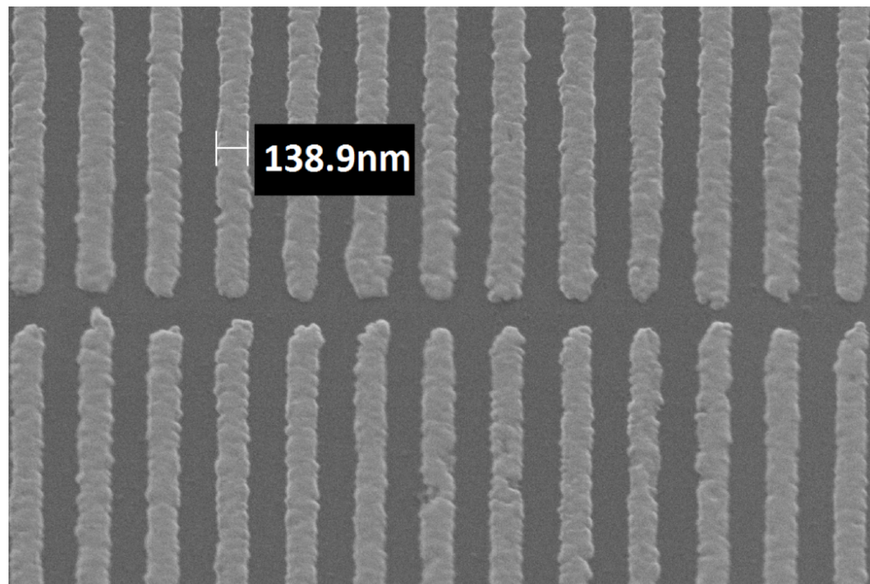

Figure 3.10 SEM image of the top view of electrodeposited nanolines.

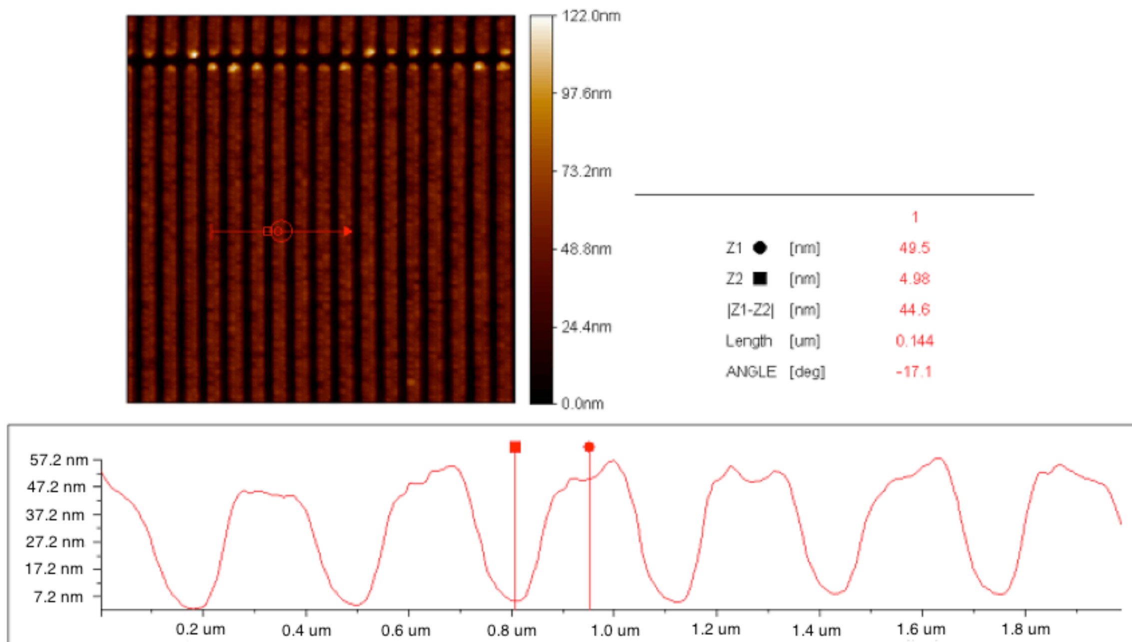

Figure 3.11 AFM image of the electrodeposited nanolines showing a height of about 45 nm.

3.2.3 Nanotransfer and Electrodeposition

We have demonstrated a working procedure for fabricating nanostructures using NIL and electrodeposition. Now we talk briefly about doing electrodeposition on nanostructures which have been fabricated by another process called the nanotransfer printing. We have discussed the fabrication steps involved in nanotransfer printing in detail in the section 2.6. Using this method, nanostructes were fabricated again on a highly doped p-type substrate. We fabricated nanopillars as well as nanolines using nanotransfer printing. Figure 3.12 shows an AFM and SEM image of transferred nanolines.

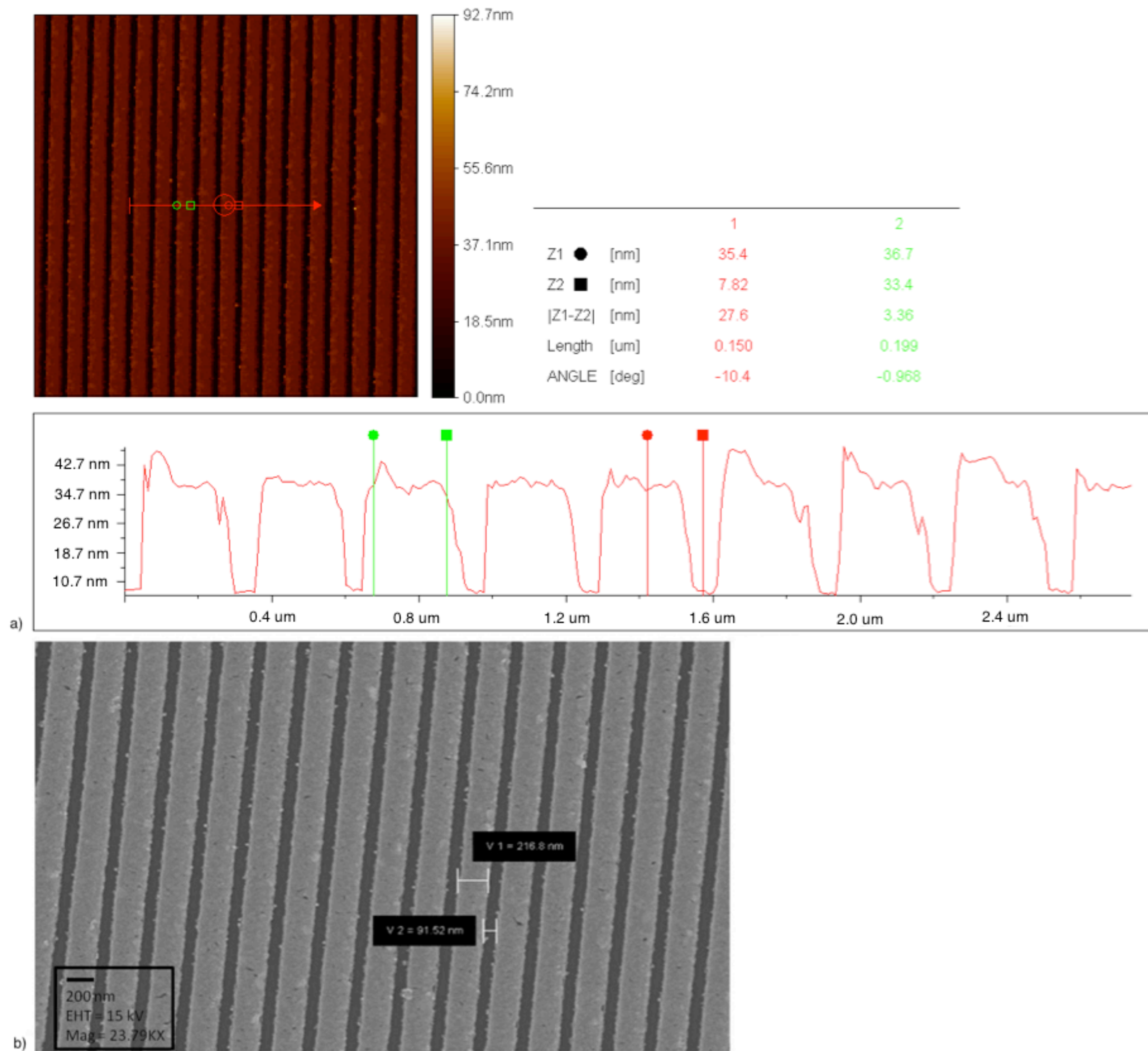

Figure 3.12 a) AFM and b) SEM images of nanotransferred lines.

We observed that the lines although transferred well onto the silicon were very grainy at the edges and not smooth as obtained via lift-off. Due to this, the electrodepositon was not successful over the lines. It was also observed that it was easier to transfer nanolines onto the substrate as compared to nanopillars due to lesser contact of the pillars with the substrate in terms of surface area as compared to lines. Figure 3.13 shows an SEM image of nanopillars electrodeposited with permalloy. It can be seen that the nanopillars are not uniform which can be attributed to lower bonding of the transferred material to the substrate as compared to the material which is evaporated.

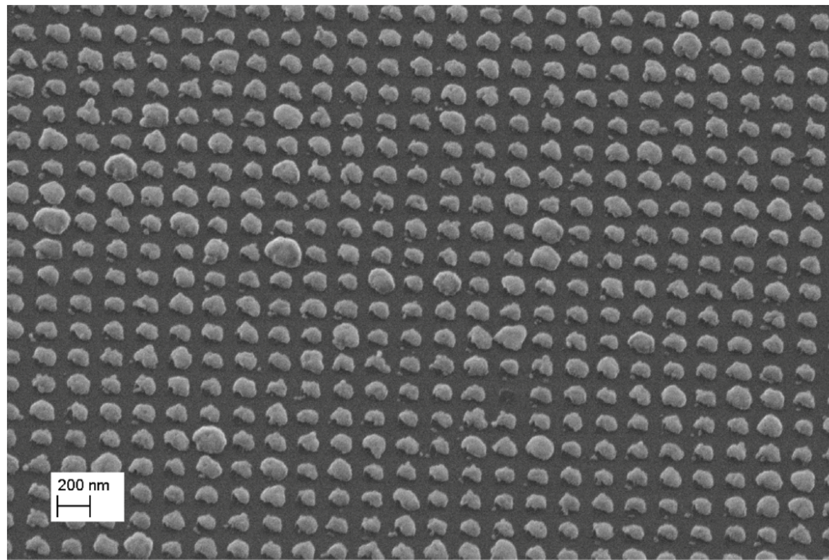

Figure 3.13 SEM image of electrodeposited nanopillars obtained after nanotransfer printing.

Figure 3.14 and 3.15 depict an AFM image of the electrodeposited nanopillars as well as a 3D image respectively where we can see the irregularities in the heights of permalloy deposited. The 3D image gives a more detailed view of the topography of the pillars. Some pillars are 75 nm high whereas some are only 45 nm high. The original height of Ti/Au deposited was around 20 nm. One possible explanation of this is due to the bad bonding of the transferred nanopillars with the silicon substrate, which provides a current path during electrodeposition such that the permalloy is deposited unevenly.

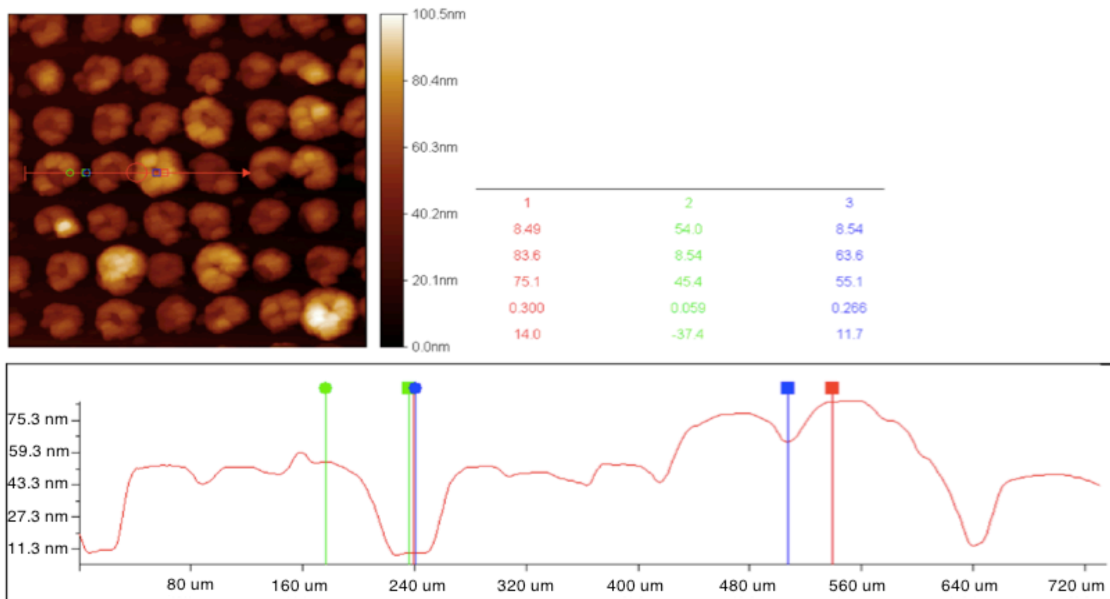

Figure 3.14 AFM image of electrodeposited nanopillars after nTP.

Figure 3.15 3D image of the nanopillars showing detailed topography.

3.3 Results and Discussion

The results henceforth have been taken from the PhD thesis of Muhammad Atyab Imtaar as this project was a collaborative effort. All additional information regarding magnetic behavior can be found in his thesis. Till now we have discussed all the fabrication techniques used to get the desired metal deposition on our nano structures. The material used is as discussed permalloy, thin films of which have in-plane magnetization which are shape dependant. Generally, the magnetization is along the easy axis or longer axis. A Vecco Magnetic Force Microcope (MFM) was used to perform all the magnetic measurements. All the nanopillars and nanolines were subjected to a magnetic field and imaged by the MFM to observe magnetic poles or coupling. Since the magnetization is shape dependant, any object being circular in shape will not show any magnetic poles since both its axes are of the same length. Therefore, the nanopillars did not show any magnetic interaction when measured in the MFM.

The nanolines on the other hand having two different axes did display magnetic poles but were too long in length to be captured in one frame. In order to image them, they had to be cut for which a Focused Ion Beam (FIB) gun was used as discussed below.

3.3.1 Focused Ion Beam Cutting

The nanolines fabricated were too long to be imaged in a single scan field therefore a focused ion beam (FIB) had to be used to cut the nanolines into nano rectangles. A Zeiss NVision Gemini FIB was used for this purpose. The main objective was to cut through the nanolines completely such that no residual metal is left behind which may lead to any interconnects. At the same time, a small width was also necessary between the nano rectangles in order for it to have two ends to be measured in the MFM scan field. Therefore an optimum cut time and width had to be found which could then later be applied to our samples. For experimental purposes, the beam sweep time was varied for 30 s, 60 s, 90 s and 120 s at a current of 10 pA. The length of the cut was 50 µm. The series of four different FIB cut times lead to cut widths of 42 nm, 52nm, 63 nm and 82 nm as shown in figure 3.16.

We observed that there were some interconnects for the 30 s FIB cut but none for the others. Also the cut widths for the higher times were too far apart for proper measurement. The cut at 60 s for 52 nm was the optimum.

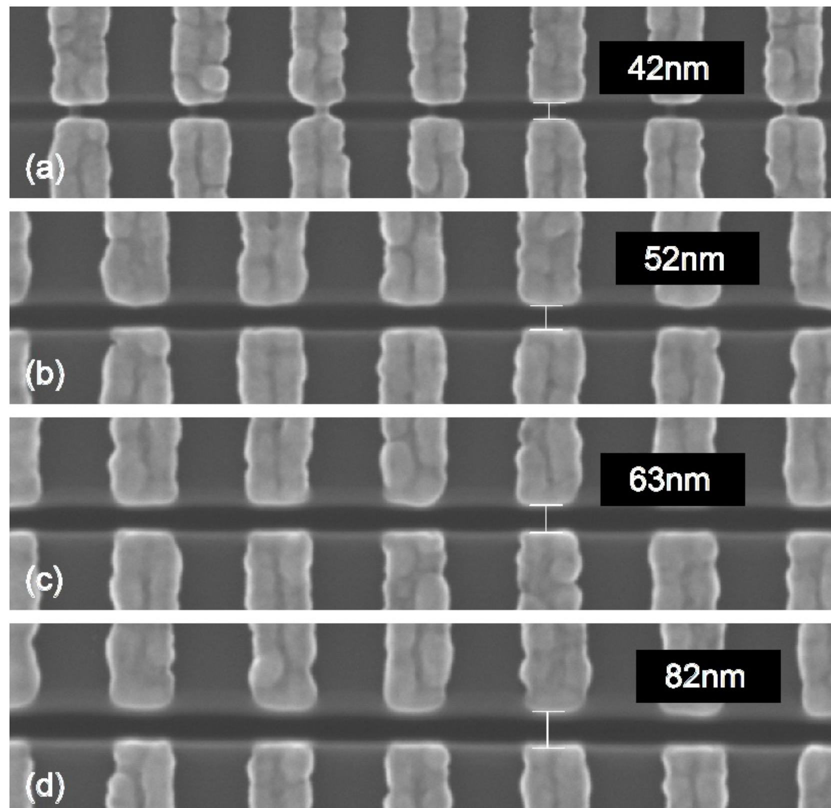

Figure 3.16 SEM image showing the experimental FIB cuts made for a) 30 s b) 60 s c) 90 s and d) 120 s.

These parameters were then used to make four FIB cuts across a length of 50 μm again. The cuts were made perpendicular to the lines in our samples leaving three sets of nano rectangles with different lengths for their longer axes. Figure 3.17 depicts an SEM image of the three sets of nano rectangles with the maximum length being lesser than 340 nm obtained after FIB cutting. These nano rectangles were then placed in a magnetic field oriented along the longer axes of the rectangles.

A magnetic field of 350 mT was applied along the longer axes for a few seconds. It was observed that each of the nano rectangles showed two opposite poles which were detected by the MFM as shown in figure 3.18. We can clearly see that the poles are all aligned in one direction being proof that the electrodeposited material which is permalloy is indeed magnetic in nature.

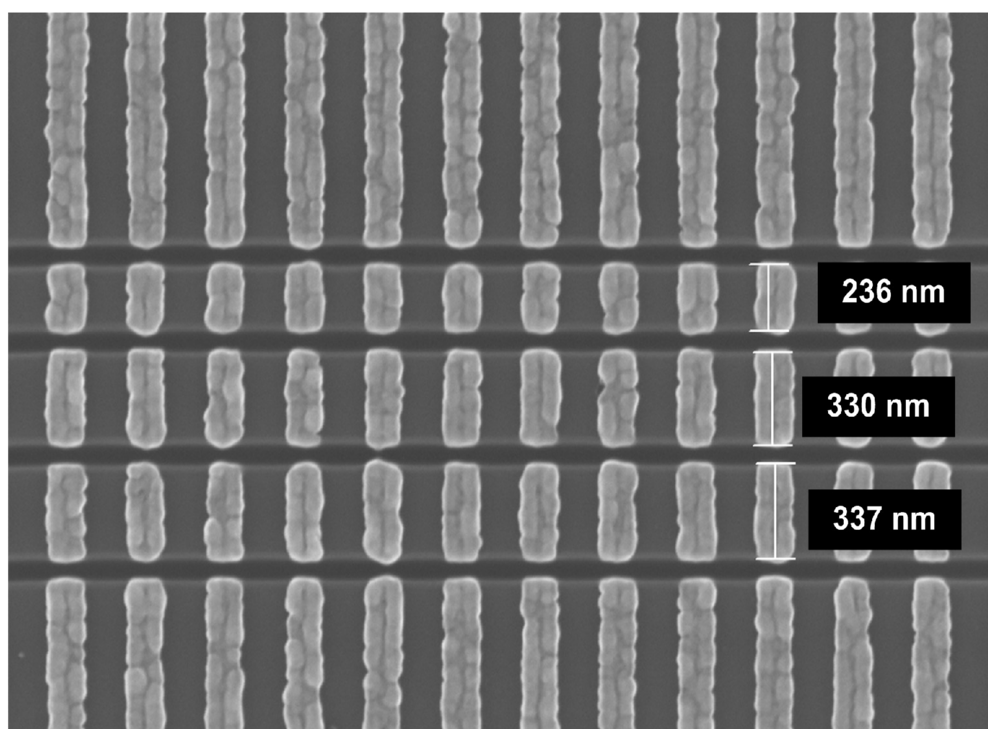

Figure 3.17 SEM image depicting the nano rectangles after FIB cutting. The length of the nano rectangles are 236 nm, 330 nm and 337 nm.

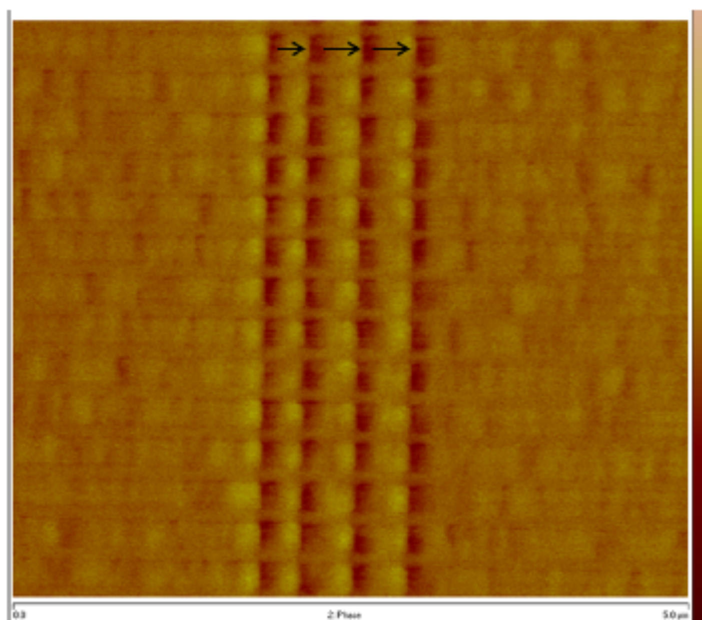

Figure 3.18 MFM image showing the two magnetic poles on the nano rectangles when external magnetic field is applied.

3.4 Summary

We have demonstrated a working process for fabricating magnetic nanostructures using a combination of NIL and electrodeposition. A highly doped p-type silicon wafer was used in order to deposit metal only on the nanostructures and not on the substrate. These nanostrucutres acted as the cathode in the electrodeposition set up. MFM measurements show the magnetic poles of the nanostructures obtained after FIB cutting. Nano magnetic logic can be applied to surface enhanced electrochemistry and this process of fabrication is scalable rendering it very useful for industrial purposes. The nanomagnets fabricated here are less than 340 nm in length. Future work includes going down further in dimension in terms of fabrication while still maintaining the overall structure of a nano magnet with a hard and an easy axis. More work can also be done to optimize the electrodeposition process again in terms of dimensions and homogeneity of the layer deposited.

Chapter 4

NIL for Nanowire Growth

In this chapter we will talk about another application where nanoimprint lithography can be used which is for growing semiconducting nanowires out of an imprinted silicon dioxide substrate. Ternary Indium Galium Arsenide (InGaAs) nanowires (NWs) hold great promise for a variety of device technologies in nanoelectronics, integrated photonics as well as for photodetection and solar cell applications [56]. There are a number of ways of growing nanowires such as chemical beam epitaxy, metal organic chemical vapor deposition (MOCVD), pulsed laser deposition and so on [57]. Research has been done in this area in the past of using NIL to grow carbon nanotubes or nanowires for other applications such as nano electrode or chemical sensors [58]. Here we focus on using Nanoimprint lithography to pattern a silicon dioxide substrate so as to generate holes from which to grow the nanowires in a molecular beam epitaxy (MBE) machine for the purpose of device integration on Si. This project is a collaborative effort with the Walter Schottky Institute of the Technical University of Munich, Germany. Some of the results shown here are part of the PhD thesis of Simon Hertenberger of the Walter Schottky Institute. The work done here is a comparative study of nanowires grown via self assembly using a catalyst and site specifically with a fixed periodicity.

4.1 Introduction

Semiconductor nanowires attract great attention due to their unique geometries and functional properties with heterostructures that provide rich prospects for novel electronic and optoelectronic devices, solar cells, biosensors etc [59]. In particular, InAs are of great interest due to their low band gap energy ($E_g \sim 0.36$ eV), small electron effective mass and high electron mobility (μ = 33,000 cm^2/Vs at 300K). These properties make them predestined for future high speed electronic and near infrared photonic devices [60]. Unfortunately very few studies have been done on this so far arising from the difficult growth of well controlled and uniform Indium Gallium Arsenide (InGaAs) nanowire arrays. Conventional vapor-liquid-solid (VLS) growth with foreign or self-catalysts produced InGaAs nanowires with severe inhomogeneties, evidenced by large composition gradients, undesired tapering, as well as limited group-III element incorporation, independent of the applied growth method [61].

We introduce a novel fabrication technique using NIL which promotes periodical and site selective growth of InGaAs NWs. The composition and uniformity of the position controlled NW arrays is compared with that of the self assembled NWs using high resolution x-ray diffraction (HRXRD), low temperature photoluminescence, energy dispersive x-ray spectroscopy (EDS) and Raman spectroscopy.

4.2 Fabrication of NWs using NIL and MBE

Commercially available 2 inch p-type doped Si wafers (111) were used as substrates with a 20 nm thick thermally grown SiO_2 layer. They were spin coated with a thermal polymer (mr-I 8010 R). A quadratic Si stamp of 8 mm^2 area with periodic pillar structures with a diameter of 60 nm and a pitch of 250 nm was used as a master stamp. The substrate was imprinted with the stamp in an Obducat nanoimprinter. The schematic of NIL has been explained extensively in chapter 2.

The residual layer was removed with O_2 plasma and then the pattern was transferred to the SiO_2 layer with RIE. This left behind an array of holes with an identical diameter and pitch. One final step was performed of dipping this substrate in buffered HF acid to access the underlying Si (111) layer through the holes. This provides further stability against native oxide formation before loading the substrate into the MBE machine for nanowire growth.

The growth was performed in an all-solid-source Gen-II MBE system equipped with several cryopumps to guarantee high purity growth conditions, standard effusion cells for group III elemental sources (In, Ga, Al), and a Vecco valve cracker cell providing uncracked Arsenic (As_4). Several other in-situ analytical capabilities also included an optical pyrometer for measuring growth temperature (T).

All material fluxes [ϕ(In), ϕ(Ga) and ϕ(As)] used for growth are given in equivalent two-dimensional (2D) growth rate units (Å/s). $In_{1-x}Ga_xAs$ NW growth was performed under As-rich conditions with ϕ(As) = 20.3 Å/s and a fixed total group-III flux ϕ(Ga) + ϕ(In) = 0.36Å/s [As/(Ga+In) ratio = 56.5]. To achieve composition tuning of the $In_{1-x}Ga_xAs$ NWs with variable Ga content x(Ga), the ($\phi^{Ga}/\phi^{In}+\phi^{Ga}$) ratio was adjusted while keeping the total group III flux fixed. Growth temperature and time were also fixed at T=550°C and t=1h, unless otherwise specified. Figure 4.1 depicts a basic schematic of NW growth from NIL.

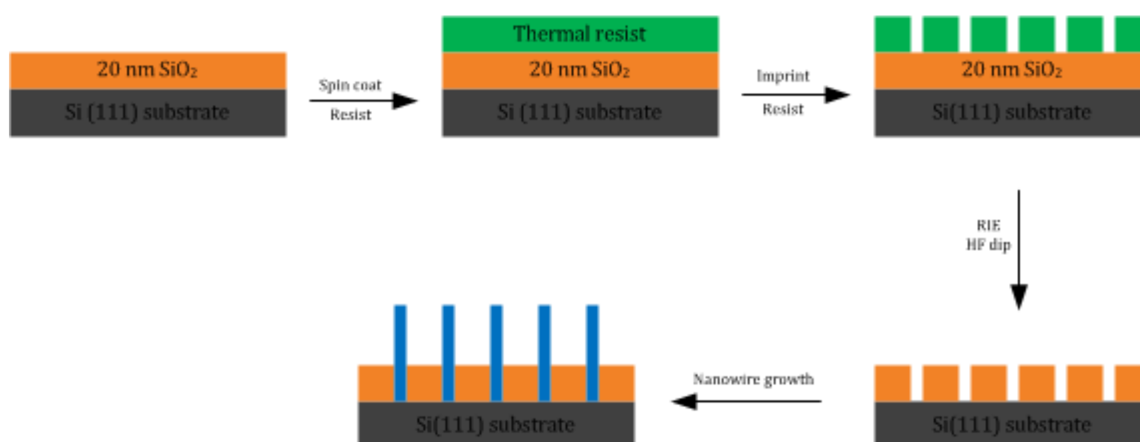

Figure 4.1 Schematic showing nanowire growth after NIL.

A variation of the hole pitches was also used during nanoimprinting to give us a better idea of the growth time vs. pitch. The different pitches used were 250 nm, 500 nm, 1000 nm, 2000 nm and 10,000 nm. Figure 4.2 gives some examples of the pitch variation after NIL and before growth. Following are 3 3D images depicting the pitches 250 nm, 500 nm and 2000 nm.

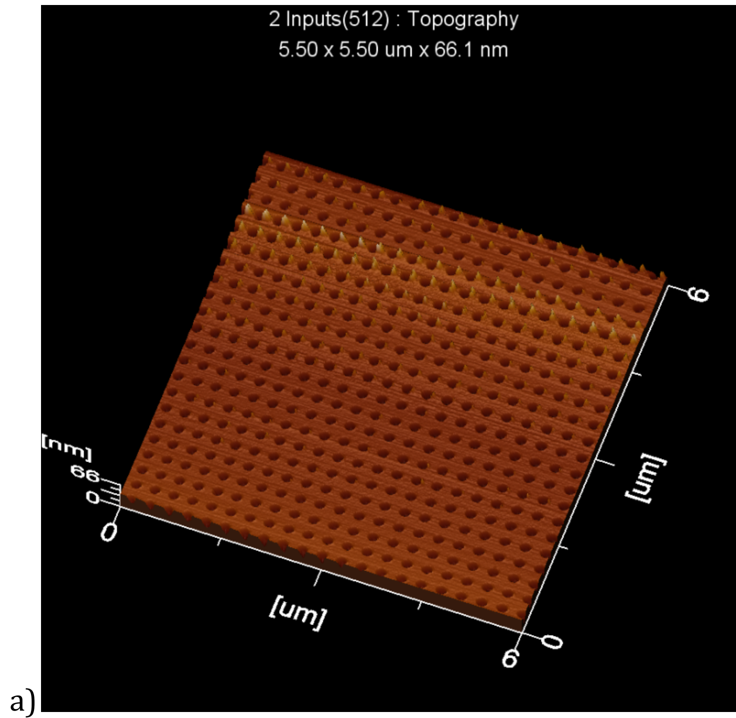

a)

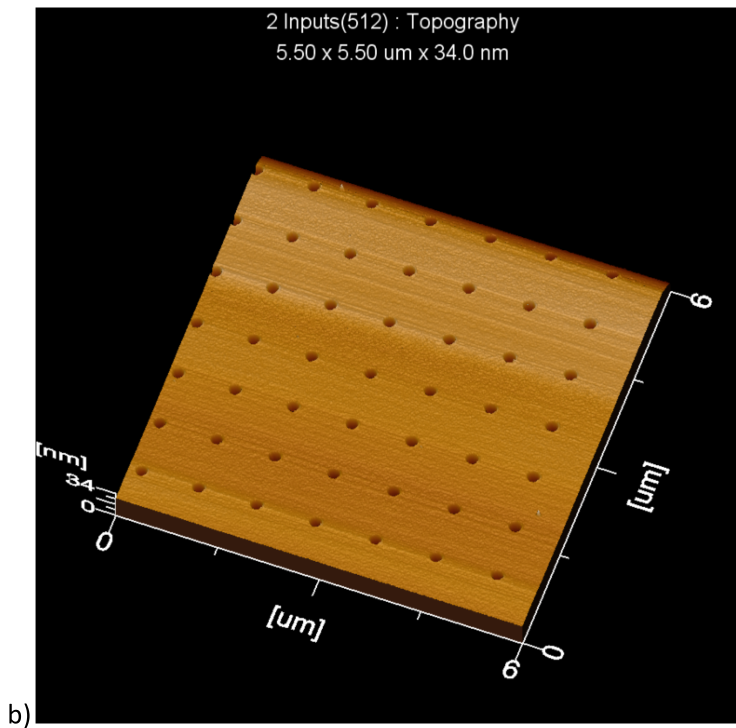

b)

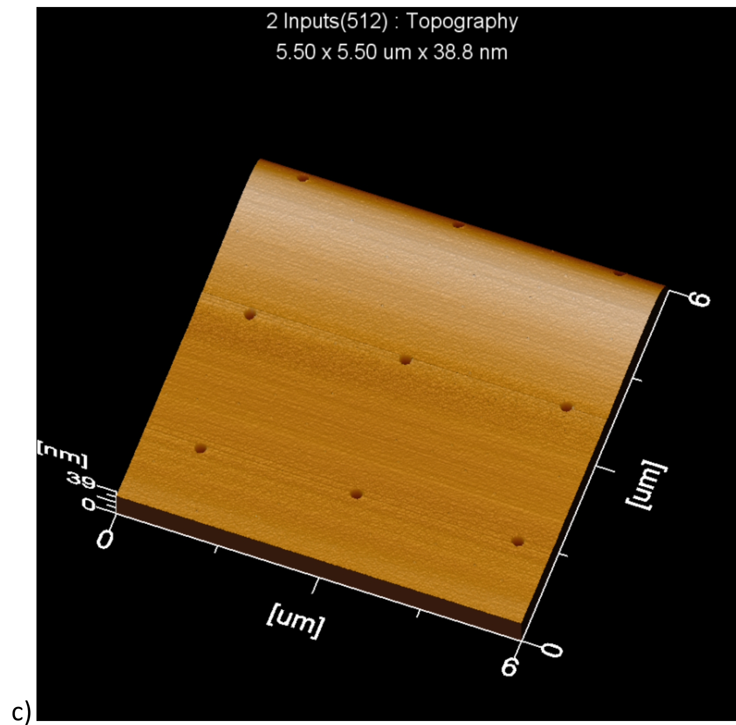

c)

Figure 4.2 3 D images showing the imprinted holes in varying pitches of a) 250 nm, b) 500 nm and c) 2000 nm.

Figure 4.3 depicts SEM images of site selectively grown InGaAs nanowires growing out of imprinted SiO_2/Si (111) substrates for various $(\phi^{Ga}/\phi^{In}+\phi^{Ga})$ ratios. The pitch in this case is 250 nm. The upper panel in fig 4.3 a) depicts a photograph of the edge of the imprinted area of NWs and the surrounding SiO_2 substrate showing the InGaAs growth selectivity and the sharp contrast in the patterned and unpatterned area. The lower panel shows a magnified top view SEM image of the grown NWs with a $(\phi^{Ga}/\phi^{In}+\phi^{Ga})$ ratio of 0.1. A tilted view of the NWs is also shown in the images b) – d) for different $(\phi^{Ga}/\phi^{In}+\phi^{Ga})$ ratios of b) 0.1, c) 0.3 and d) 0.5. Growths with higher $(\phi^{Ga}/\phi^{In}+\phi^{Ga})$ ratios was also attempted (higher than 0.5) and resulted in formation of NWs but with lower volume due to parasitic growth under the given growth conditions. This can be avoided by adjusting the growth temperature T and [As/(Ga+In)] ratio.

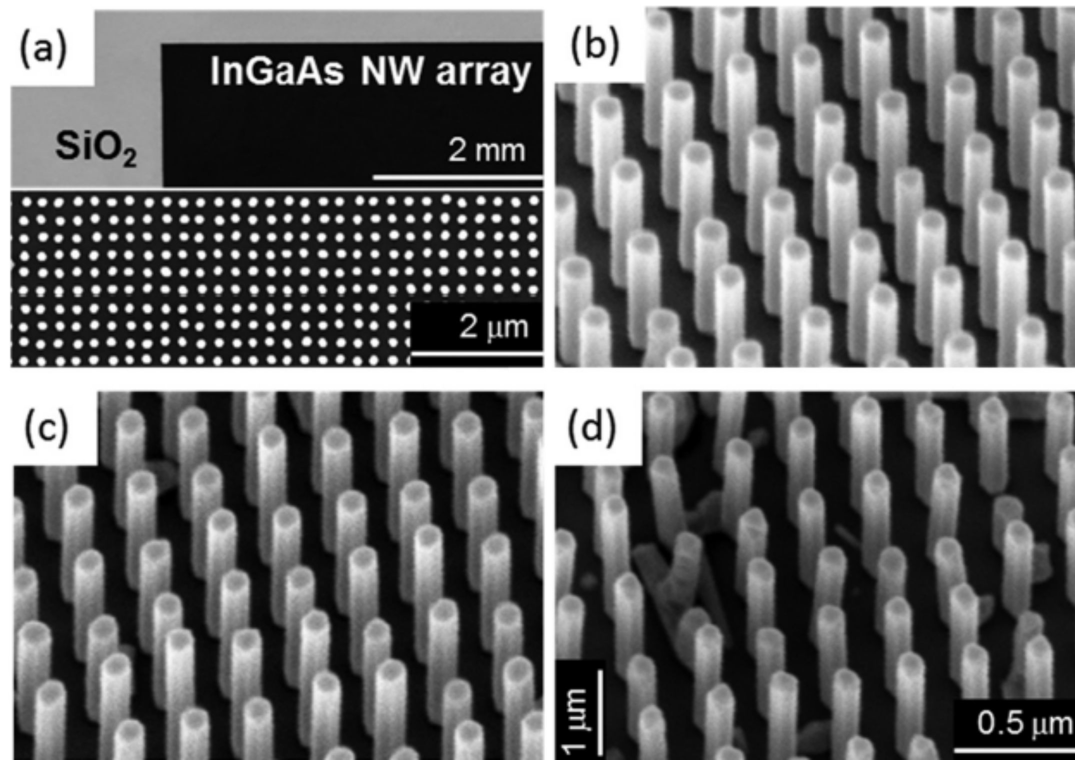

Figure 4.3 SEM images of InGaAs nanowires grown on nanoimprinted SiO_2 substrates where a) shows the top view and photograph of the NW array and b) – d) NW arrays grown with different concentrations of Ga.

One of the main difficulties faced during imprinting was the lateral shifting of the stamp over the substrate while the imprint was going on. This resulted in elongated hole patterns through which nanowire could not be grown. The diameter of the imprinted holes increased considerably from 60 nm to more than 150 nm. Figure 4.4 depicts some examples of such lateral shifts observed after the imprint process.

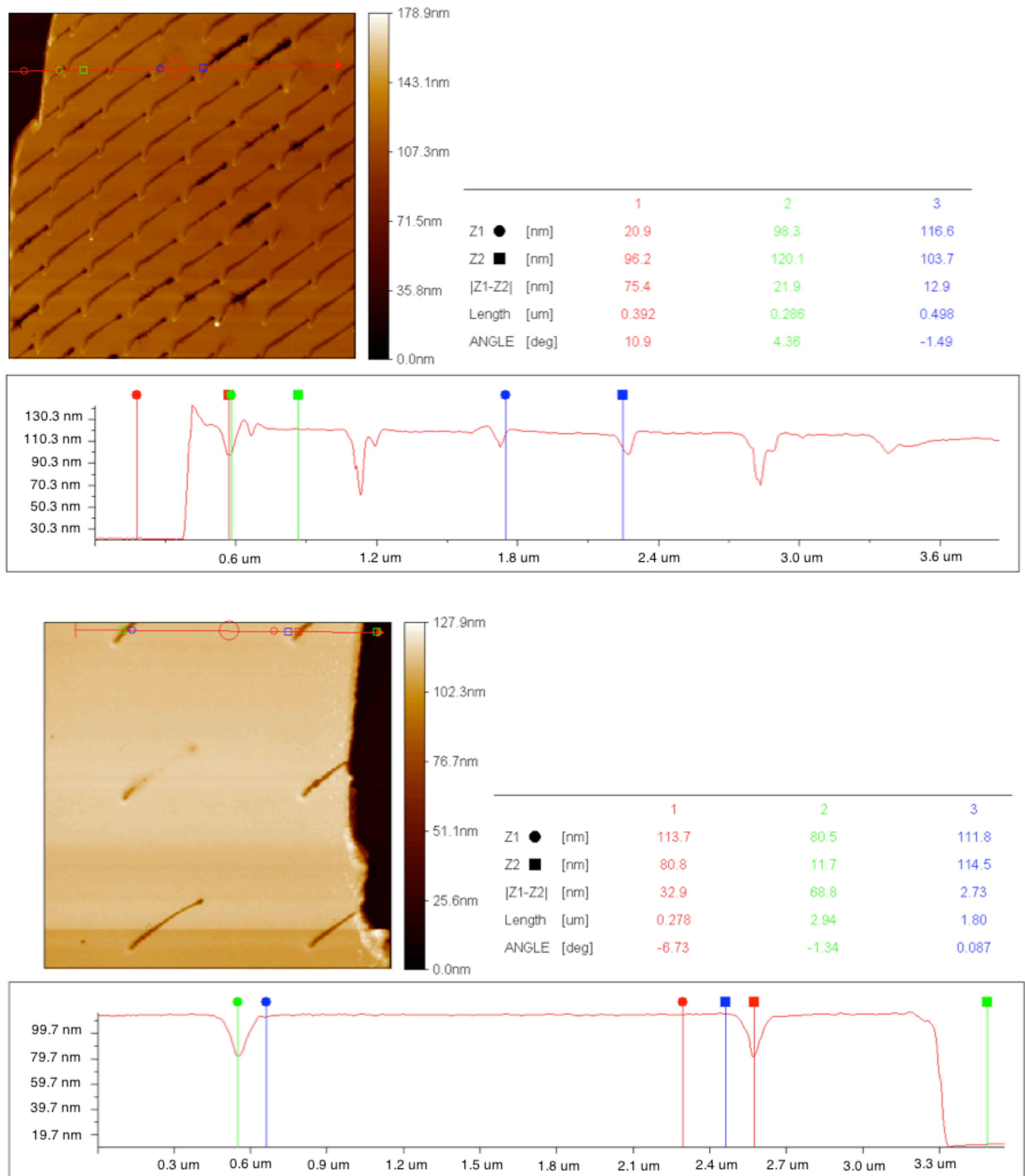

Figure 4.4 AFM images showing lateral shift during imprint of pitch 500 nm (above) and 2000 nm (below).

The reason for this shift was that when the polymer is above its T_g, it starts flowing around the structures and the nanometer scale structures are far too small to grab the stamp and substrate together in one position. Therefore, with the movement of the polymer, the stamp also slides around over the substrate causing shifted imprints. This

can be avoided by fabricating alignment markers around the main structures on the stamp. Alignment markers are micrometer structures which help in holding together the stamp and substrate in place such that the stamp does not move during any imprint process. Figure 4.5 shows a simple schematic of such alignment markers.

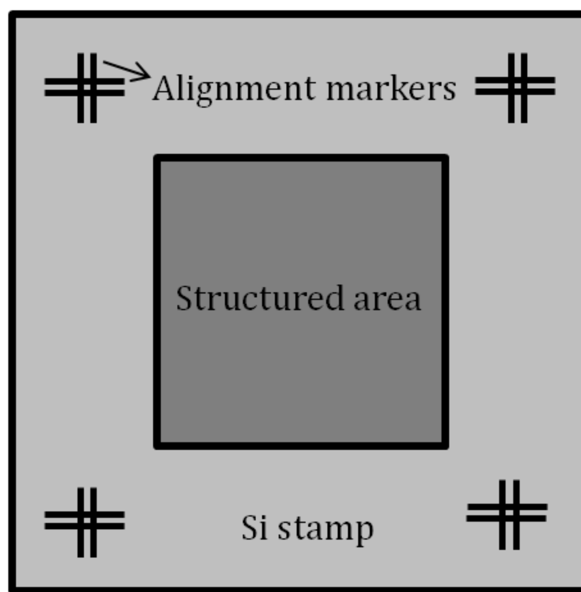

Figure 4.5 Simple schematic showing alignment markers around the structured area of a stamp to avoid lateral displacement during an imprint process.

4.3 Results and Discussion

As we have already seen above, post growth characterization was performed using a field emission scanning electron microscopy (FE-SEM). HRXRD (Phillips X'Pert Pro MRD diffractometer), and low temperature photoluminescence at 20K (Biorad FTS-40 Fourier transform infrared spectrometer in closed-cycle helium cryostat) employing a 1.55 μm cw diode laser excitation source and liquid nitrogen to cooled InSb photodetector were also performed. Raman spectroscopy was conducted in a μ- Raman setup in backscattering geometry, utilizing excitation energy at 2.41 eV and a laser spot size of ~ 2 μm (NA = 0.4).

4.3.1 HRXRD Measurements

To derive the actual composition of the $In_{1-x}Ga_xAs$ NW arrays grown under the different ($\phi^{Ga}/\phi^{In}+\phi^{Ga}$) ratios, 2θ-ω HRXRD scans were recorded and the Ga content x(Ga)determined by Vegard's law under the assumption that the NW s are completely relaxed.

Here, the as-measured peak reflections of InAs (2θ = 25.33) and GaAs (2θ =27.30) were taken as the binary boundary conditions from which the alloy composition was linearly interpolated for the different $In_{1-x}Ga_xAs$ NW samples via shifts in 2θ peak position (and respective lattice constant).

Fig. 4.6 a) shows the 2θ-ω HRXRD scans of all $In_{1-x}Ga_xAs$ NW arrays normalzed with respect to the peak intensity of binary InAs NWs. This yields x(Ga) of 0.07, 0.19, and 0.36 for supplied ($\phi^{Ga}/\phi^{In}+\phi^{Ga}$) ratios of 0.1, 0.3 and 0.5 respectively. Note that besides the Si (111) substrate peak at 2θ = 28.44° and the composition-dependent $In_{1-x}Ga_xAs$ NW 2θ - peaks, no other reflections were observed over a large 2θ range of 0° – 60°. This confirms the direct epitaxial relationship between all $In_{1-x}Ga_xAs$ NW arrays and Si [62].

The HRXRD full-width-at-half-maximum (FWHM) values of the $In_{1-x}Ga_xAs$ NW 2θ peak width were measured to evaluate whether significant composition inhomogeneities and phase separation are present across this array. For this analysis, all $In_{1-x}Ga_xAs$ peaks with x(Ga) ≤ 0.19 were best fitted by a single Voigt function, while the $In_{1-x}Ga_xAs$ peak with x(Ga) = 0.36—which exhibits some asymmetry—was best fitted by two Voigt functions (with peak maxima at 2θ = 26.037° and 26.065°, indicated in grey). We note that the low intensity peak which fits the asymmetric shoulder at 2θ = 26.065° is related to the zinc blend (111) reflection and stems from parasitic clusters formed in between the NWs for this growth. On the other hand, the major peak at 2θ = 26.037° is associated with the NW-based wurtzite (002) reflection, similar to the single (002) peak reflection observed for all other cluster-free $In_{1-x}Ga_xAs$ NW arrays grown with lower x(Ga). Most interestingly, comparison of all the fitted NW-related peak widths gives very similar FWHM values between 0.031° and 0.039°. This indicates rather low degree of compositional inhomogeneity for the site-selectively grown $In_{1-x}Ga_xAs$ NW arrays.

Significantly broader FWHM values were determined under identical measurement conditions for $In_{1-x}Ga_xAs$ NW arrays grown in a self-assembled manner on non-lithographic SiO_2/Si (111) templates. Fig. 4.6 b) provides a direct comparison between the 2θ-(InGaAs)-FWHM values of a site- selectively grown $In_{1-x}Ga_xAs$ NW array [x(Ga) = 0.07] and a self-assembled $In_{1-x}Ga_xAs$ NW array [x(Ga) = 0.08], which were grown under similar conditions. While the FWHM value for the site-selectively grown NW array was as small as 0.031°, the respective value for the self-assembled NW array was more than a factor of 2 larger (FWHM = 0.084°). As can be seen from the left in-set image in fig 4.6 b), the self-assembled NWs are spatially and randomly distributed. Not only larger compositional inhomogeneities but also much larger dispersion in NW length and diameter are observed.

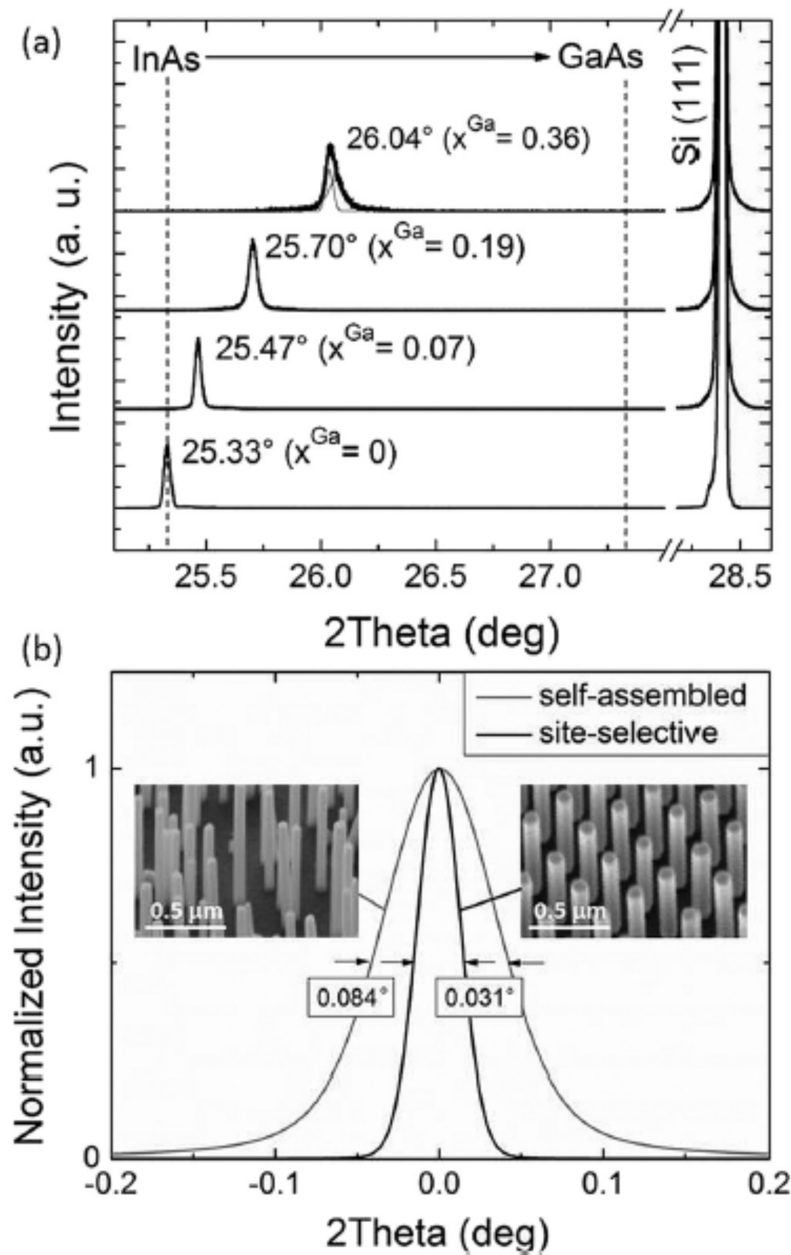

Figure 4.6 a) HRXRD 2θ-ω scans of site-selective $In_{1-x}Ga_xAs$ NW arrays on NIL-SiO_2/Si (111) grown under the different ($\phi^{Ga}/\phi^{In}+\phi^{Ga}$) ratios. Dashed lines indicate the 2θ peak positions of binary InAs and GaAs (as measured), facilitating linear interpolation of the actual Ga content x(Ga) from the respective 2θ peak positions (i.e., lattice constants) of the $In_{1-x}Ga_xAs$ NW arrays via Vegard's law. The uppermost scan [x(Ga) = 0.36] shows two fitted curves at 2θ = 26.037° and 26.065° corresponding to wurtzite-based NW and zincblende-based cluster signatures, respectively. b) Normalized intensity of the 2θ-InGaAs peak position comparing similarly grown site-selective and self-assembled NWs. Insets illustrate SEM images of the two types of NWs.

4.3.2 Raman Spectroscopy

To confirm the larger disorder and dispersion in the self- assembled NWs with respect to the site-selective NWs, μ-Raman spectroscopy was performed on NW ensembles dispersed onto a Si substrate. Since the NWs lay randomly oriented on the substrate, the measurements represent the average of two orthogonal polarization configurations with no polarization selection for the scattered light. Representative Raman spectra are presented in Fig. 4.7 as obtained from measurements on self-assembled and site-selective $In_{1-x}Ga_xAs$ NW ensembles grown under completely identical conditions [x(Ga) = 0.19]. As can clearly be seen from Fig. 4.7, the LO modes broaden and are higher in relative intensity (increased LO/TO ratio) for the self-assembled NWs. For a more quantitative analysis, Lorentzian peak fitting of the LO and TO phonon modes was conducted (fitted curves indicated as solid lines) and the individual fits of the important disorder-sensitive InAs-like and GaAs-like LO modes are shown as dashed lines (displayed by offsets). The fits for the LO modes directly evidence increased relative LO/TO intensity and increased LO-FWHM for both the InAs-like and GaAs-like LO modes in the case of self-assembled growth. Interestingly, the described differences were absent when comparing binary self-assembled and site-selective NWs, i.e., pure InAs NWs [x(Ga) = 0]. This supports our conclusion that the disorder - mediated effects are mainly caused by composition inhomogeneities across arrays of self-assembled $In_{1-x}Ga_xAs$ NWs [62].

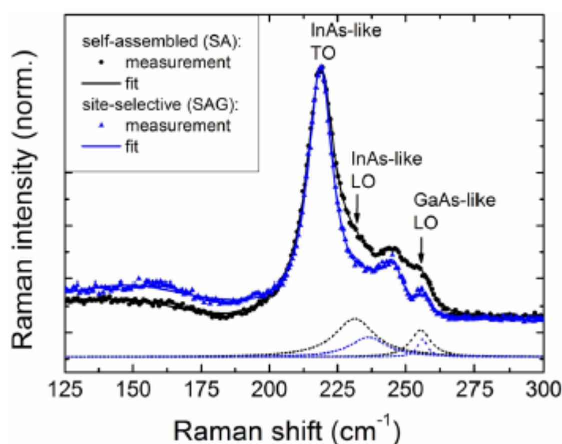

Figure 4.7 Raman spectra of site-selectively grown and self- assembled $In_{1-x}Ga_xAs$ NWs with identical x(Ga) = 0.19, measured under identical conditions. Spectra are normalized to the InAs-like TO phonon peak and a multiple-Lorentzian fitting was conducted (solid lines). Fits of the disorder-sensitive LO modes (InAs- and GaAs-like) are shown as dashed lines (offset for visibility). Note the obvious increase in LO/TO ratio and LO-FWHM for both the InAs- and GaAs-like LO modes in the case of self-assembled NWs.

4.3.3 Photoluminescence

To further substantiate the higher uniformity for the site-selectively grown $In_{1-x}Ga_xAs$ NW arrays, additional low-temperature PL spectroscopy (at 20 K) was performed on these types of NWs. Interestingly, due to the excellent periodicity of the vertically aligned NW arrays, no PL emission was observed by excitation under normal incidence to the sample surface. This unique behavior can be traced to the formation of two-dimensional photonic bands, where emission is preferentially into guided photonic bands in the plane and not perpendicular to the sample surface, such that the emitted light cannot effectively reach the detector. Hence for appropriate probing of the PL emission, the free-standing $In_{1-x}Ga_xAs$ NW arrays were mechanically transferred onto a Si substrate (nearly 1:1 transfer ratio) facilitating laser excitation perpendicular to the NW axis. The characteristic PL spectra of all $In_{1-x}Ga_xAs$ NW samples normalized to the intensity of the binary InAs NW reference sample [x(Ga) = 0] are presented in Fig. 4.8. The PL spectra show the expected trend of increasing PL peak emission energy with x(Ga) [x(Ga) given in HRXRD measured quantities]. Most strikingly, the PL linewidths (FWHM) are found as narrow as 29–33 meV and independent of Ga content x(Ga). This striking observation, together with the independence in PL linewidth for variable x(Ga), underlines the overall uniform composition for the investigated $In_{1-x}Ga_xAs$ NW arrays [62].

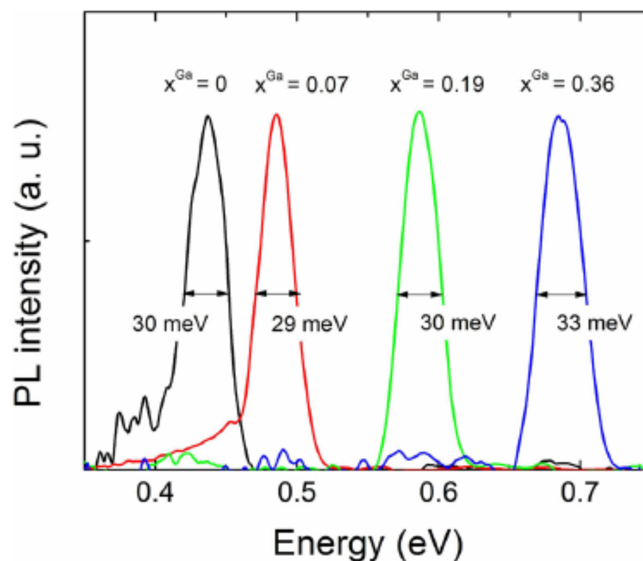

Figure 4.8 Low-temperature (20 K) PL spectra of composition-tuned site-selective NW arrays on NIL-SiO2/Si (111). Measurements were performed at NW ensembles (dispersed onto a Si substrate) with the NW axis lying perpendicular to the laser excitation. Note that the PL linewidths are independent of x(Ga).

4.4 Summary

In this chapter we have focused on one more application of Nanoimprint Lithography and shown the fabrication of InGaAs NW arrays using NIL which results in periodic NWs grown out of a Si/SiO_2 (111) substrate. Comparisons between site-selective and self-assembled grown NWs have shown clear results. These results provide evidence that homogeneous growth of periodic InGaAs NW arrays is mandatory to achieve the most uniform composition control with minimal phase separation. This is necessary to minimize inter-wire dependant adatom collection and incorporation dispersion which is mandatory for future large-scale device integration.

Chapter 5

NIL for Plasmonics

This chapter deals with yet another application of the lithographic technique that we have been talking about in the last 4 chapters. NIL presents great opportunities in various fields of engineering and research among which we have already discussed the magnetic and electronic applications. In this section we will talk about how NIL can be implemented to fabricate optical components such as waveguide gratings, sub-wavelength grating structures etc. The performance of electronic circuits is becoming rather limited these days when it comes to the transmission of digital signal from one point to another. Photonics was a solution to this problem by means of implementing purely optical communication systems based on optical fibers. Unfortunately, these micrometer scale bulky components could not be integrated onto electronic circuits which are measured in nanoscale these days. Therefore, surface plasmon based circuits which merge electronics and photonics at the nanoscale may offer a solution to this size compatibility issue [63]. A lot of research has been done in the past on plasmonic devices used for various applications as detectors [64], emitters [65], photovoltaic devices [66, 67, 68] and other optoelectronic applications [69, 70, 71]. In this chapter we will talk about patterning the different layers of the device in question (in this case, an OPD) and checking the change in its optical properties. We focus on patterning the bottom most layer of the device stack in this chapter which is the metallic gratings on our substrate.

5.1 Introduction

As we know, optical interconnects such as fiber optic cables can carry data much faster than electronic interconnects. But the optical cables are also much larger than the electronic counterparts therefore; it is a matter of concern to combine the two technologies on the same circuit. As mentioned above, a proposal to solve this problem was to have a circuit with nanoscale features which could carry optical signals as well as electronic currents. Surface plasmons came into popularity as they are electromagnetic waves that propagate along the surface of a conductor. The interaction of light with matter has led to a new branch of photonics called plasmonics [63]. Such plasmonic chips are also called 'light on a wire' due to their ability to combine both electronic and optical components perfectly on a circuit. Surface plasmons have the capacity to confine light to very small dimensions. They are light waves that occur at a metal/dielectric interface where a group of electrons is collectively moving back and forth [72]. These waves are trapped near the surface as they interact with the plasma of electrons near the surface of the metal. The resonant interaction between electron charged oscillations near the surface of the metal and electromagnetic field of light creates the surface plasmons and results in unique properties. Surface plasmons are bound to the metallic surface with exponentially decaying fields in both neighboring media. This decay length is determined by the skin depth which can be as small as 10 nm, two orders of magnitude smaller than the wavelength of light in air. This feature of surface plasmons provides the possibility of localization and the guiding of light in subwavelength metallic structures and it can be used to create miniaturized optoelectronic circuits with subwavelength components [73].

Various geometries can be used to guide the plasmonic signals in a dielectric [74]. Thin metal films of finite width embedded in a dielectric can be used as plasmonic waveguides. To achieve subwavelength localization, the length of the wire can be reduced and subsequently guide the light under these nanowires using the surface plasmons generated. In nanowires, the confinement of electrons in two dimensions leads to well defined dipole surface plasmon resonances.

The goal here is to achieve grating structures on our substrate by using NIL. A lot of research has been done previously to obtain waveguides and gratings using NIL as the fabrication tool [75, 76, 77]. Other fabrication techniques have also been used to generate plasmonic interference patterns or grating structures [78, 79].

We will focus on using nanolines as our structures to generate surface plasmons in air as the dielectric. The metal used in our experiments is gold as the comparison later on of our gratings is done with a plain gold film. In the next section of this chapter we will describe the device structure or stack of an organic photo detector (OPD) used for our experiments.

5.2 Device Stack

The device used in these experiments is a standard OPD, the layers of which are represented schematically in figure 5.1. Since it is for an optical application, the bottom layer is kept as glass or Indium Tin Oxide (ITO). Then there is a conducting layer comprised of poly (3, 4-ethylenedioxythiophene) poly (styrenesulfonate) (PEDOT:PSS). The active layer consists of a blend of regioregular poly (3-hexylthiophene-2, 5-diyl) (P3HT) and (6, 6) - phenyl C61 butyric acid methyl ester (PCBM). We will discuss about PEDOT:PSS in detail in the next chapter. Lastly, a metal layer of usually Aluminum is evaporated on top to seal off the remaining bottom layers.

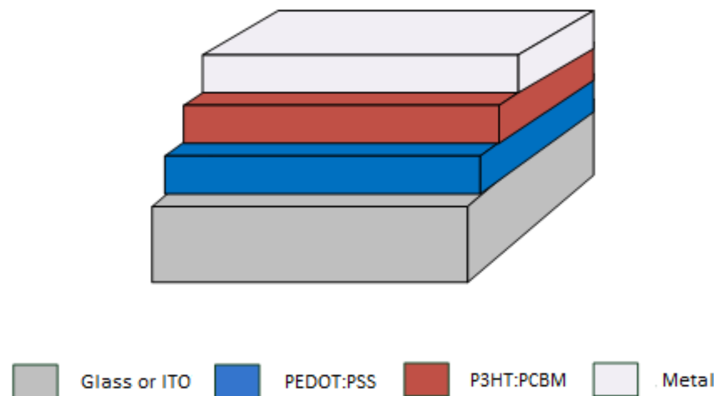

Figure 5.1 Schematic of the different layers of an OPD.

5.3 Fabrication

Having discussed the layer stack of the device, it is now time to talk about the fabrication details and techniques used to achieve the grating structures desired. In this section we will talk only about the first layer that is glass or ITO. The idea was to fabricate metal gratings on the glass/ITO and NIL as well as nTP was utilized for

achieving this. Figure 5.2 gives an idea of what the gratings would look like in the device stack.

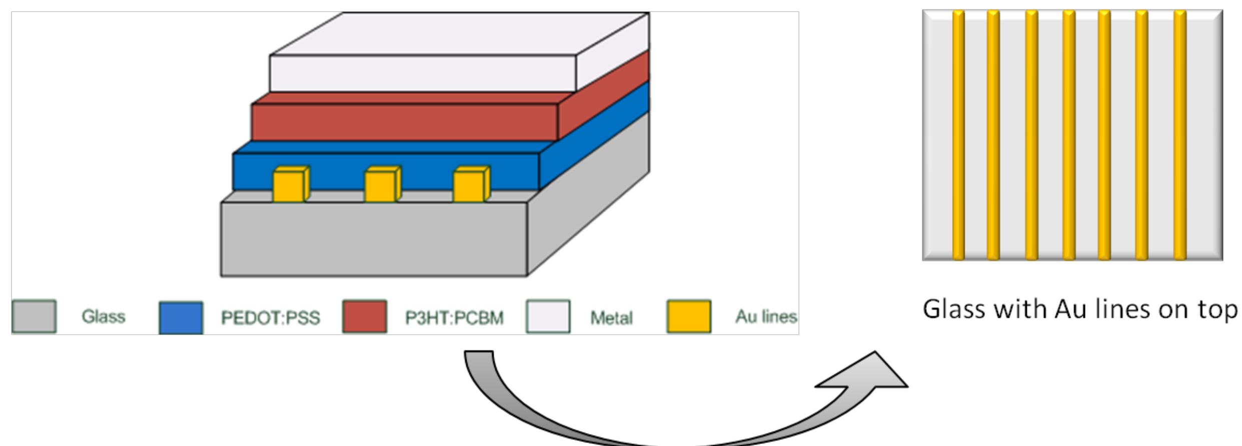

Figure 5.2 Representation of the metal gratings on the glass/ITO.

An ITO substrate was first cleaned in Acetone and Isopronanol in an ultrasonic bath for 10 minutes each. It was then spin coated with a thermal imprint polymer (mrI 8010R, Microresist, Germany) at 3000 rpm for 30 seconds and heated on a hotplate for 1 minute at 100°C to remove the excess solvents. A silicon stamp consisting of nanolines of 60 nm width with a pitch of 250 nm was used for imprinting over the ITO substrate using our standard 2” imprinter (Obducat, Sweden), the working principle of which was described in section 2.2. The residual layer was removed with oxygen plasma in a RIE. In order to get metallic gratings, a layer of Titanium (4 nm) and Gold (20 nm) was evaporated over the structured ITO. Titanium was used as an adhesive layer between the gold and the ITO. A quick dip in Acetone resulted in a very good lift-off and left behind gold gratings on the ITO which was desired. Figure 5.3 depicts an AFM image of the lift-off nanolines.

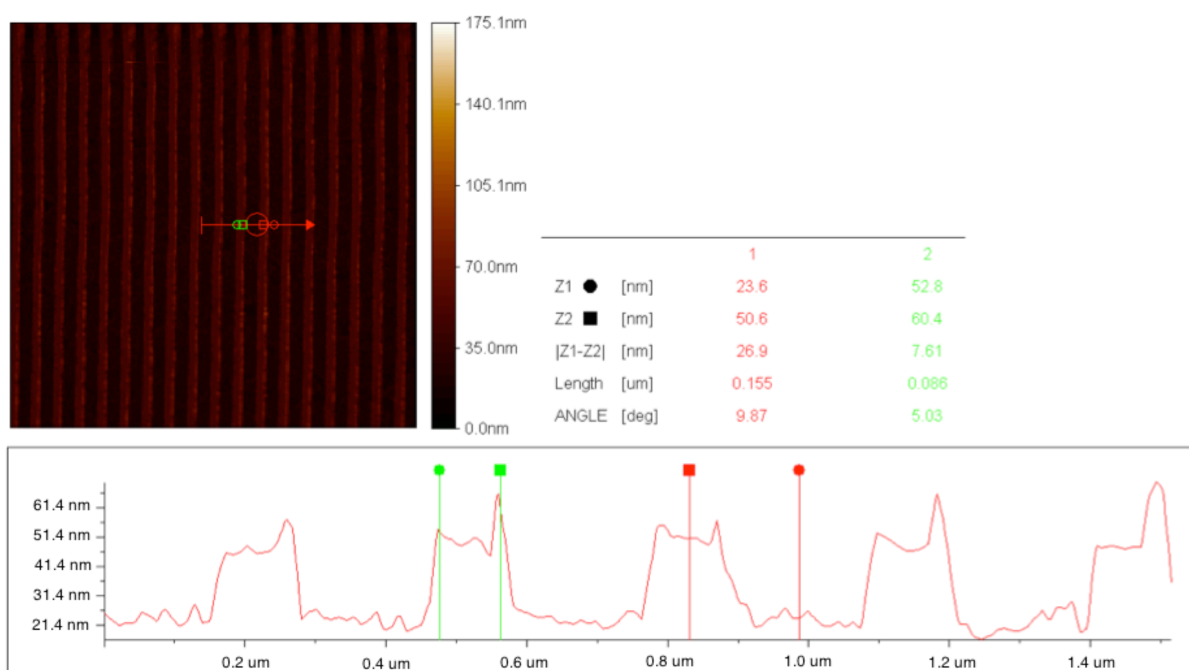

Figure 5.3 AFM image depicting a lift-off of 60 nm gold lines with a pitch of 250 nm on an ITO substrate.

Another technique used to get the gold nanolines or gratings on the ITO was the nTP or the nanotransfer printing whose working principle was described in section 2.6. Similar silicon stamps with structures of nanolines of 50 nm width with a pitch of 100 nm and another with a width of 200 nm with a pitch of 100 nm were used for the transfer. These stamps were evaporated with Gold and Titanium of similar thicknesses and pressed onto the ITO substrate to transfer the metallic lines onto the ITO. Figure 5.4 shows SEM images of the nanotransferred metallic gratings.

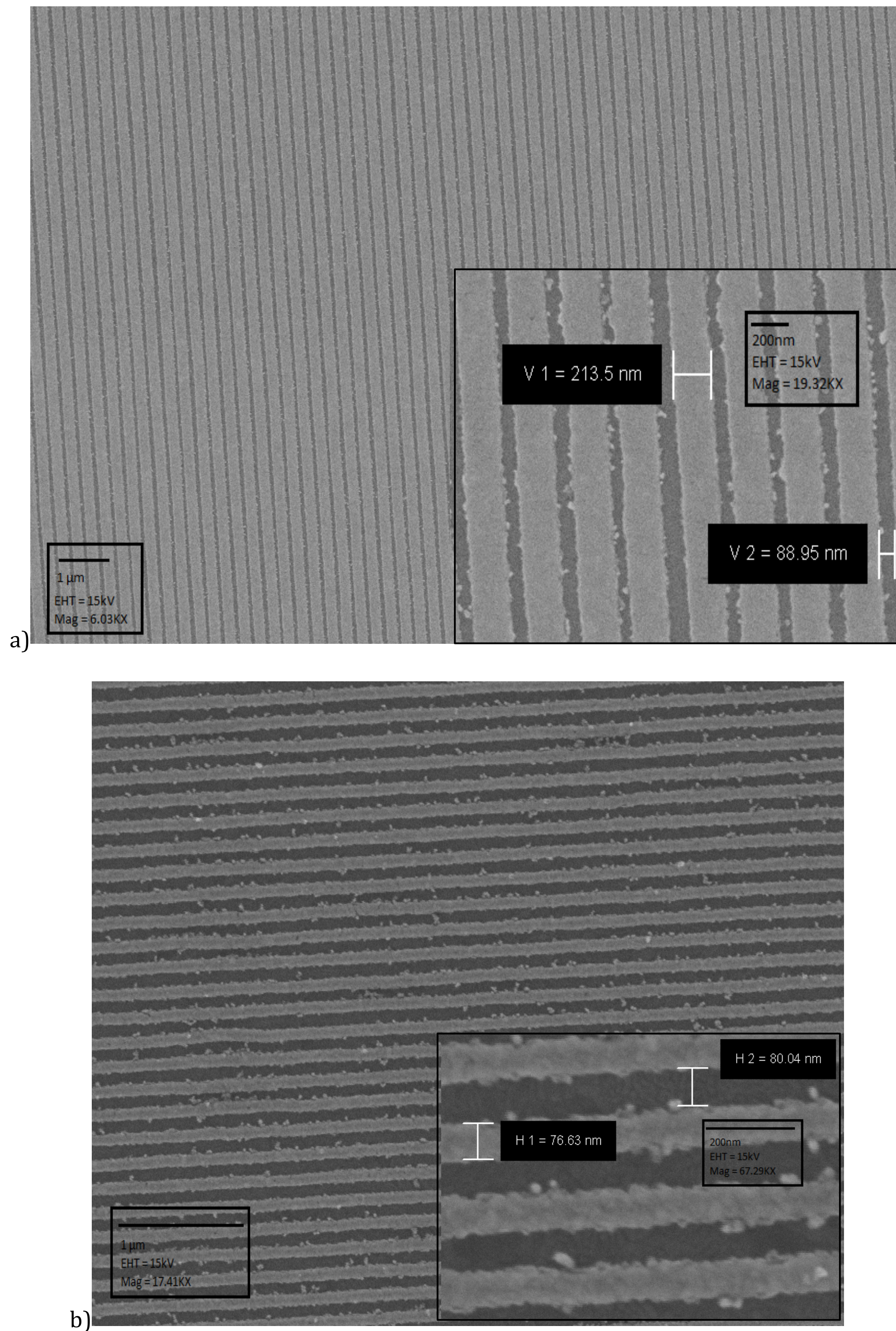

Figure 5.4 SEM images showing nanotransferred gold lines with a) 200 nm width and a pitch of 100 nm b) 50 nm width and a pitch of 100 nm. The insets show magnified images of the lines which depict the grainy nature of the transferred gold lines.

We notice that in the transfer process, the metallic gratings are very grainy and do not have sharp sidewalls. This could be because nanotransfer printing requires very high pressures on the stamp and substrate and gold being a soft metal, leaves behind some grains when the high pressure is pulled off. Therefore this technique of nanotranfer printing was not used throughout the experiments rather the focus was kept on using NIL.

The same procedure was applied to a glass substrate next instead of ITO. For all further optical measurements, samples with glass as the substrate were used instead of ITO. For good comparison and more detailed studies, the dimensions of the structures being imprinted were changed. Earlier we used a standard stamp with lines of 60 nm width and 250 nm pitch which is almost a 1:4 ratio of metal gratings to air as the dielectric. Next we changed the dimensions to 50 nm width lines and a pitch of 100 nm thereby increasing the ratio to 1:2 of metal to air. Figure 5.5 shows AFM images of gold lines with different metal heights after lift-off on glass as the substrate.

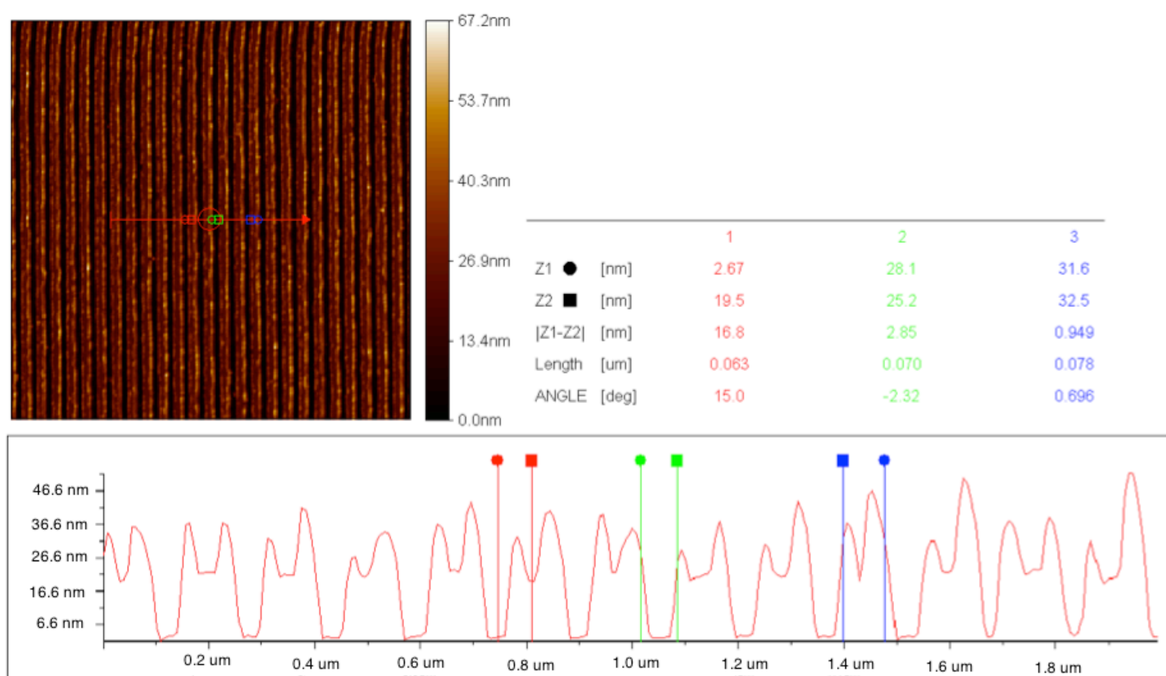

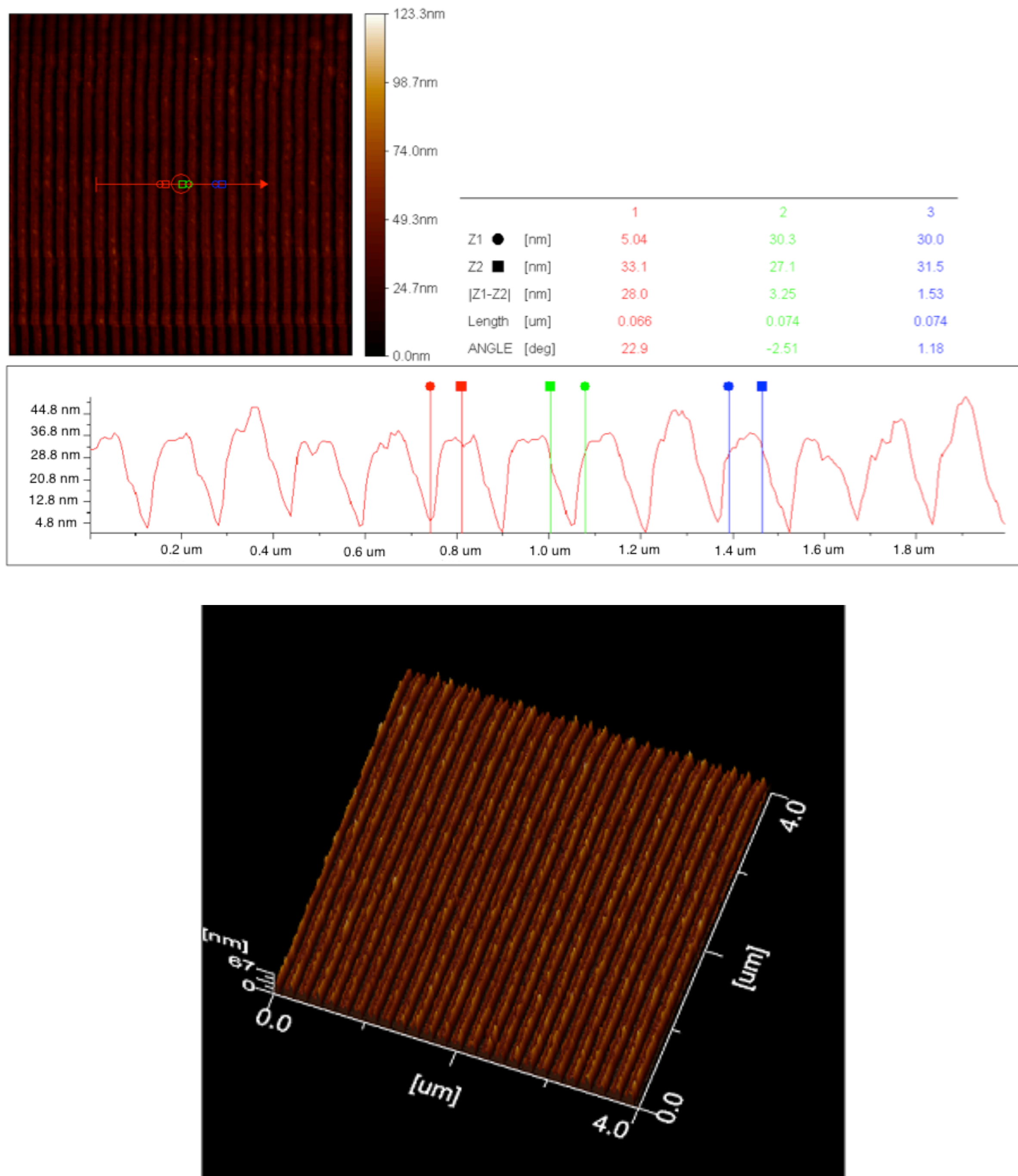

Figure 5.5 AFM images showing the gold lift-off lines on glass as a substrate. The dimensions of the lines are 50 nm wide with a pitch of 100 nm with 10 nm and 20 nm of metal deposited on the lines respectively. The bottom image is a 3D image which better depicts the metallic gratings.

5.4 Results and Discussion

After discussing about the fabrication techniques involved to get the desired metallic gratings, let's move on to the measurements and analysis of the samples. Simple optical measurements were done on the samples to try and understand the effect of gratings on the transmission and reflection spectra as compared to plain metallic films. In order to verify whether the experimental results obtained were correct or not, simulations were first performed on the metallic grating structures on glass. In the next section we will talk about the simulation results obtained first.

5.4.1 Simulation Results

Basic simulations were run on a very simple metallic grating structure keeping in mind the thicknesses and widths of the gratings. Figure 5.6 depicts a schematic of the simulation stack used. The metal used here is gold on glass as a substrate. The thickness, width and period of the gratings were altered to see the change in the optical spectra. The dielectric used was air with a refractive index of 1. The refractive index of the substrate which is glass is 1.5. Simple transmission of white light through the first layer of gold gratings and the reflected light were simulated. The polarization of the light was kept in mind therefore, the simulations were performed in two modes: TE mode or the transverse electric mode where there is no electric field in the direction of propagation and the TM mode or the transverse magnetic mode where there is no magnetic filed in the direction of propagation of light.

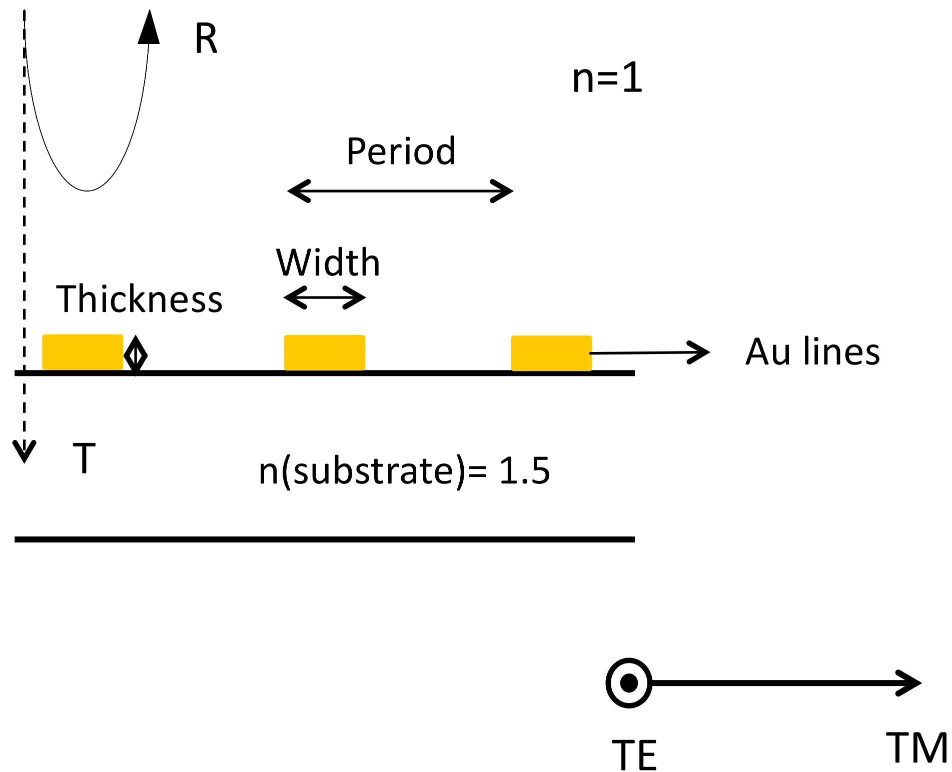

Figure 5.6 Schematic of the simulated gold gratings on glass with the two different propagation modes. The thickness, width and period were the variables whereas the refractive indices and the metal used were kept constant.

As we had a standard stamp of 60 nm wide lines and a pitch of 250 nm, the first simulations were performed keeping these dimensions in mind. Therefore, the width of the gold lines was fixed to 60 nm and the pitch to 250 nm and the transmission spectra was plotted in the two different modes as shown in figure 5.7.

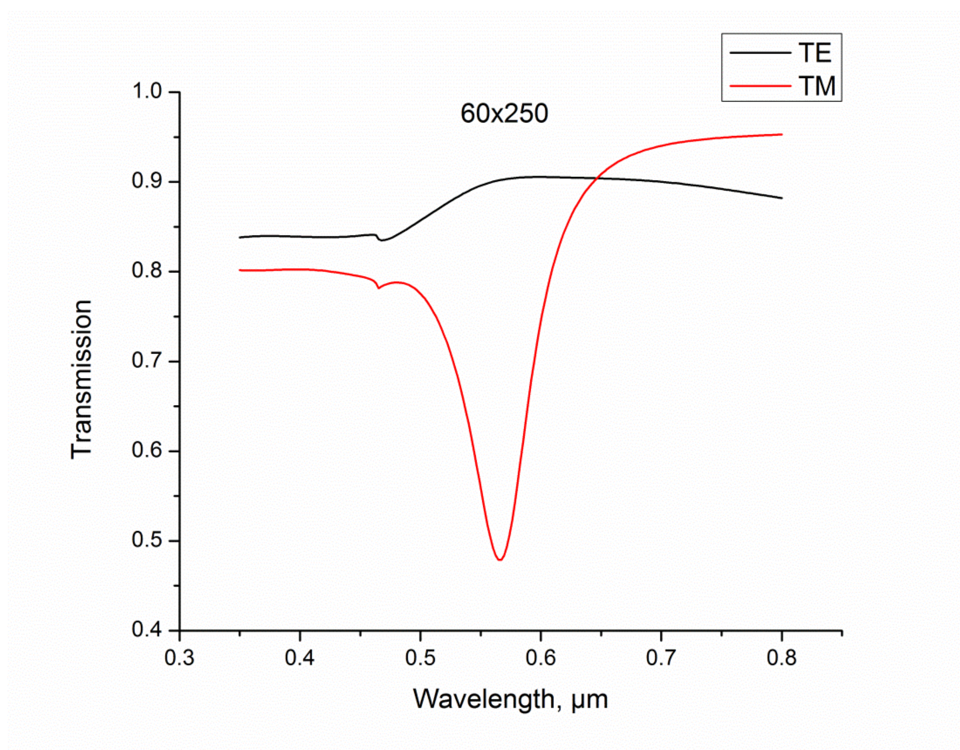

Figure 5.7 Transmission spectra of 60 nm wide gold lines with a pitch of 250 nm in the two different propagation modes of light.

We wanted to further understand how changing the width of the gold gratings and simultaneously the pitch would affect the optical spectra therefore, the next set of simulations were done varying the gold widths from 20 nm to 80 nm in steps of 20 nm and the pitch was varied in turn with respect to the width in ratios of 1:0.5, 1:1, 1:2 and finally 1:3. This means that if the width was kept at 40 nm, the pitch would be varied in steps of being half of the width first, then equal to the width, double the width and finally three times the width. Figure 5.8 shows a range of graphs plotted while varying the widths of the gold gratings and the corresponding transmission and reflection spectra.

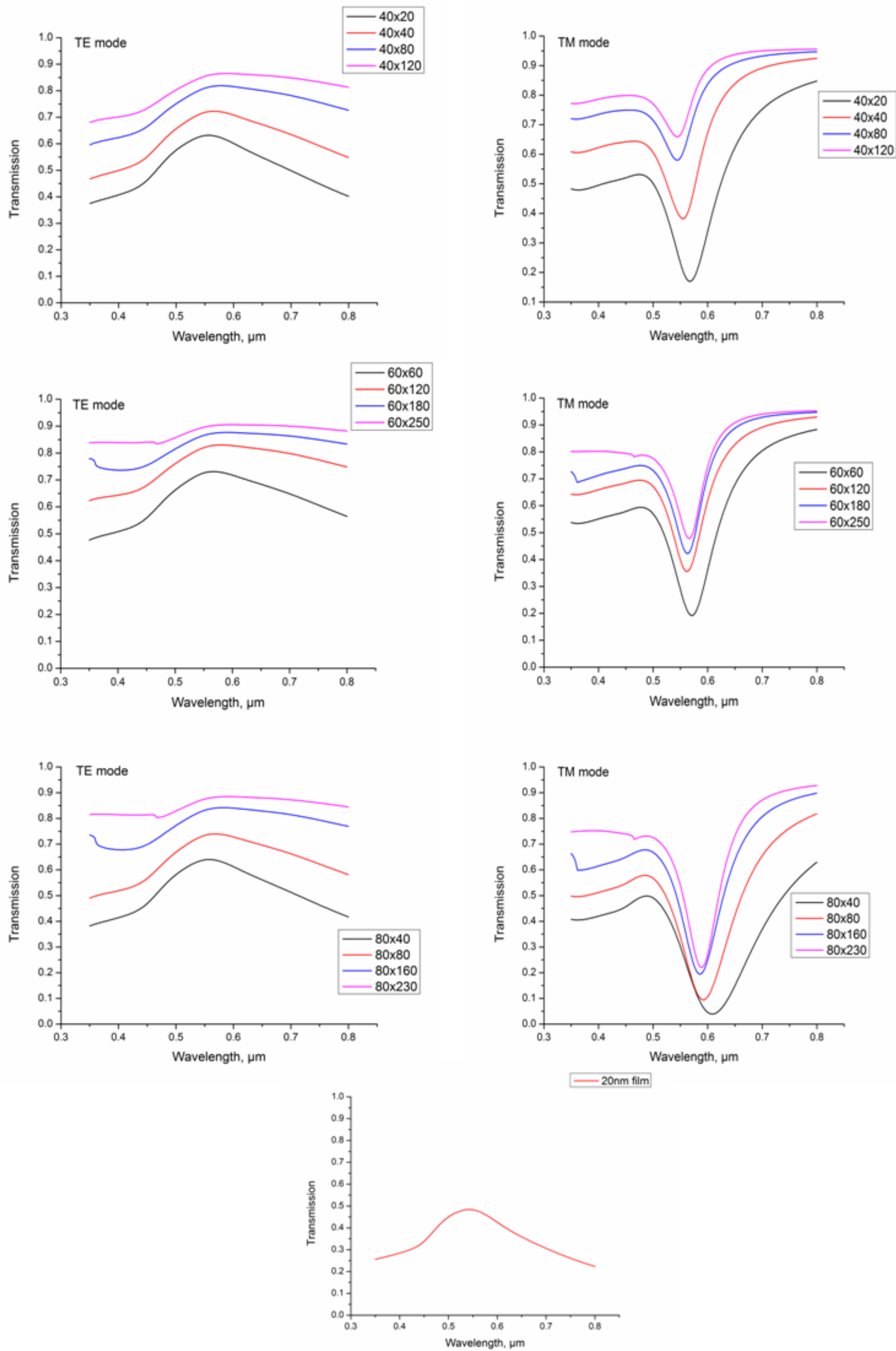
TE mode
40x20
40x40
40x80
40x120
Transmission
Wavelength, μm
TM mode
40x20
40x40
40x80
40x120
TE mode
60x60
60x120
60x180
60x250
TM mode
60x60
60x120
60x180
60x250
TE mode
80x40
80x80
80x160
80x230
TM mode
80x40
80x80
80x160
80x230
20nm film

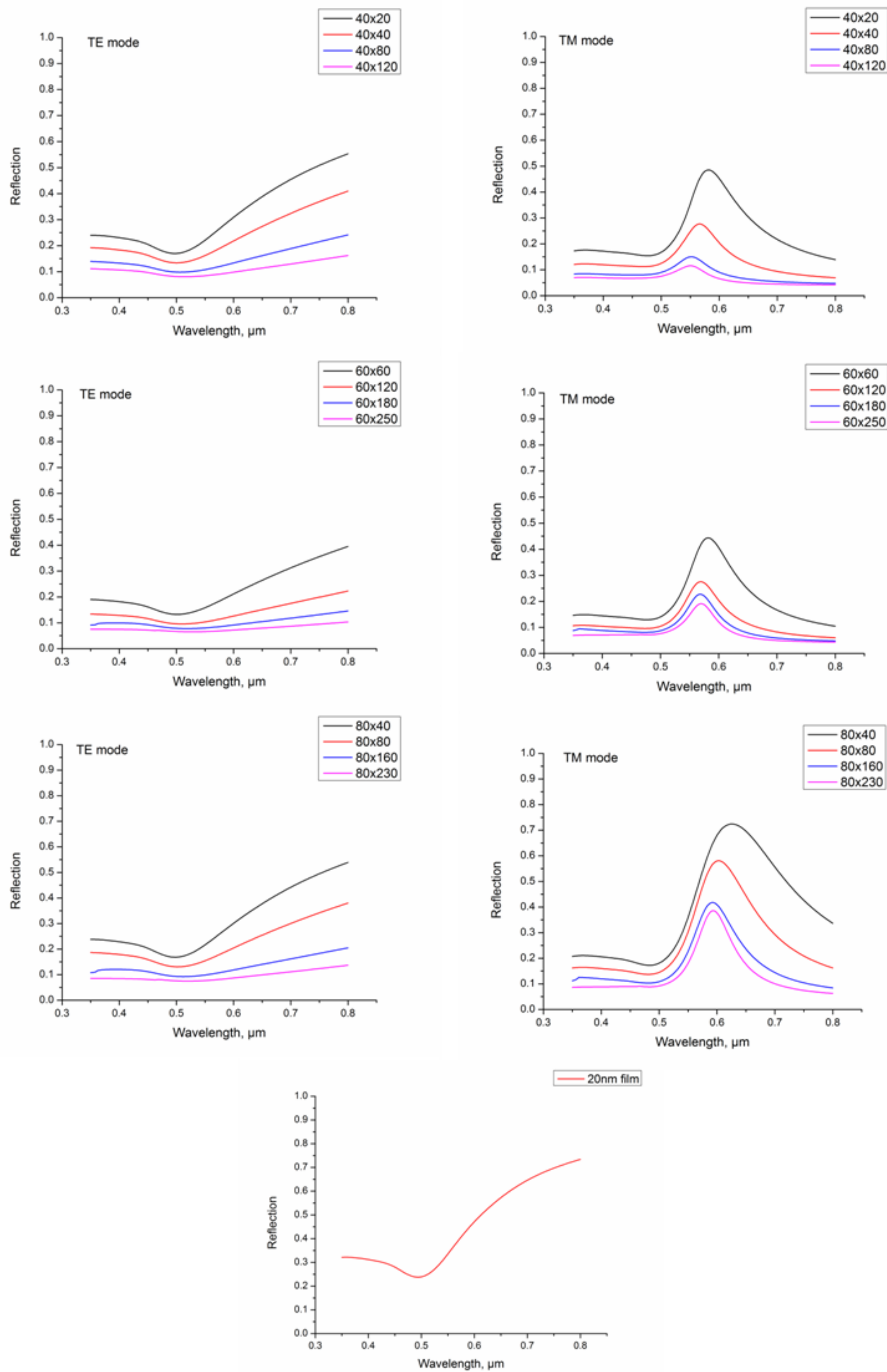

Figure 5.8 Transmission and reflection spectra of gold gratings with varying widths. The single graphs at the bottom depict the transmission and reflection of a plain gold film of 20 nm thickness.

Two different propagation modes were measured as shown in the figure above with keeping the width same and changing the pitch in the ratios described. We notice a gradual shift in the peaks and dips of the curves in the TM mode towards the left of the wavelength. As we increase the spacing between the gold gratings, the magnitude of the reflection spectra decreases considering there is less metal covering a given area and more glass. For different widths, we see a peak in the curves mostly centered around 550 – 600 nm which caters to the greenish-yellow section of the visible light. In fact, upon casual observation of the gold grating samples under the naked eye, they appeared to be greenish-blue as well. The reflection is at its lowest for the thinnest width of the metal grating which is 40 nm and highest for the thickest width which was 80 nm.

The bottom two graphs in both the images simply show us what the transmission and reflection pattern look like of a plain gold film of 20 nm thickness such that we can clearly see the effect of the gratings as compared to the plain film.

Based on these simulations, another set of graphs were plotted which basically depicted the ratio of the coverage of the metal over the gratings to the empty space between them, giving us an idea of how the optical spectra is dependent on the amount of metal there is on the gratings. The reflectance and transmittance was measured at 3 different wavelengths namely at 400 nm, 600 nm and 800 nm as these are the 3 wavelengths where the maximum difference is observed in the spectra as compared to a plain gold film. Figure 5.9 depicts these 3 graphs of transmission and reflection with respect to the area covered by metal.

For discussion let's take the case of coverage at 800 nm. As always the two different modes were plotted but we are more interested in the TM mode where we actually see a difference in the spectra. The data for all the four different widths (20, 40, 60 and 80 nm) was plotted with respect to the amount of area being covered by the metal. We observe that for all the widths, the transmission is highest for the least amount of area covered by metal which is understandable as most of the light is transmitted through the glass substrate. As we increase the area covered in metal, the transmission gradually decreases and is the lowest when the entire area is covered with gold. We have also observed from before that the transmission for a plain gold film is around 50% which is not the highest. And as can be seen from the graphs, the best case for highest transmission is thinnest width with the least amount of area covered in metal. These facts also hold true for reflection but reversed.

Coverage Graphs at 400nm

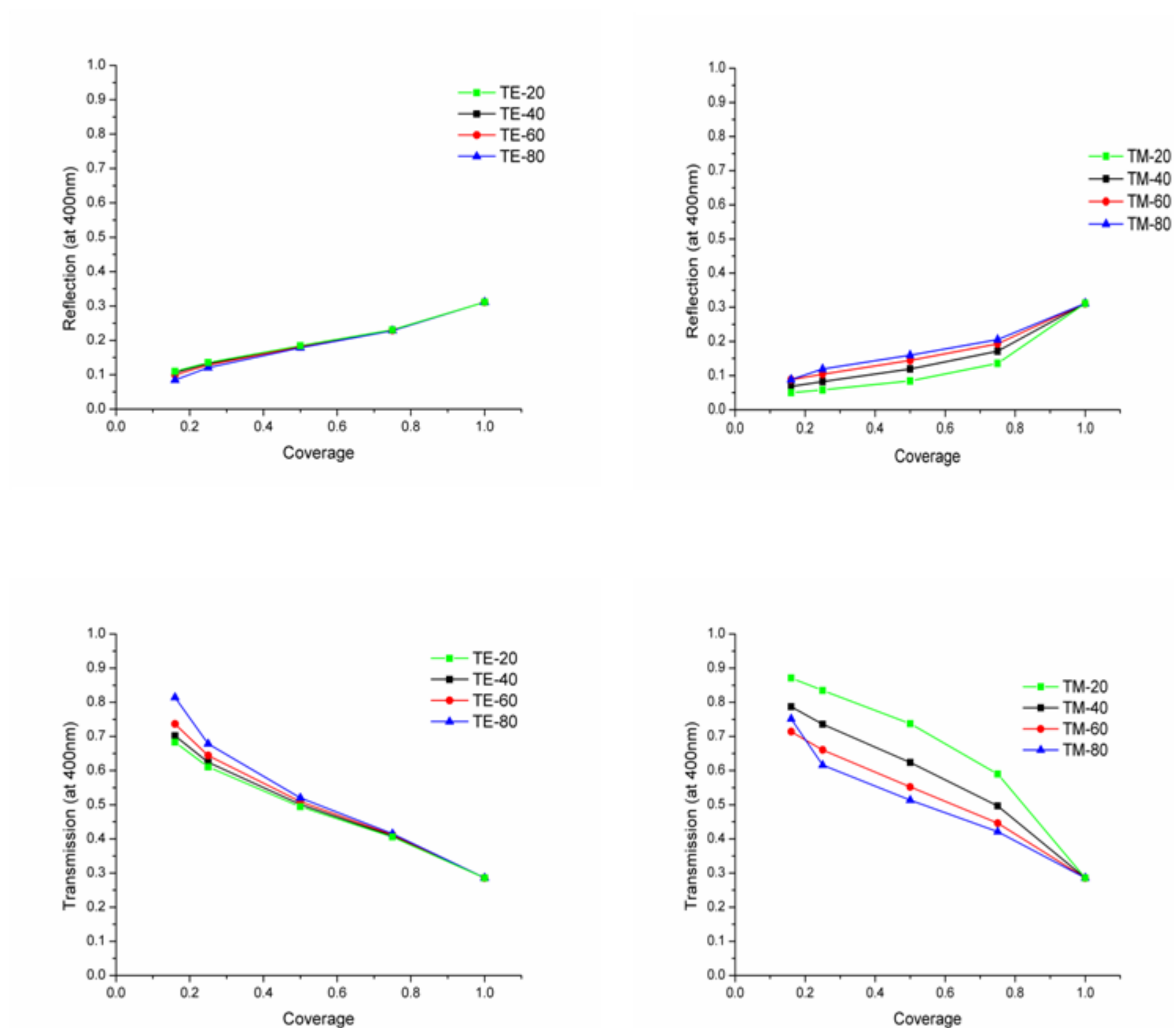

Coverage legend:
1.0 - area completely covered with gold (film)
0.5 - area comprising half of gold, half of spacings

Figure 5.9 A) Coverage graphs depicting the optical spectra of the gratings with respect to the area covered by metal at 400 nm.

Coverage Graphs at 600nm

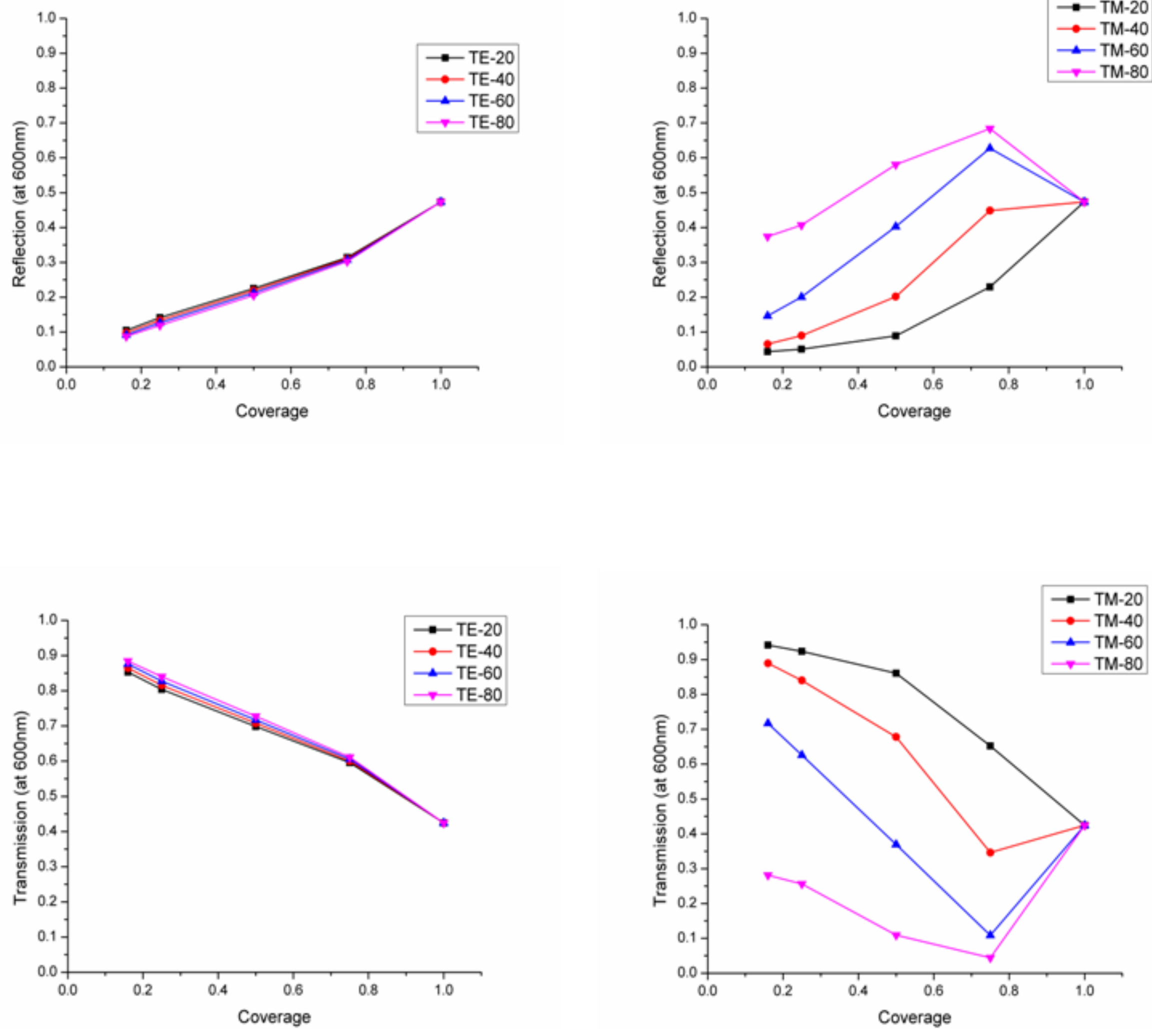

Coverage legend:
1.0 - area completely covered by gold (film)
0.5 - area comprising half of gold, half of spacings

Figure 5.9 B) Coverage graphs depicting the optical spectra of the gratings with respect to the area covered by metal at 600 nm.

Coverage Graphs at 800nm

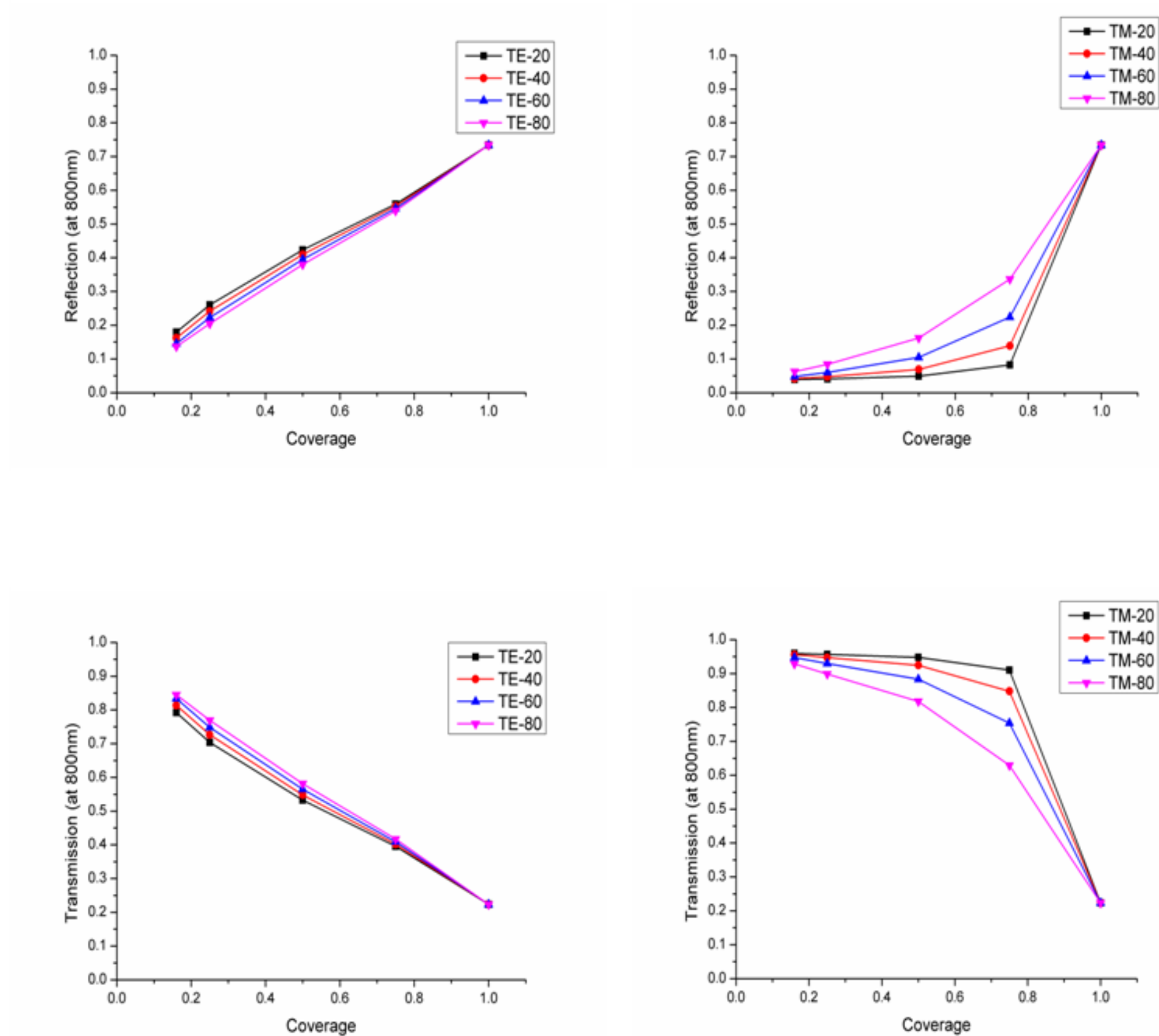

Coverage legend:
1.0 - area completely covered by gold (film)
0.5 - area comprising half of gold, half of spacings

Figure 5.9 C) Coverage graphs depicting the optical spectra of the gratings with respect to the area covered by metal at 800 nm.

We have discussed the dependence of the optical spectra on the width, pitch and amount of area covered with metal. Now let's talk about the dependence of the spectra on the amount or thickness of the metal deposited on the gratings keeping the pitch constant. Figure 5.10 shows a graph of transmission for gratings which are 60 nm in width and 250 nm in pitch which have been covered by four different metal thicknesses ranging from 10 nm to 40 nm. We observe that the transmission is highest for the thinnest metal and highest for the thickest one. This was also proven experimentally the result of which is also shown in the bottom graph of figure 5.10. Due to this being experimental, there is a lot of noise and interference which has to be taken into account while performing the measurements, therefore the magnitude of the transmission differs from the simulated results but the concept is still the same.

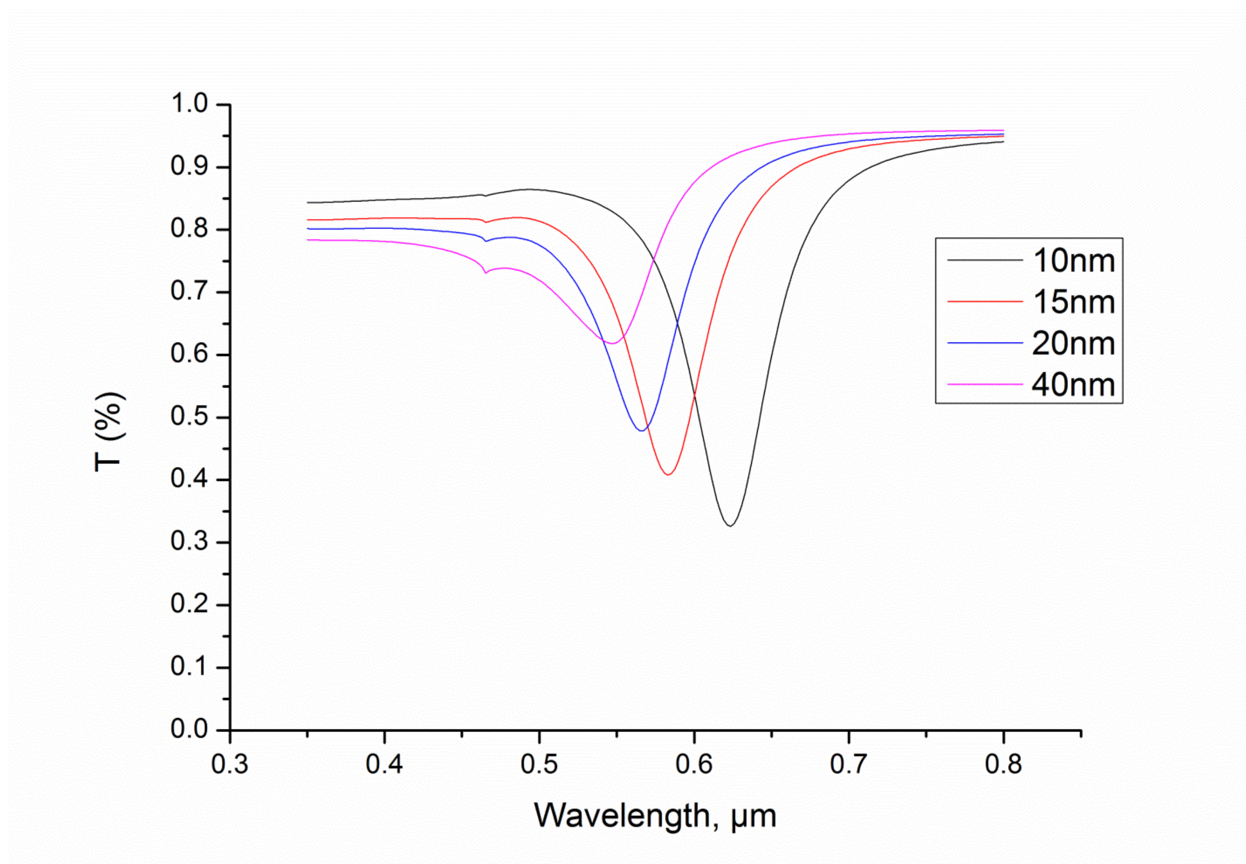

(a)

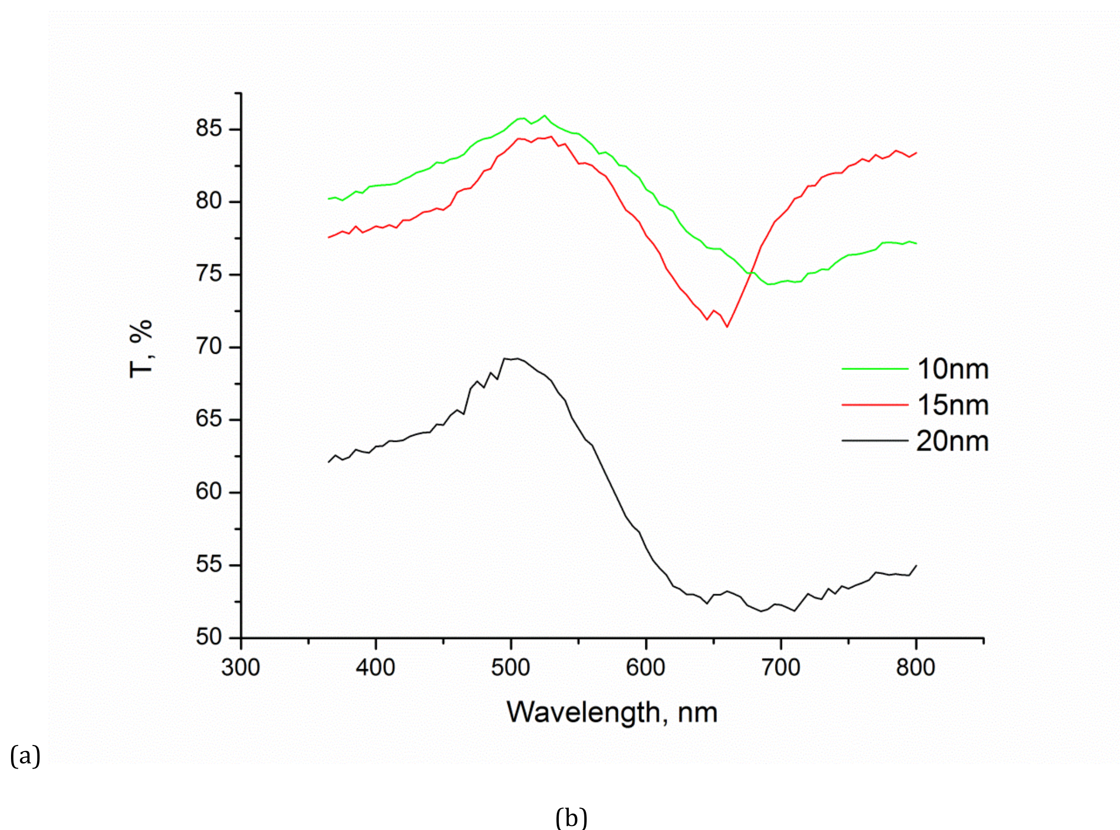

(b)

Figure 5.10 Simulated (a) and experimental (b) graphs showing the dependence of transmission on the amount of metal deposited on the gratings.

5.4.2 Experimental Results

Till now we have discussed about the optical spectra obtained upon simulating metallic grating structures with different dimensions varying the widths of the gratings, the amount of metal on them as well as performing coverage simulations depicting the dependence of the spectra on the area covered by metal. Now let us talk about the actual experiments performed and correlate them with our simulation results.

We have used two different dimensions of gratings as already explained in the previous section: 60 nm lines with a pitch of 250 nm and 50 nm lines with a pitch of 100 nm with the effort to differentiate the optical spectra dependence on width and pitch.

Let's start with the 60 nm gratings. It should be understood that the dimensions of the structures after the fabrication do not remain exactly 60 nm but become slightly larger by +20-30 nm. This happens during the etching of residual layer in the RIE. Although

RIE is anisotropic in its nature of etching, due to the plasma created, there is some additional etching of the sidewalls. Therefore, a 60 nm imprinted trench when put in the RIE comes out to be 80-90 nm wide thereby keeping the final width after metal deposition and lift-off to also 80-90 nm. Obviously if the width is enlarged, it is compensated in reduction of the pitch. So the final structure dimension in our experiments is 90 nm wide lines with a pitch of 220 nm. All the experiments and simulations are done keeping these dimensions in mind.

The optical set-up used for the experiments was a Newport spectroscope self assembled in our laboratory using a Silicon detector with a white light source. The dimension of the area of light shown on the sample was kept to 3x3 mm which was the smallest our set-up was capable of. The entire area of the imprinted gratings was almost 1x0.5 cm^2 for the 60 nm stamp used and 0.8 cm^2 for the 50 nm lines stamp. The lamp was turned on more than 30 minutes before performing the experiment in order to warm it up. First the measurements were done with unpolarized white light and then repeated again with a polarizer. Figure 5.11 depicts an image of a transmission measurement done on a sample with a plain gold film which is then compared to one of our samples with metallic gratings on them.

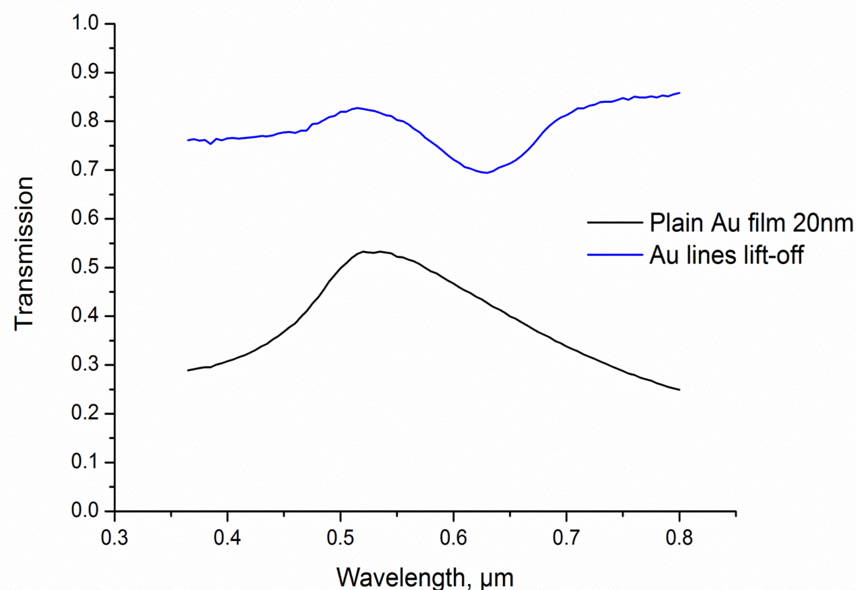

Figure 5.11 Compared transmission spectra of a plain gold film to that of metal gratings.

We observe a considerable enhancement in the transmission of gratings as compared to a plain gold film of 20 nm thickness. The transmission curve starts out as that of a normal gold film but with a higher transmission and then we notice a change in the curve around 630 nm where it shifts upwards. This change is also dependant on the pitch of the gratings as we have noticed the shift in the earlier graphs where a range of widths and pitches was plotted.

Apart from transmission, another aspect of the optical spectra was also plotted which is the reflection. Figure 5.12 shows a comparison of the simulated and experimental reflectance of a plain gold film and metallic gratings on a glass substrate.

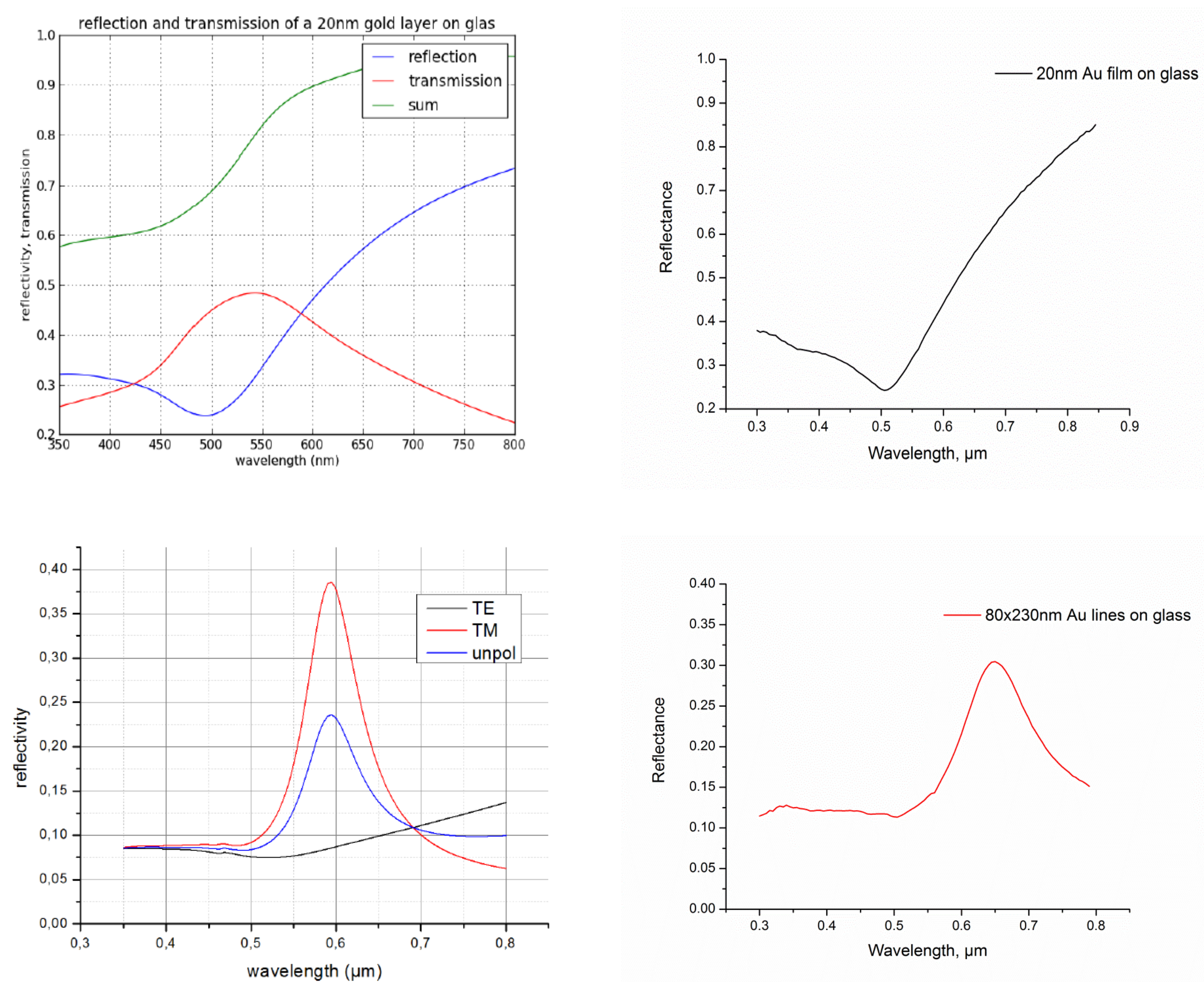

Figure 5.12 Simulated (left) and experimental (right) reflectance measurements of a plain gold film (top) and metallic gratings (below).

The transmission was also measured using a polarizer in two different propagation modes of light and figure 5.13 shows the comparison of simulated and experimental data of gratings of dimension 90 nm width and 220 nm pitch.

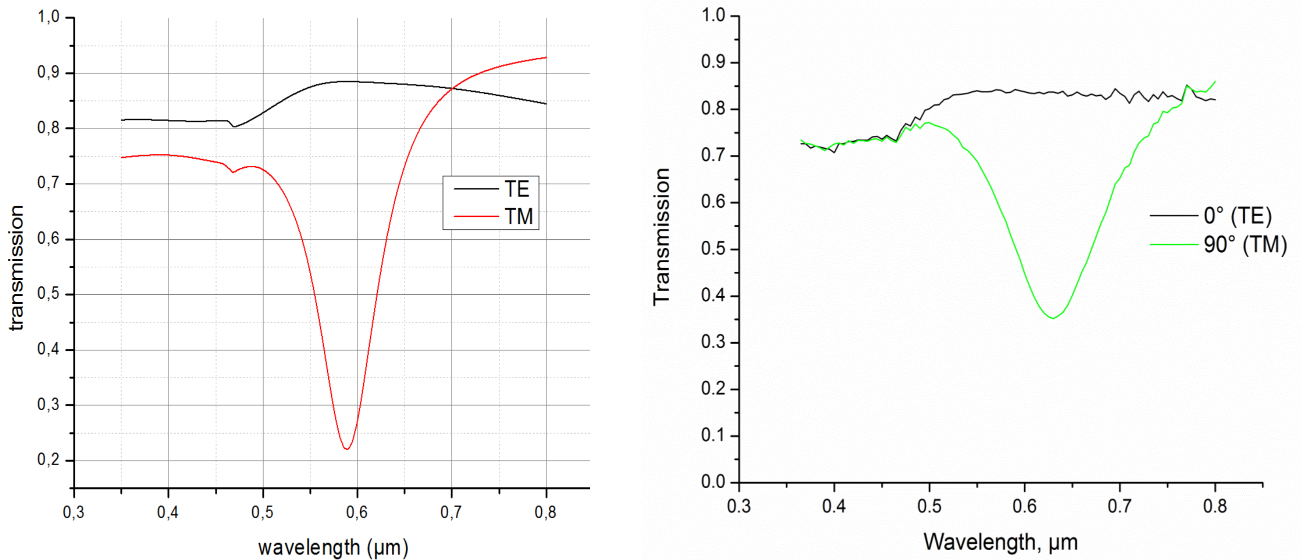

Figure 5.13 Simulated (left) and experimental (right) transmission spectra of 80 nm wide gratings on glass. The metal thickness is kept to 20 nm in each case.

The simulated and experimental data match quite well apart from the magnitude of the experimental data being less compared to that of the simulation. This is bound to happen considering that the simulation is for an ideal case and do not include any noise from the environment or errors.

Now let us compare the transmission spectra of both the dimensions of gratings, i.e. 60 nm width and a pitch of 250 nm and 50 nm width with a pitch of 100 nm using two different metal thicknesses. We have deposited 10 nm and 20 nm of gold on each of the gratings. As mentioned before, the dimensions of the gratings do not remain exact and change to 90 nm with a pitch of 220 nm and 70 nm with a pitch of 80 nm. Figure 5.14 shows four graphs plotting the transmission of these gratings with the above mentioned metal thicknesses.

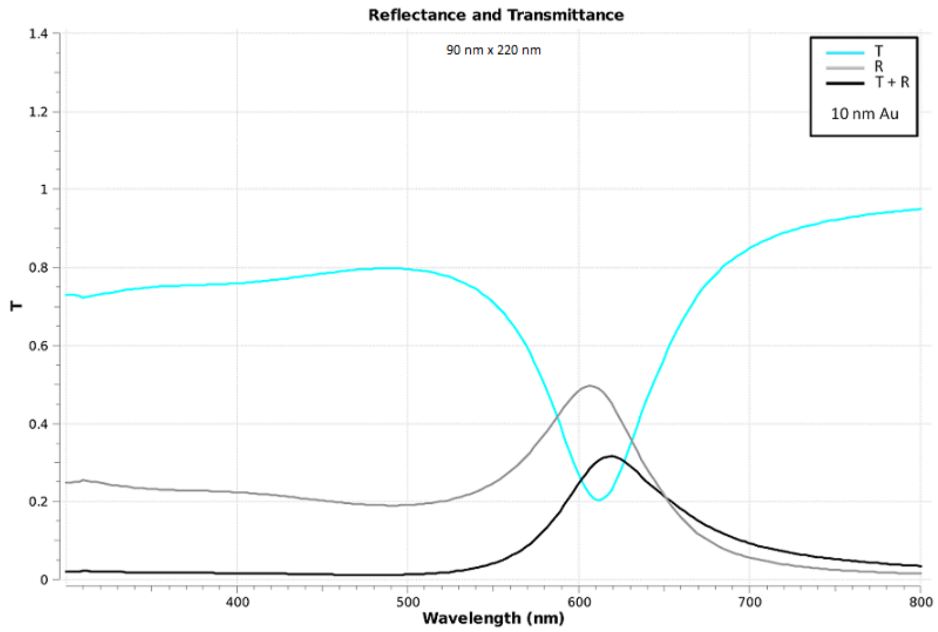
Reflectance and Transmittance
90 nm x 220 nm
T
R
T + R
10 nm Au
1.4
1.2
1
0.8
0.6
0.4
0.2
0
T
400
500
600
700
800
Wavelength (nm)

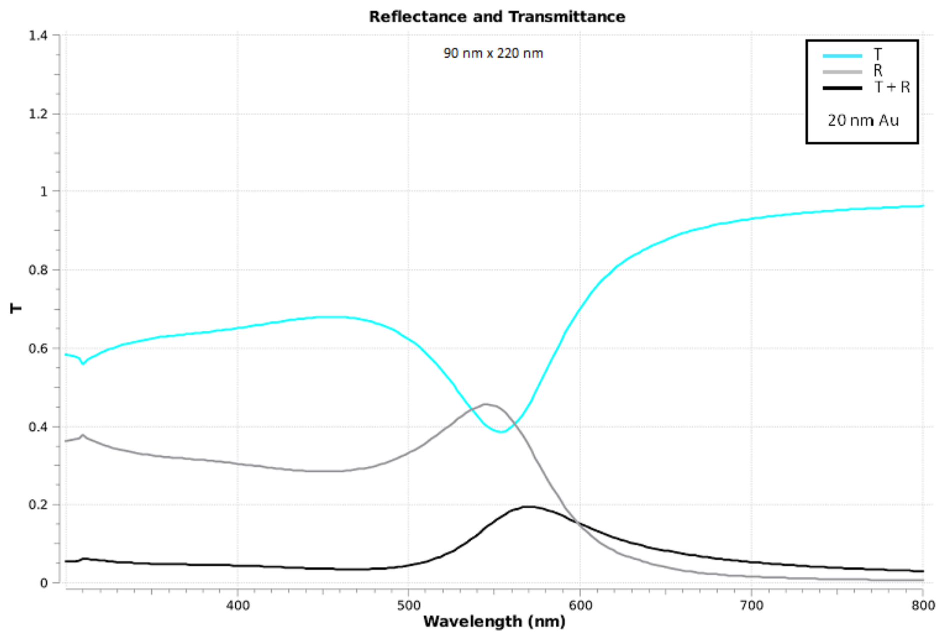
Reflectance and Transmittance
90 nm x 220 nm
T
R
T + R
20 nm Au
1.4
1.2
1
0.8
0.6
0.4
0.2
0
T
400
500
600
700
800
Wavelength (nm)

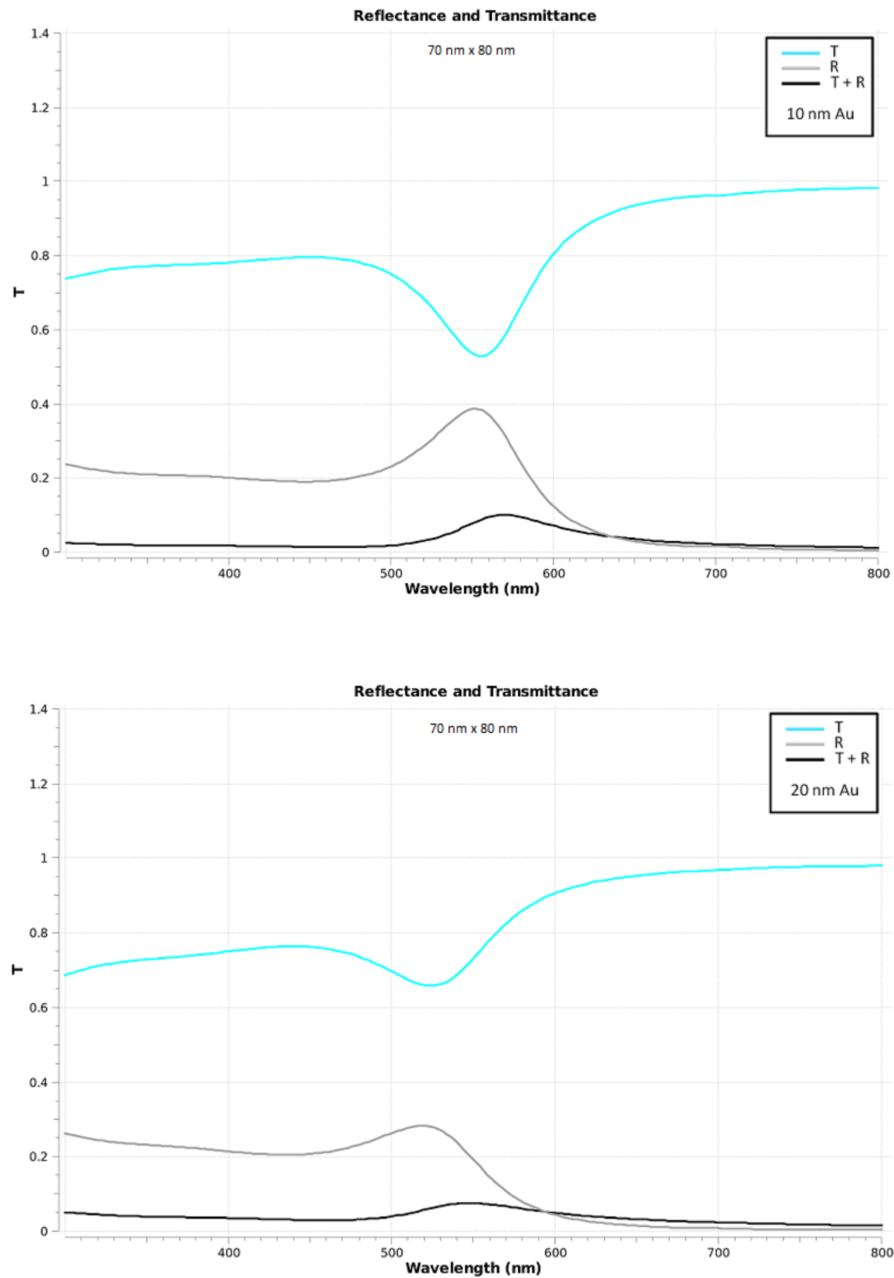

Figure 5.14 Graphs depicting the transmission (blue curve) and reflection (grey curve) spectra of 90 nm line (top two graphs) and 70 nm lines (bottom two graphs) with two different metal thicknesses of 10 nm and 20 nm.

As observed before, we can see that with lesser metal the transmission is higher so more light is transmitted through the thinner sheet of metal than the thicker one. Again we notice the dip in the curve shift with the amount of metal covering the gratings. The dip shifts towards the lower wavelength with more metal and this is also dependant on the width and pitch of the structures, more so on the pitch. The more the pitch, the dip is more around 600 nm and when we lower the pitch, the dip also shifts towards 550 nm which is around the bluish-yellow range of the visible spectrum as mentioned before.

5.5 Summary

We have shown the fabrication of plasmonic or grating structures using NIL and nTP as two different fabrication techniques which are metallic in nature. Preliminary simulations were generated to understand the behavior of these gratings optically with respect to the transmission and reflection spectra and compared to a plain metallic film. The simulations performed gave us an idea of the dependence of the optical properties on the width, pitch, thickness of metal and the amount of metal covering the area of the gratings. Furthermore, experiments were performed to correlate to the simulations in two different modes of propagation of light which resulted in similar results. The dimensions were also changed of the structures to see the difference in the optical measurements.

Further work on this would be to characterize the device in full electrically and optically to see if the efficiency of the device would change such that these gratings could be incorporated in an actual device for future research and development.

In the next chapter we will move to the second layer which is the PEDOT:PSS layer above the glass. This chapter is dedicated to purely patterning the PEDOT:PSS layer using different fabrication techniques and the challenges faced during it. We will introduce a novel method of patterning the desired layer.

Chapter 6

NIL for Organic Optoelectronic Devices

This chapter is a continuation of the previous one in terms of the device stack being used. After patterning the substrate with metallic gratings, we move up the stack to the organic PEDOT:PSS layer. This chapter is purely based on the fabrication aspect of patterning the PEDOT:PSS layer. Some research [80] has already been done on this in the past but due to reasons explained in the next section, PEDOT:PSS is not a very easy material to pattern. This chapter is dedicated to accounting the different types of fabrication methods used and a novel method devised to achieve our goal. We used NIL along with soft lithography using PDMS to pattern the layer. The aim of all the research described in the previous and current chapter is to increase the efficiency of the device we already talked about. By patterning the organic layer, we are trying to observe an enhancement in the optical and electrical properties of the device. The next section will give a brief overview of organic electronics and the polymer being used, PEDOT:PSS, before moving onto the further sections describing the process and results in detail.

6.1 Introduction

Besides the established silicon based electronics, the new field of organic electronics technology has gained a lot of interest during the last decade. Organic electronic devices are based on conjugated molecules or polymers and are promising candidates for the manufacturing of environmentally safe, flexible, lightweight and inexpensive electronic

devices which can be used in low cost applications. Since the invention of conjugated polymers in the mid 1970s, a significant approach in their research was done to understand their chemistry better. Conjugated polymers have spatially extended π-bonding system which offers unique physical properties. Different electric components are made of organic electronics like OLEDS, solar cells, sensors and transistors. Some of the above mentioned fields are already out in the market whereas others are still in research. The flexibility which can be achieved by the chemical tailoring of desired properties as well as the inexpensive technology which is already well developed for traditional plastic applications together makes organic electronics and interesting field. The efficiency of different polymer electronics can be enhanced if the different layers are structured of the behavior of a device can be changed. A lot of research was done in the structuring of conductive polymers and the applications of structured polymer films are a growing research area. Commonly used methods for patterning are photolithography, micro moulding and nanoimprint lithography. These methods are limited by material parameters of the structured polymers. A lot of research has been done on structuring P3HT [81] or other metal layers on or between the metal layers. These processes are well developed and the results are satisfactory but the structuring of the often used PEDOT:PSS layer is not well developed and upto the mark. The most common method of structuring common PEDOT:PSS is laser ablation [82], NIL or micro transfer. Even in these methods, the processes are complicated and the height of the structures is low and often the addition of plasticizer is necessary. The properties of organic electronics can be changed and adapted to specific applications and their processing and chemical functionality can be changed during the synthesis. Likewise, a novel process based on new scientific findings in the chemical structure of the PEDOT:PSS is developed. The resulting structures are analyzed and their optical behavior is examined. Next we will talk about the organic material PEDOT:PSS, its properties and why is it difficult to pattern it in its normal state.

6.2 PEDOT:PSS

PEDOT or poly(3, 4 ethylenedioxythiophene) is a polythiophene derivative which was found to have interesting properties like a high conductivity and transparency. It is an insoluble polymer in all common solvents and is very unstable in its neutral state as it oxidizes quickly in air. In most applications doped PEDOT is used as film formation with pristine PEDOT is difficult. It can be made soluble by using a water soluble polyelectrolyte, poly(styrenesulfonate), abbreviated PSS. The molecular weight of PSS is higher than that of PEDOT. PSS has two functions, one is to be a source for the charge balancing counter ion, the other is to keep the PEDOT chain segments dispersed in the

aqueous medium. PEDOT:PSS consists of a conducting polycation (PEDOT) and polyanion (PSS). The addition of PSS leads to improved process ability but it also decreases the conductivity.

PEDOT is transmissive to visible light and it is cathodically colored transparent sky blue in the doped and conducting state, as the band gap is located at the transition between the visible and near infra red regions of the spectrum.

When they are both mixed, they form a complex which is not really water soluble, but it forms a stable, deep blue colored micro dispersion. It was first used as an antistatic coating for photographic films to avoid electrostatic discharge, as a counter electrode in electrolyte capacitors and high-power Li-batteries, because of its electronic and ionic conductivity. It is also widely used in the emerging field of organic optoelectronics as a buffer layer, between Indium Tin Oxide (ITO) and as an active organic layer. Applications are as a conductive layer in organic thin film transistors or hole transport layer in OLEDs. Future applications for PEDOT:PSS which are possible due to improved conductivity by secondary doping and new pattern techniques, are as flexible and transparent electrodes in field effect transistors, LEDs and photovoltaic cells.

PEDOT:PSS has very interesting properties like a relatively good electrochemical and thermal stability of its electrical properties and good optical properties compared with other conducting polymers. The advantage of PEDOT:PSS is its long lifetime and the relatively stable work function (PEDOT:PSS film 5.2eV [83]) in comparison with inorganic oxides. It is normally used in a bi-layer configuration with an ITO contact due to its relatively low charge mobility, but it can be modified to be used as an anode. When PEDOT:PSS is used in light emitting devices, it works usually as a hole transport polymer which is spin coated on a clean ITO substrate. It smoothes the surface of the ITO substrate and its higher work function as compared to ITO is good for hole injection due to the lower height of the injection barrier. Therefore, an efficient luminance can be achieved but it is not good for devices which emit blue light. The work function of PEDOT:PSS is not good for blue light as the HOMO level is too low [84].

The electronic properties of PEDOT:PSS can be varied widely depending on the solid content, doping concentration, particle size and additives. The conductivity of PEDOT:PSS is one or two orders of magnitude lower than that of other good conducting polymers and about three orders lower than that of ITO[85]. However it can be improved by more than one order of magnitude by adding polyalcohols e.g. sorbital or glycerol.

6.2.1 Glycerol doped PEDOT:PSS

Recent studies have demonstrated that the conductivity of PEDOT:PSS films can be dramatically increased by adding a high boiling liquid additive such as glycerol or sorbitol. The additives are normally added after polymerization and before the spin coating. These solvents are often called 'secondary dopants' while PSS is the primary dopant. The exact mechanism of the conductivity improvement in PEDOT:PSS with the addition of secondary dopants is still open to debate [86], but it seems that the effect is independent if the dopant remains in the PEDOT:PSS after drying or evaporates.

The adding of glycerol as a plasticizer decreases the inter chain interactions and helps at the reorientation of the polymer chains at high temperatures (150°C) so that better connections between the conducting chains of the PEDOT molecules are formed.

For the purpose of experimentation in this chapter, the secondary dopant used is glycerol. Further reference to glycerol doped PEDOT:PSS in this chapter will henceforth be termed as G-PEDOT:PSS. Mixing PEDOT:PSS with glycerol increases its conductivity three fold [87]. The electrical conductivity is increased by an increase in the hopping transport and in the connectivity among the conducting grains, an increase of doped PEDOT at the surface of the grains and the delocalization of electrons [88]. But the doping has no observable effect on the work function of PEDOT:PSS [89], therefore the hole injection barrier is not changed and the conductivity of the PEDOT layer and the current density are increased. The used amount of glycerol depends on the application and should be aligned in order to get the best results. The reason behind enhanced parameters of PEDOT:PSS because the PEDOT:PSS chains expand upon adding glycerol which leads to an improved chain organization. Another major improvement is also the resistance of G-PEDOT:PSS to air moisture is better than that of pure PEDOT:PSS films and they even showed a good performance after they were immersed in water [90]. The doping with glycerol reduces also the operating voltage of devices compared to that with PEDOT:PSS, as shown by [91]. Zhang et al. [92] reported that solar cells with G-PEDOT:PSS show a higher performance than pure PEDOT because the colloidal PEDOT rich particles swell and aggregate and enhance the conduction.

6.3 Materials

6.3.1 Substrate

In this research, three different types of substrates are used: standard glass substrates, silicon wafers and quartz wafers. The material properties are described below.

6.3.1.1 Silicon wafer

A standard p-doped 2” wafer is used for the purpose of our experiments. The thickness of the wafer is between 256 and 306 μm. The silicon wafer is used for preliminary experiments only as the ultimate goal is to pattern PEDOT:PSS on a glass/quartz or in other words, a transparent substrate.

6.3.1.2 Glass substrate

Standard microscopic glass slides are used for the experiments in this chapter. They are produced by Menzel- Gläser. The size is 26x76 mm and their thickness is 1 mm. the surface wettability is good and the transmission in the total region of the UV-A spectrum is high around 90%. The refractive index is 1.5 and for the purpose of ease of experiments they are cut into the size of 26x 25 mm pieces.

6.3.1.3 Quartz wafer

The used quartz wafers are made out of a clear borosilicate glass (D 263 T eco produced by SCHOTT). The quartz wafer surface is highly polished which is the main reason for using it later on in our research to have a very homogenous spin coated layer of PEDOT:PSS. It is a very thin glass with a high chemical resistance and high transmission ~ 91.7%, refractive index of 1.52. The diameter is 50.8 ± 0.5 nm and the thickness is 0.5 ± 0.3 nm. The wafer is again cut in to 18x18 mm pieces.

6.3.2 PEDOT:PSS

The PEDOT:PSS used in this research was bought from CLEVIOUS. Three different versions of PEDOT:PSS were used with different conductivities namely CLEVIOUS PH 1000 with the maximum conductivity, CLEVIOUS P VP Al 4083 with medium conductivity and finally CLEVIOUS P VP CH 8000 with the least conductivity.

6.3.3 NIL thermal resist

mr-I 8000R bought from Micro Resist technology GmbH was used as the thermal resist for all the nanoimprinting purposes. The T_g of this resist is 105 °C. Two different version of this series was used to obtain two different spin coated thicknesses: 8010R for 100 nm thickness and 8020R for 200 nm thickness.

6.3.4 Master mold

Initially a DVD stamp made of nickel with structure width ranging from 400 nm to 1 µm was used to make copies into PDMS. The height of the structures was 150 nm. To further move down into the nm regime, we shifted to silicon master molds the features of which are described as follows: an 8x8 mm structured area with lines of 60 nm diameter and 250 nm pitch.

6.3.5 PDMS

The most widely used elastomer for soft lithography is Polydimethylhexathiophene (PDMS). It is a silicone resin and consists of a mixture of vinyl-terminated PDMS and trimethylsiloxyterminated poly(methylhydo-siloxane) polymer and a highly cross-linked three-dimensional structure. The elongation at break point is high but the modulus is low which leads to structural problems in the pattern transfer elements especially for nanometer structures. The s-PDMS or soft PDMS used in this research is the Sylgard 184 Silicone Elastomer bought from Dow Corning.

The h-PDMS or hard PDMS was developed by an IBM group with a relatively high compression modulus to solve the problems associated with s-PDMS. The chain length of h-PDMS is relatively short, so the modulus is high but its elongation at break point is much lower. The main problem with using h-PDMS is its brittleness. It has four major components which are as follows: the PDMS prepolymer (vinylmethylsiloxane-dimethylsiloxane VDT-731) bought from ABCR GmbH, a platinum catalyst (platinumdivinyltetramethyldisiloxane complex in xylene) from Gelest Corp, a modulator (2, 4, 6, 8- tetramethyl- 2, 4, 6, 8- tetravinylcyclotetrasiloxane as inhibitor) bought from ABCR GmbH, and a hydrosilane prepolymer (methylhydrosilane-dimethylsiloxane as copolymer) bought from Gelest Corp. The recipe used will be described later on in the next section.

6.4 Fabrication

In this section firstly we describe the fabrication details of preparing the stamps for our imprint process and the problems encountered during this process.

6.4.1 Stamp Preparation

In this section we talk about preparing PDMS copies from our silicon master molds. The reason behind using flexible soft stamps to imprint PEDOT:PSS as compared to hard stamps is because of the hard nature of the PEDOT:PSS blend. As already mentioned, the chemical properties of PEDOT:PSS do not change much from 20°C to 200°C. Therefore, in order to pattern it we require soft stamps which can conform to the polymer surface better than hard stamps. Thus, the use of PDMS for preparing copies from the master molds. PDMS ensures adhesion between stamp and the substrate over a large area without any pressure because of its low Young's modulus (~750KPa), its low surface energy (21.6 nN/m) and the ease of release from the imprinted structures. The surface of PDMS is highly hydrophobic and the high fracture robustness allows the use over a wide temperature range [93]. PDMS is transparent down to a light wavelength of 256 nm making it possible to use these stamps for UV-NIL. Its main advantage is that it is commonly available, easy to use and inexpensive. But some of these advantages are also disadvantages when it comes to certain applications. Its low Young's modulus limits the fabrication of high aspect ratio structures because they collapse, merge or buckle. Deformations and distortions can take place during the replication because of the high elasticity and thermal expansion. The resolution of the replicated structures is limited by the physical properties of the material- if the physical toughness is too high, they tend to fracture or crack. The shrinkage of PDMS after curing at high temperature is ~1%.

6.4.1.1 Replica Molding

This technique is used to fabricate the PDMS stamps from the master molds which are silicon and basic DVD stamps in our case. Replica molding is widely used to duplicate the shape, morphology and structure of the mold and fabrication of multiple copies is simple, reliable and inexpensive. The conformity of the replication technique depends on the van der Waals interactions, wetting and kinetic factors such as filling of the mold which allows accurate replication of small features (<100 nm). Typically UV or thermally curable prepolymers are used as their shrinkage is usually lower than 3% after curing, their replicas have the same dimensions and topologies as the mold.

Figure 6.1 shows a schematic of the steps involved in replicating a mold into PDMS. The standard recipe for PDMS is to mix the polymer base and the curing agent in a weight ratio of 10:1. The mixture is stirred for 5 minutes and degassed in a desiccator to remove trapped air bubbles as the mixture has to be smooth before pouring it onto the master mold. Any additional air bubbles will result in non homogenous replica as the air bubbles will also get cured on the structures of the stamp. The PDMS is then poured on a rigid mold (Si or Ni) and the polymer is cured by heat or UV light. After cooling down, the PDMS stamp is then peeled off and it results in a negative pattern of the mold. Lower curing temperatures are better to reduce the roughness and avoid tensions inside the material due to thermal shrinkage. This way the master mold is protected from any undue damage and can be used to make multiple replicas in PDMS.

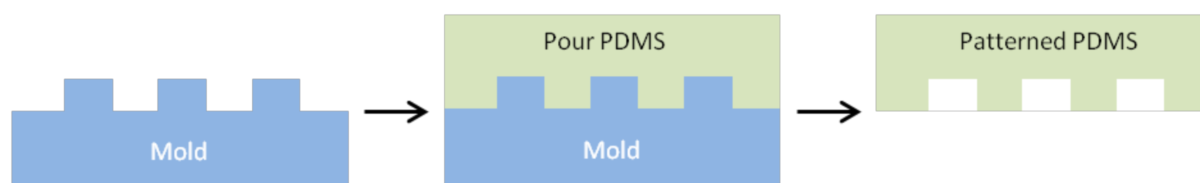

Figure 6.1 Mold replication into PDMS.

Using replica molding, we fabricate a number of PDMS stamps starting with 50 µm line structures due to the ease of fabrication of micro meter structures in PDMS as compared to nano meter. A silicon wafer with 50 µm line structures was prepared using optical lithography and a PDMS replica of that made.

The next set of master mold used for replication was the DVD stamp made of nickel. The structures in this were smaller than the 50 µm ones. The dimensions ranged from 400 nm to 1 µm in length and around 70 nm in width. The height of the structures was around 150 nm. Figure 6.2 shows a microscopic image of the replicated 50 µm PDMS stamp and an AFM image of a replicated DVD stamp in PDMS.

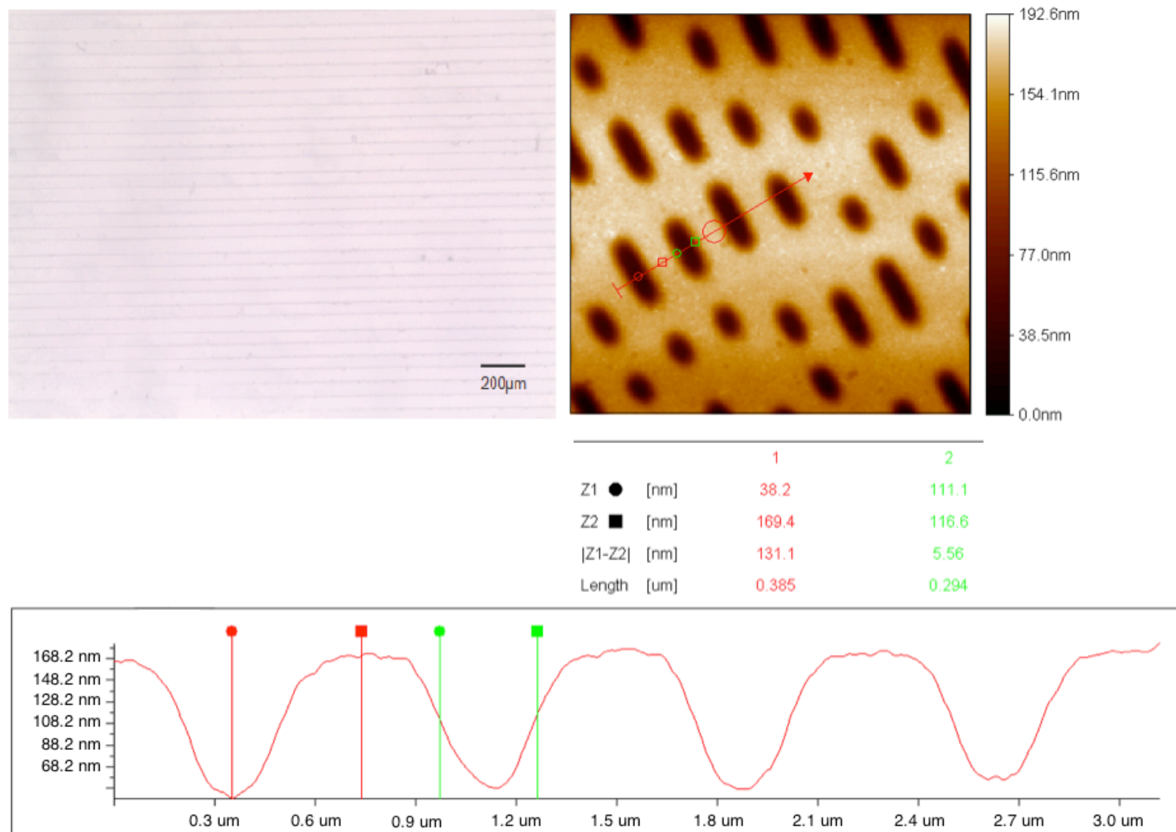

Figure 6.2 a) Replicated 50 µm lines stamp b) replicated DVD stamp in PDMS.

Finally after achieving good replicas with the micrometer and DVD stamps, a PDMS copy of a stamp with nano meter structures was made. The master mold used here was a silicon stamp with 60 nm line structures and a pitch of 250 nm. The height of the structures was around 90 nm. The replication was successful but unfortunately the height of the structures replicated was not good at all as shown in figure 6.3 in the image on the bottom, therefore this stamp could not be used for an imprint later on. The depths of the replicated structures depend strongly on the viscosity of the material used and the geometry of the structures being replicated. The viscosity of PDMS is high (3500 mPa*s) and therefore the cavities of the mold are not completely filled. The resolution is limited by an inappropriate material flow into the cavities for structures in the sub 100 nm range [94]. A possibility to lower the viscosity is to dilute the PDMS with a solvent. Koo et al. used toluene to lower the viscosity of PDMS and they demonstrated imprints of dot arrays in the sub 50 nm range with a structure depth of 110 nm [95].

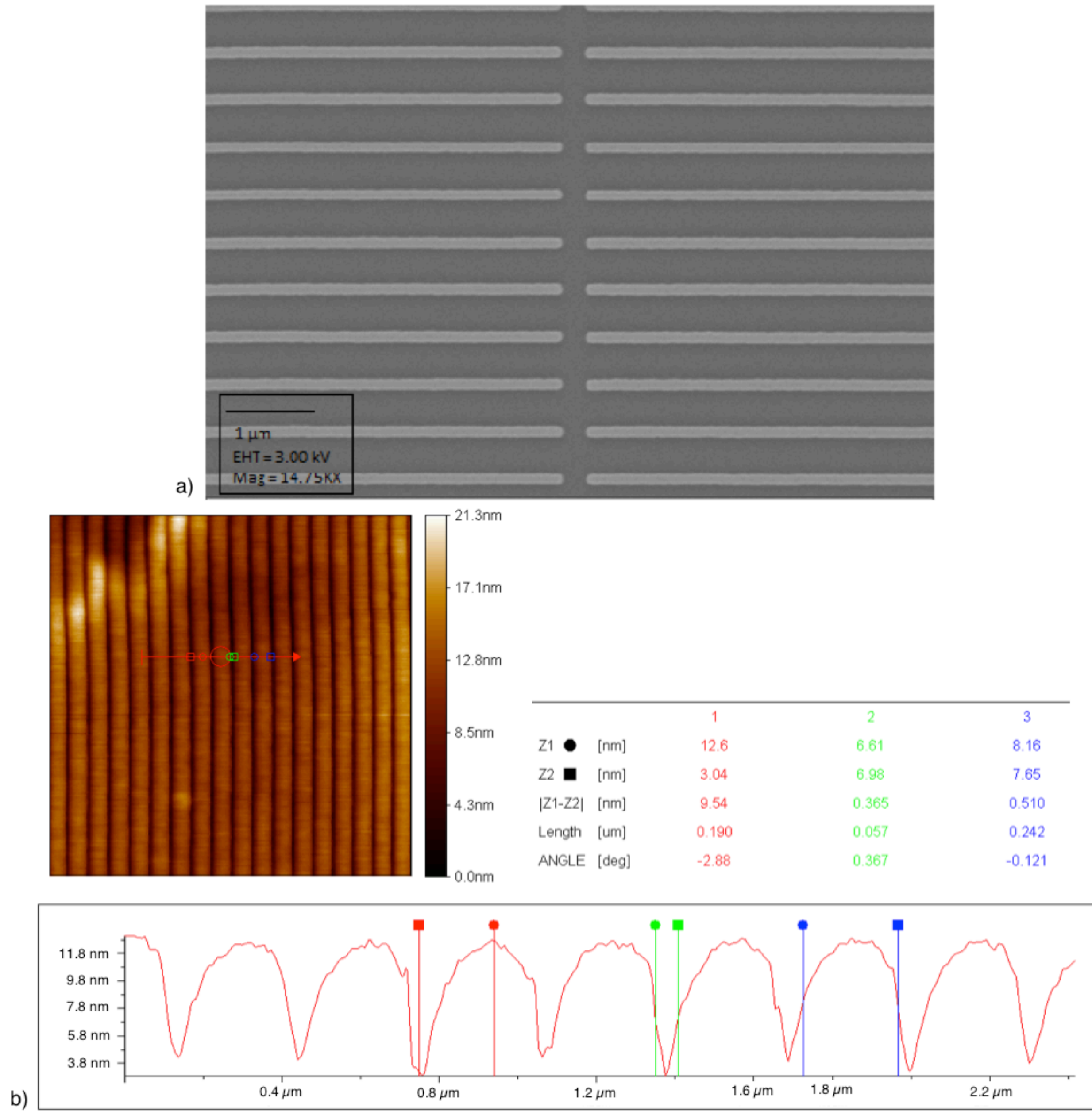

Figure 6.3 a) SEM image showing the line structures in the silicon master mold b) an AFM image of a replica of the 60 nm lines in PDMS.

6.4.1.2 PDMS dilution with solvent

The improvement of mold replication using PDMS diluted with toluene was investigated. The PDMS base was mixed with the curing agent and diluted with different weight concentrations of toluene. The mixture was then poured on a silicon mold and degassed in a desiccator. The mixture was cured at different temperatures and for various times. Different weight concentrations (1:0.1, 1:0.5, 1:1, 1:1.5, 1:2) curing times (1-4 hrs) and temperatures (80° and 100°) were investigated. For the weight concentrations of PDMS to toluene less than 1:2, no structures were visible. The figure 6.4 depicts an AFM image of the nano meter mold replicated in PDMS with a PDMS to toluene concentration of 1:2.

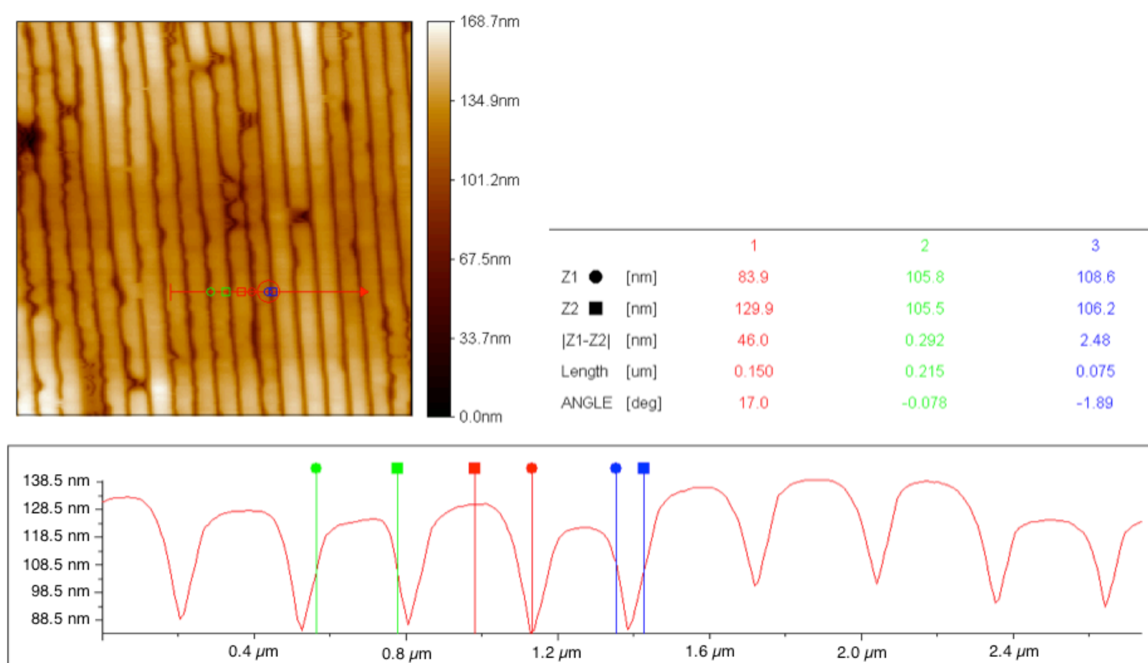

Figure 6.4 An AFM image of a replicated PDMS stamp diluted with Toluene.

The height of this replicated stamp is better as compared to plain PDMS, however, a problem was encountered during this step. The structures were not found to be stable and degraded over time due to the high concentration of the solvent. The degradation of the stamp is shown in the image of figure 6.5. It is taken after four hours of demolding. The degradation in the quality and the height of the structures is clearly visible.

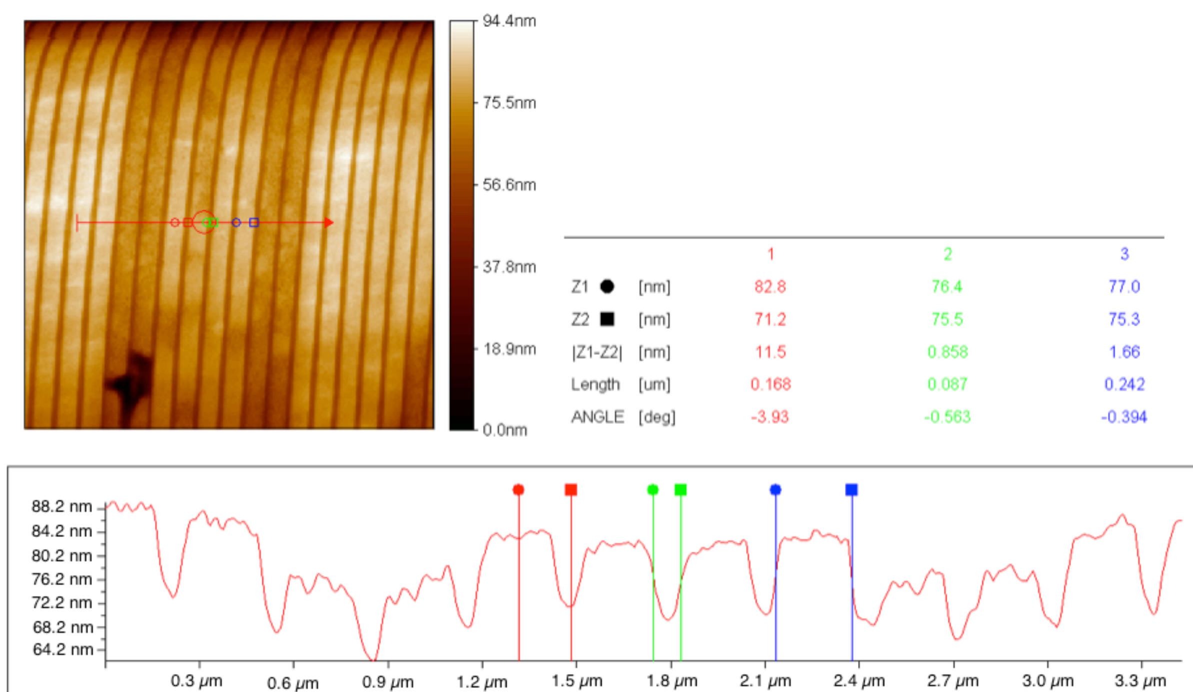

Figure 6.5 AFM image showing degradation of PDMS stamp diluted with toluene four hours after demolding. The height and surface topology both degrade over time due to excessive solvent.

An improvement to the above process was made and the PDMS base was first mixed with 60 wt% toluene and this mixture in turn was mixed in the ratio 10:1 with the curing agent. The amount of curing agent was increased in comparison to the original recipe as the original results were weak and the structures degraded fast. The PDMS diluted with toluene was spin coated on the silicon mold at 3000 rpm and 30 s to get a uniform layer and to fasten the curing time and to improve the evaporation of toluene. The mixture was degassed and cured at 120°C for one hour on a hotplate. This was repeated for different concentrations of toluene. Figure 6.6 shows the AFM images of the PDMS replicas made with varied toluene concentrations.

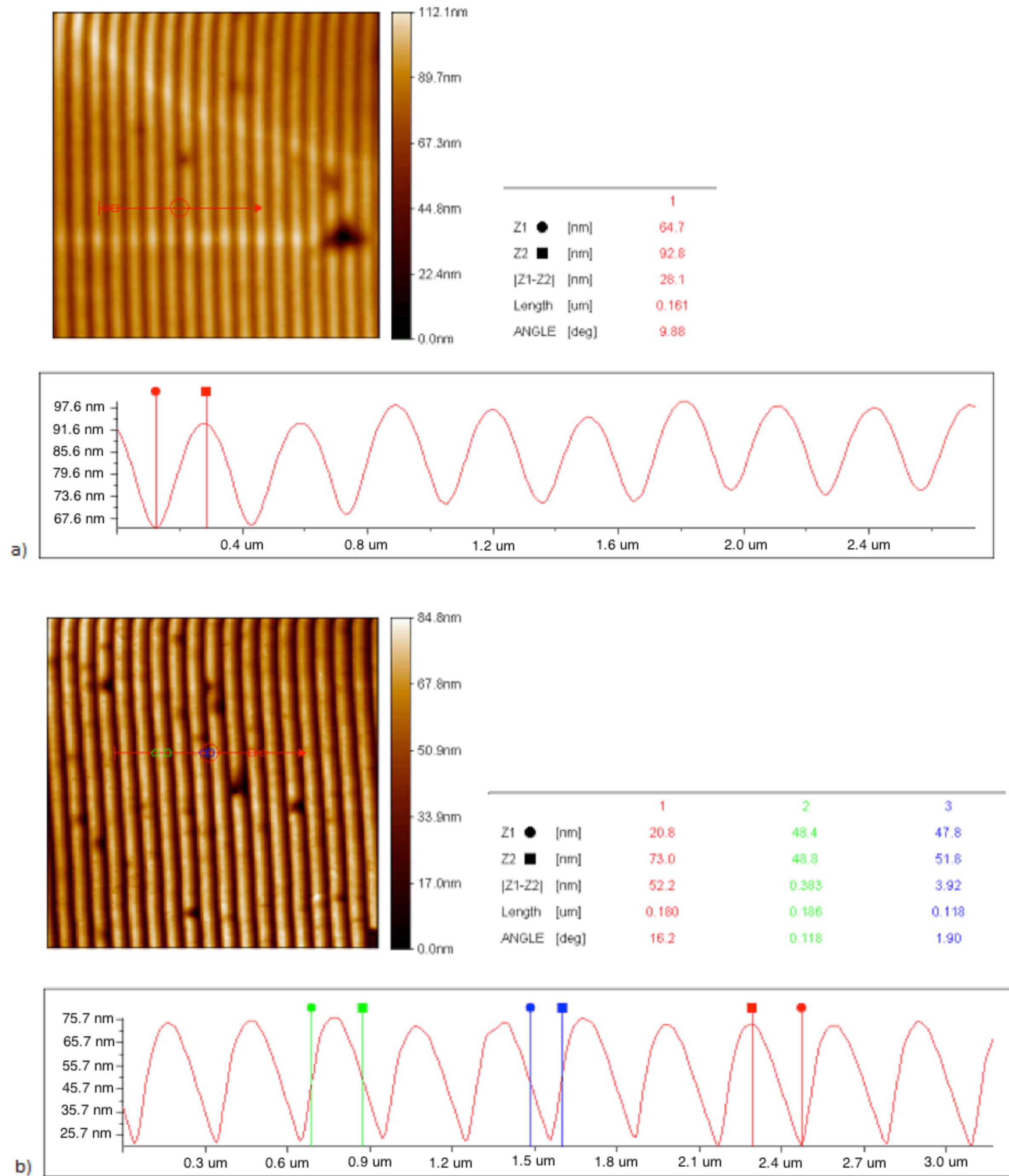
112.1nm
89.7nm
67.3nm
44.8nm
22.4nm
0.0nm
1
Z1 ● [nm] 64.7
Z2 ■ [nm] 92.8
|Z1-Z2| [nm] 28.1
Length [um] 0.161
ANGLE [deg] 9.88
97.6 nm
91.6 nm
85.6 nm
79.6 nm
73.6 nm
67.6 nm
0.4 um
0.8 um
1.2 um
1.6 um
2.0 um
2.4 um
a)
84.8nm
67.8nm
50.9nm
33.9nm
17.0nm
0.0nm
1 2 3
Z1 ● [nm] 20.8 48.4 47.8
Z2 ■ [nm] 73.0 48.8 51.8
|Z1-Z2| [nm] 52.2 0.383 3.92
Length [um] 0.180 0.186 0.118
ANGLE [deg] 16.2 0.118 1.90
75.7 nm
65.7 nm
55.7 nm
45.7 nm
35.7 nm
25.7 nm
0.3 um
0.6 um
0.9 um
1.2 um
1.5 um
1.8 um
2.1 um
2.4 um
2.7 um
3.0 um
b)

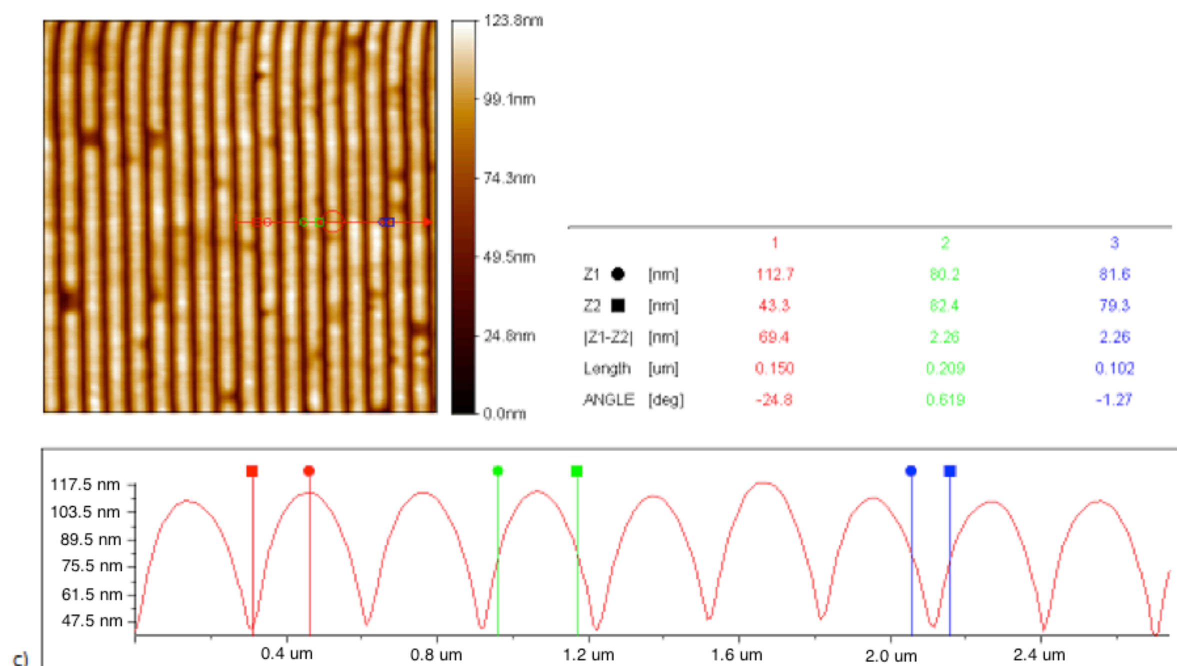

Figure 6.6 AFM images of PDMS mixed with toluene a) 20 wt% b) 60 wt% c) 200 wt%.

As can be seen the best height was obtained with a 200 wt% concentration of toluene. These structures are stable over several days and show just little degradation compared to the stamps made earlier.

6.4.1.3 h-PDMS stamp replication

The process of stamp replication was shifted to using h-PDMS instead of normal PDMS because of the high aspect ratios of our silicon master molds. We already mentioned before, h –PDMS is a hard and brittle material to use therefore stamp replication with this is a slightly complicated process with more components as normal PDMS. The recipe is the same as before except that the prepolymer, Pt catalyst and the modulator are mixed together for two minutes and degassed in a desiccator till the air bubbles are removed. Then 1 g of the hydrosilane prepolymer is gently stirred into this mixture to get as less air bubbles as possible. Degassing at this step is not possible as the polymerization starts almost immediately. A thin layer (30-40 µm) is spin coated (1000 rpm, 40 s) within 3 minutes onto a silicon mold. The h-PDMS is then cured at 80°C for 30 minutes on a hotplate. It does not cure completely and remains slightly tacky. Then normal PDMS is prepared according to the earlier mentioned recipe and poured on the

h-PDMS layer and cured for at least one hour at 80°C. The composite stamp is cooled down and released from the surface very carefully by peeling the stamp. Since h-PDMS cracks very easily, the applied pressure from the tweezers has to be minimum and a bending of the stamp has to be avoided.

The 60 nm line stamp was also used to replicate with h-PDMS. The dimension of the structures was slightly altered after the replication but not by a huge margin. The height again was an issue although the shape of the structures was better as compared to normal PDMS. Figure 6.7 depicts an AFM image of the replicated lines in h-PDMS. Due to the high aspect ratio, some collapsing effect can be seen in the lines.

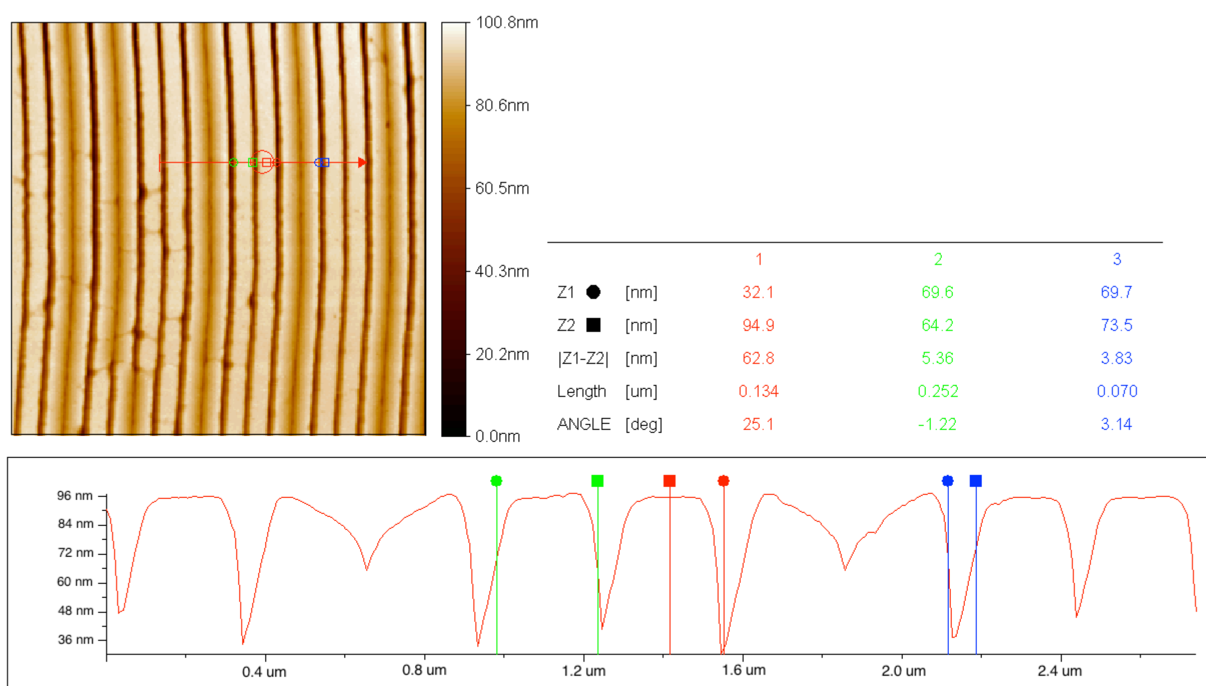

Figure 6.7 AFM image of a replica of 60 nm lines in h-PDMS.

Even after diluting h-PDMS with certain solvents (toluene, triethylamine, hexane), the collapsing or bunching effect could still be seen as shown in figure 6.8 as compared to plain h-PDMS, the structure height after using diluted h-PDMS was much more and resulted in higher bunching together of the lines after demolding. Lower height structures do not bunch together that much as the higher aspect ratio structures.

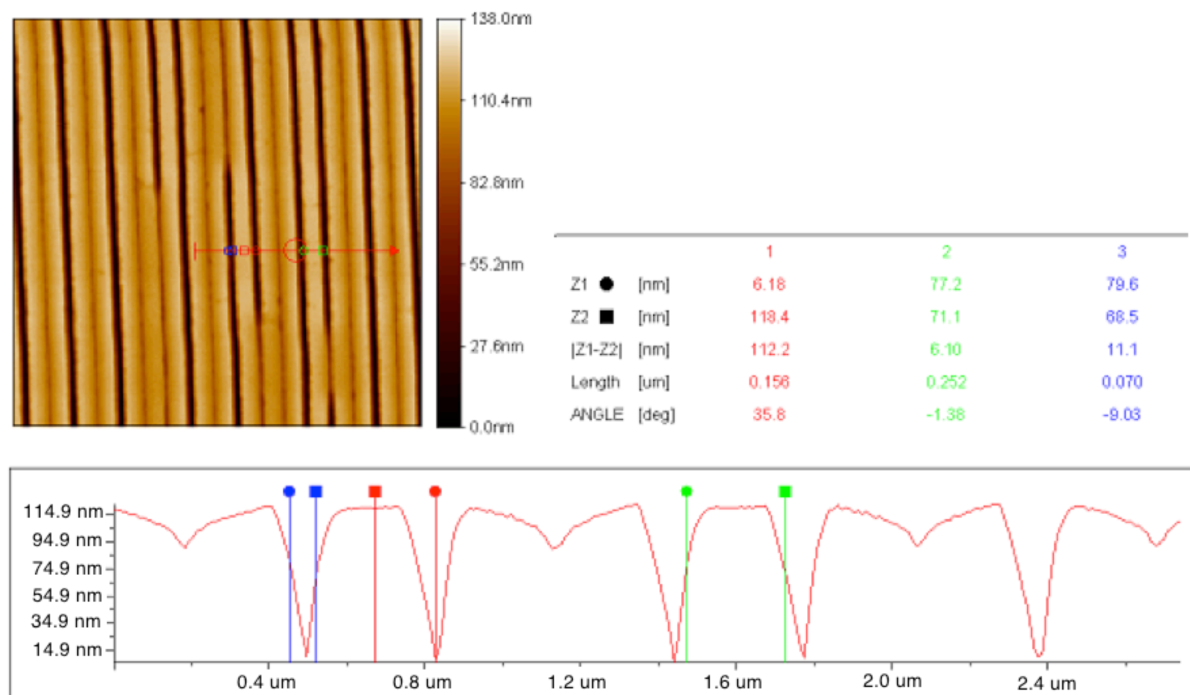

Figure 6.8 AFM image of a stamp replica made in h-PDMS diluted with Triethylamine.

6.4.2 Problems faced during the use of PDMS/h-PDMS

This section briefly goes over the kind of obstacles faced while working with PDMS to replicate the master molds.

6.4.2.1 Swelling of PDMS

PDMS does not dissolve in organic solvents, it swells. The amount of swelling does not only depend on the solvent but also on the temperature. The effect on swollen PDMS stamps on the imprint has been shown by Chen et al. [96]. Lin et al. produced a cleaning procedure for PDMS stamps in order for them to be reused. The cleaning procedure is basically to get rid of impurities, dust particles, organic matter. But the stamps are found to swell up after the cleaning is done and it is necessary to let the solvents evaporate completely before reusing it by leaving it at room temperature or hating it on a hotplate.

6.4.2.2 Plasma treatment

PDMS stamps are highly hydrophobic. Therefore, before making an imprint, the stamps are kept in plasma for a very short time to make the surface more hydrophilic such that

it sticks to the surface of the polymer we are trying to imprint. Unfortunately, keeping it longer in the plasma can cause damage to the PDMS stamp. It can induce cracks in the surface through which uncured PDMS fragments can reach the surface. These fragments can be transferred to the substrate during the imprint and can contaminate it decreasing the quality of the imprint.

6.4.2.3 Shrinkage of the stamps

Lee et al. [97] investigated the shrinkage ratio of PDMS during cooling. They got a shrinkage ratio of 1.06% for curing at 65°C for 4 hours, 1.52% for 80°C for 2 hours and 1.94% for 100°C for 1 hour. The stamps are cured at a lower temperature to avoid shrinkage and the ideal case would be to cure it at 65°C but then that would mean a trade-off between the time to cure and the shrinkage coefficient.

6.4.2.4 Pattern density and aspect ratio

We have already discussed about this in detail in the previous sections. Structures made of PDMS deform easily as the Young's modulus is too low (~2 N/mm^2) whereas structures made of h-PDMS tend to be stiffer due to the higher Young's modulus (~9 N/mm^2). The results of the investigations made by Lee et al. are that an increase in the aspect ratio increases the lateral collapse and the structures with a higher density tend to have more defects. If the aspect ratio is too large, the structures can collapse under their own weight or can adhere to the neighboring structures due to adhesion forces [98].

The critical Young's modulus of the structure is defined as

$$E \equiv \frac{24\sigma H^4}{L^3 d^2}$$

With the surface tension σ of the surrounding liquid, the height of the structures H, the gap between the lines d and the width of the lines L. If the Young's modulus of the molded lines is higher than E, there is no lateral collapse due to adhesion between neighboring structures.

6.4.3 Stamp surface modification

In order to use the stamp for an imprint two surface modifications are done to make it imprint ready- one before making the stamp and one after.

- Antisticking layer – to be able to separate the substrate from the PDMS stamp after the imprint, the resist should only adhere to the substrate and not to the stamp. But the surface energy of the stamp is higher than that of the substrate so the resist inadvertently sticks to the stamp as well. To avoid this, an antiadhesion layer is coated on to the silicon master mold before pouring the PDMS onto it to make a replica. In this work 1H, 1H, 2H, 2H-Perfluorooctyltrichlorosilane (FOTS) from Alfa Aesar is used in the vapor form. It forms a self assembled monolayer of perfluoropolymers on the surface of the silicon mold which ease in the separation of cured PDMS from the mold and avoid damage to the structures.
- Plasma treatment- as already mentioned before, PDMS is highly hydrophobic and in order to guarantee a good surface conformality of the PDMS to the resist being imprinted, it has to be made more hydrophilic. Therefore, the last step in the stamp fabrication is the plasma treatment of the PDMS stamps in order to increase the surface wettability to allow a good conformal contact of the surface of the PDMS with the surface of the resist.

6.5 Results & Discussion

This section details the imprints performed using the above mentioned stamps to pattern the PEDOT:PSS. Two lithographic processes are used to imprint the polymer: standard NIL using hard silicon stamps and soft lithography using the PDMS stamps prepared in the above sections.

6.5.1 Direct imprints with silicon stamps

Direct imprints using the standard silicon stamps (line structures with dimensions of 60 nm and pitch 250 nm) were performed in our nanoimprinter. Three different substrates were used: silicon, glass and quartz.

6.5.1.1 Imprints on silicon

Before imprinting on glass substrates which is the ultimate goal, some test imprints were performed on silicon wafers coated with PEDOT:PSS as the surface of the silicon wafers is very flat and smooth which is favorable for spin coating a homogenous layer of PEDOT:PSS. The silicon wafers were cleaned with the standard RCA clean method by keeping it in acetone and IPA for 10 minutes in an ultrasonic bath in order to get rid of

the impurities. PEDOT:PSS solution is spin coated onto the silicon wafers at a speed of 1000-3000 rpm for a time between 30-60 seconds. The layer thickness obtained ranged from 130 nm to 80 nm which is suited for our imprints as the structure height of our stamps was about 90nm. The imprints were performed in our nanoimprinter at a temperature of 165°C, a pressure of 50 Bar for a time of 420 seconds. Various imprints were performed with different parameters but the best result was obtained for the above mentioned recipe. Figure 6.9 shows an AFM image of the obtained imprint into PEDOT:PSS. The structures have a height of ~ 130 nm.

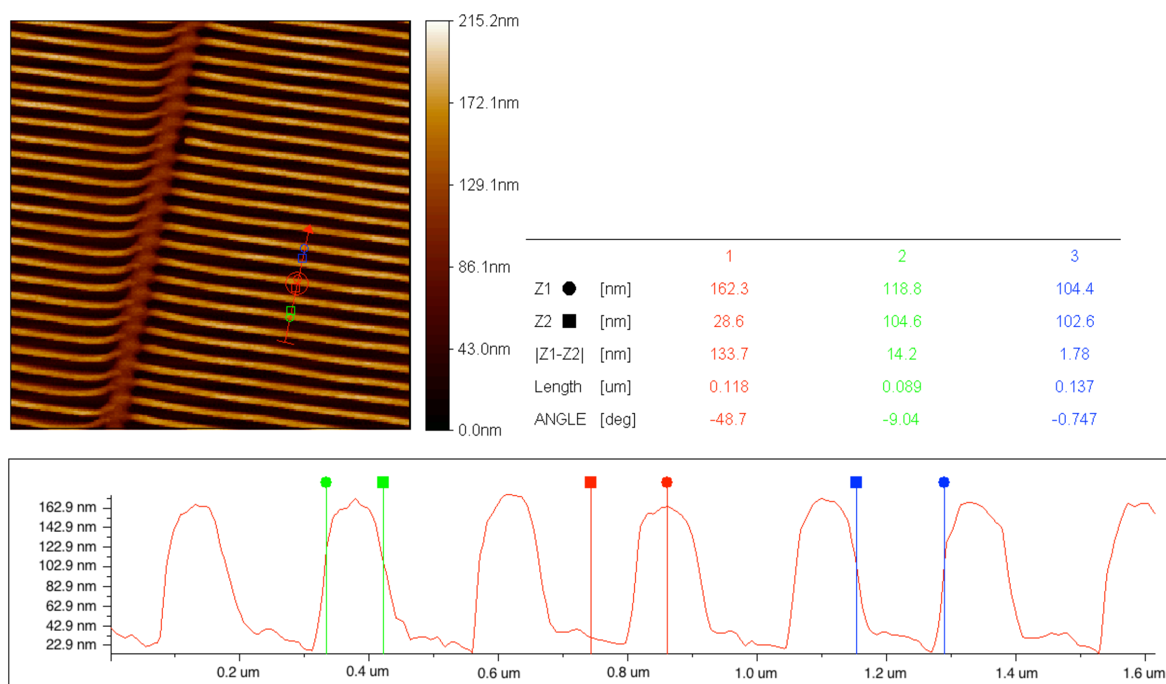

Figure 6.9 AFM image of a direct imprint into silicon with a hard stamp.

6.5.1.2 Imprints on glass

The same imprints were performed on microscopic glass slides mentioned in section 6.3 with the same silicon stamps but unfortunately a very small area was imprinted. The glass slides were cleaned with the standard RCA clean recipe and also put in oxygen plasma for better adhesion of the polymer to the glass. The recipe was changed to higher pressure and time but even then we observed only the edges of the structured area were imprinted. This can be attributed to the poor homogeneity of the spin coated PEDOT:PSS layer onto the glass slides as the surface of the glass substrates is very rough as compared to silicon. This leads to poor overall contact of the stamp surface with the PEDOT:PSS layer leading only to imprints in the area there is a good contact.

6.5.1.3 Imprints on quartz substrates

The reason for using quartz substrates was its highly polished and smooth surface such that the spin coated layer of PEDOT:PSS is homogenous all over the surface and there is a higher contact between the stamp and polymer surfaces. The same cleaning recipe and plasma treatment was applied to the quartz substrates as well before spin coating the polymer. The imprints turned out to be much better than earlier as shown in the AFM image in figure 6.10.

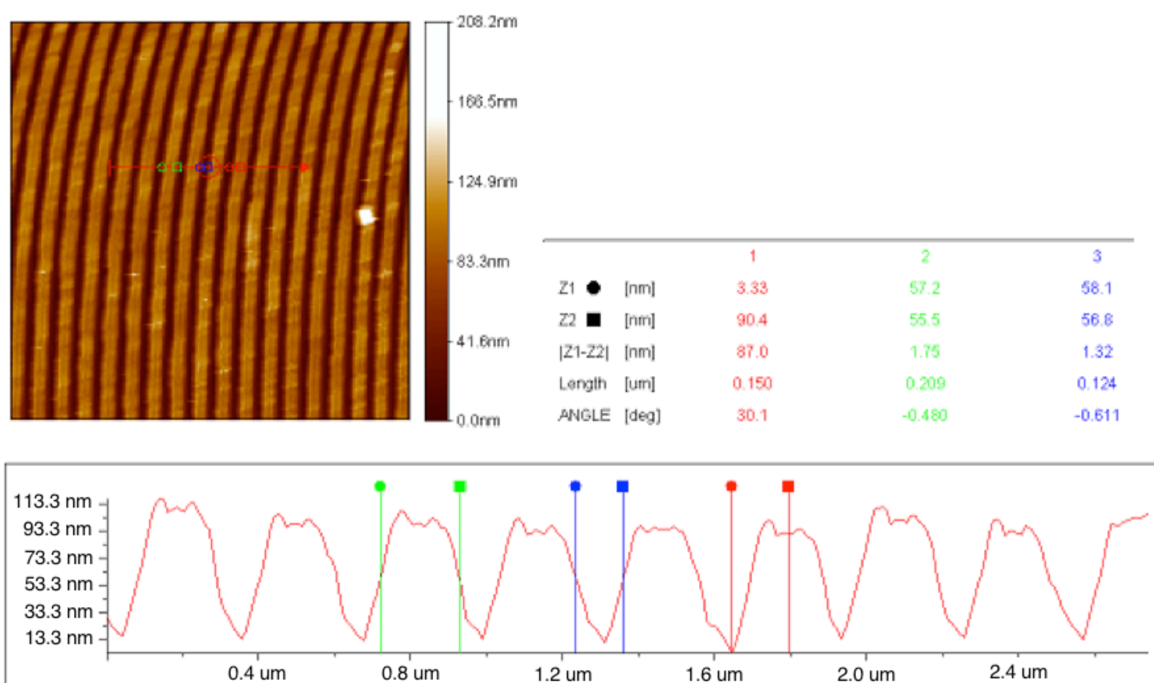

Figure 6.10 AFM image of an imprint on a quartz substrate using the silicon stamps.

Till now PEDOT:PSS 4083 was being used for the imprints. In order to test other versions as well, PEDOT:PSS 8000 was spin coated and imprinted upon using NIL and a noticeable difference was observed in the extent of the imprinted area. Imprints on PEDOT:PSS 8000 lead to a larger area of imprint. This is due to the fact that the grain size of PEDOT:PSS 4083 (80 nm) is much larger as compared to PEDOT:PSS 8000 (30 nm). Therefore, the particles of PEDOT:PSS 8000 are quite small as compared to the spacing in the stamp which is 250 nm and so the imprint is easier leading to a larger

area being imprinted. Figure 6.11 shows two microscopic images of the imprinted areas using the two different versions of PEDOT:PSS.

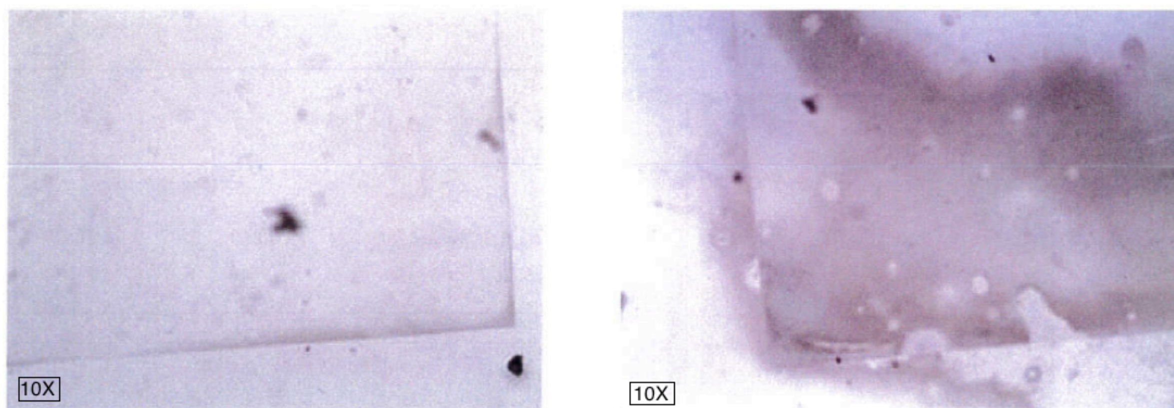

Figure 6.11 Microscopic images showing the imprinted area in PEDOT:PSS 4083 (left) and PEDOT:PSS 8000 (right).

6.5.1.4 Imprinting on G-PEDOT:PSS on glass/quartz substrates

Glycerol doped PEDOT:PSS with a concentration of 3% weight was spin coated at a speed of 1500 rpm for 60 sec on glass and quartz wafers and imprinted with the obducat imprinter. The figure 6.12 shows an AFM image of the imprinted sample where it is clearly observable that the lines are ripped off. The G-PEDOT:PSS is too soft and the glycerol was not completely evaporated during the imprint. The polymer film is still greasy after the imprint. The imprint looks the same even if different recipes were used by varying the temperature, pressure and times.

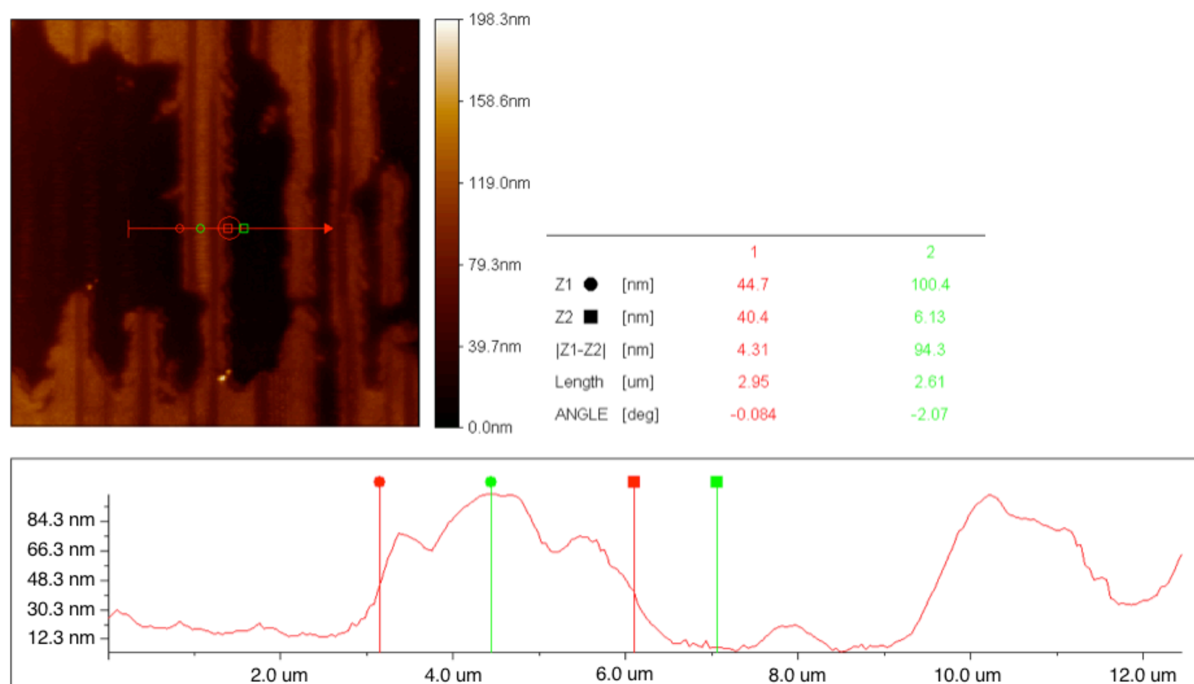

Figure 6.12 AFM image of an imprint on G-PEDOT:PSS on a glass substrate. It can be clearly seen where the lines have ripped off and got stuck to the stamp since the polymer film was very greasy due to the glycerol.

6.5.2 Improved NIL process on quartz substrates

The imprints described above show unsatisfactory results so far therefore, the imprint process was changed. During the classic imprint process, the polymer is heated first to a temperature above its glass transition temperature in order to make it less viscous such that it flows into the structures and then the pressure is applied to press the stamp structures into the polymer. This technique does not work that well with PEDOT:PSS as it does not have a glass transition temperature unlike other polymers. The mechanical properties depend strongly on the relative humidity. The Young's modulus for example, drops by approximately two thirds when the relative humidity is increased from 25% rH to 55% rH [99]. PEDOT:PSS is a water based dispersion and the grains have more degrees of freedom and can respond to a external force by slipping past each other.

As already described in the earlier section, PEDOT:PSS films consist of grains with a diameter of about 30-50 nm and the diameter decreases when the film dries. Under

pressure, the shape of the grains changes to a slight lentil shape [99]. The coherence of the material is due to hydrogen bonds which are stronger if the humidity is lower, so the material cracks through the individual grains and the fracture is brittle. If the humidity is higher, the hydrophilic and hygroscopic PSS rich shell swells and distance between the individual grains becomes larger. The grain shape is rounder than in the dried films. The hydrogen bonds are weaker and so the cohesion and therefore the mechanical strength are reduced. The individual grains can slide along each other and plastic fracture behavior occurs.

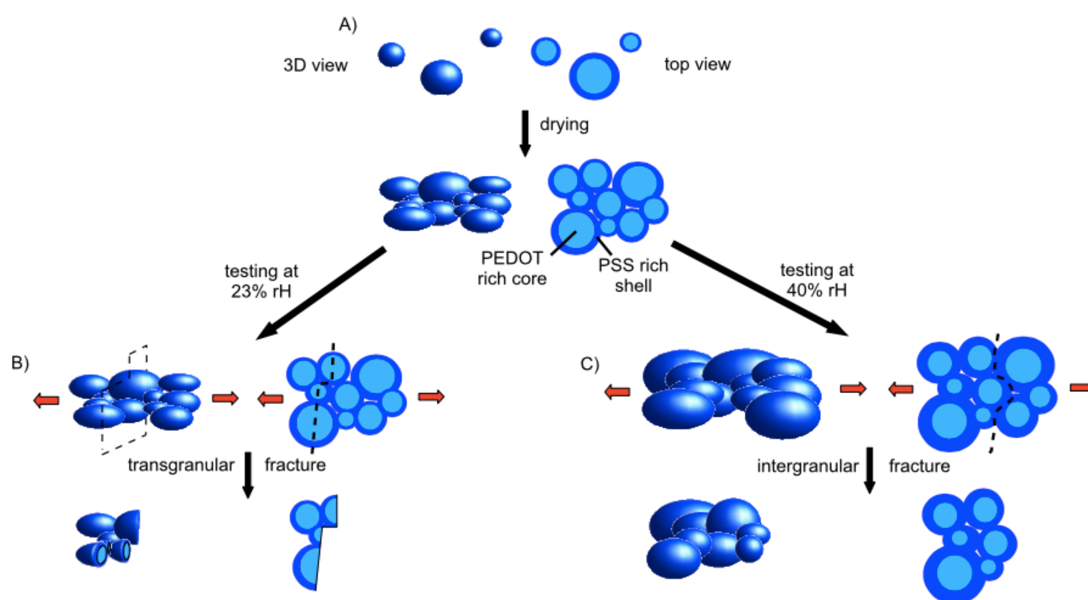

Figure 6.13 Schematic of the grains and fracture process in PEDOT:PSS with different humidity concentrations [99]

These results from Lang et al. and Friedel [100] were taken into account for the development of the new imprint process. If the PEDOT:PSS film is heated first, the film becomes hard and the hydrogen bond between the individual grains are stronger so a high pressure is needed to imprint the material. If the stamp structures are bigger, the grains can rearrange easier and the structures are imprinted. If the pitch of the lines becomes smaller (250 nm), a higher pressure is needed to imprint which makes it impossible to imprint the complete area of the stamp.

In the new imprint process, a PEDOT:PSS film was spin coated twice on a plasma treated (200W, 2 minutes) quartz substrate with 1500 rpm for 60 seconds. The imprint process consists of two steps- in the first step, the stamp was pressed into the substrate with a lower pressure of 40 Bar at 55°C and the pressure was kept for 120 seconds. In

the second step, the temperature is raised to 100-120°C and the pressure is kept constant at 40 Bar for 120 seconds again. The imprint stack is then cooled down to 90°C and the pressure released before demolding the stamp from the substrate. Figure 6.14 shows the traditional imprint process and the improved one.

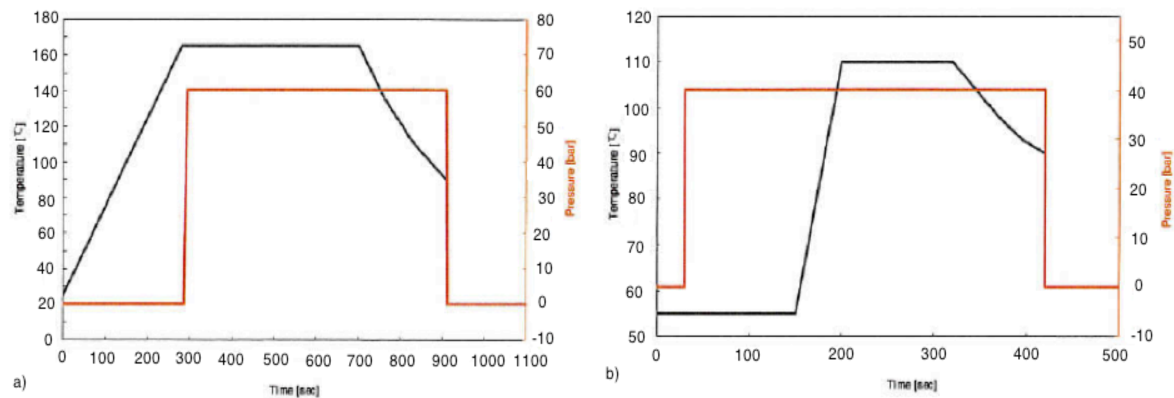

Figure 6.14 Recipe flow of a) traditional NIL process b) improved NIL process.

Figure 6.15 shows AFM images of the imprints done using the improved method. The height of the structures is about 45- 50 nm.

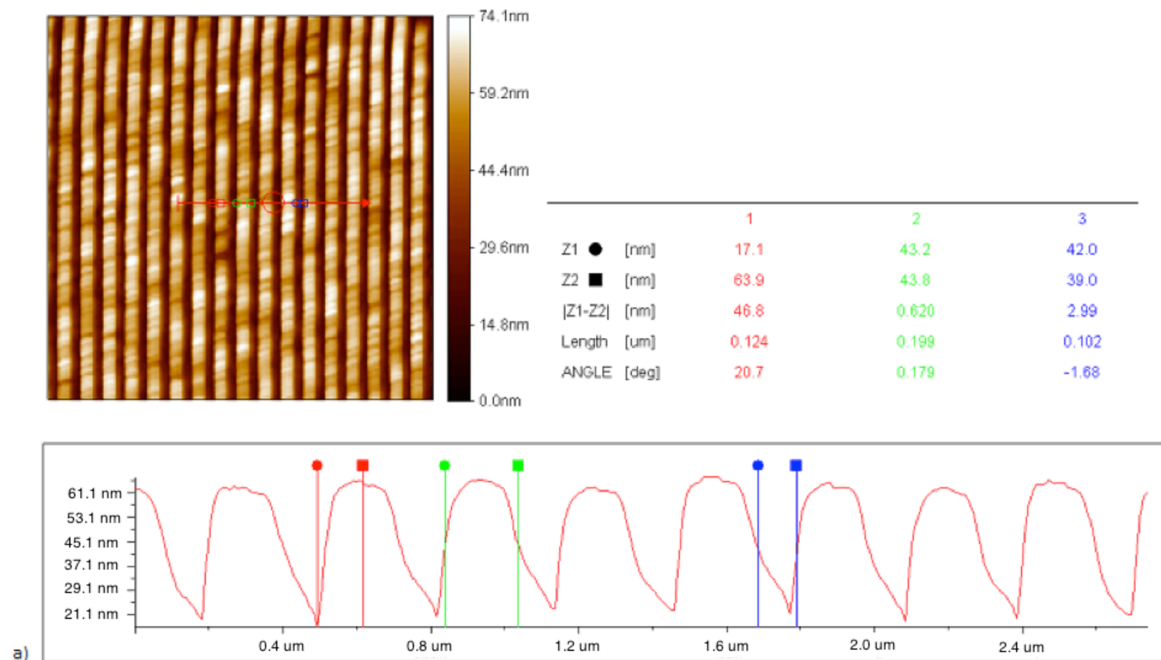

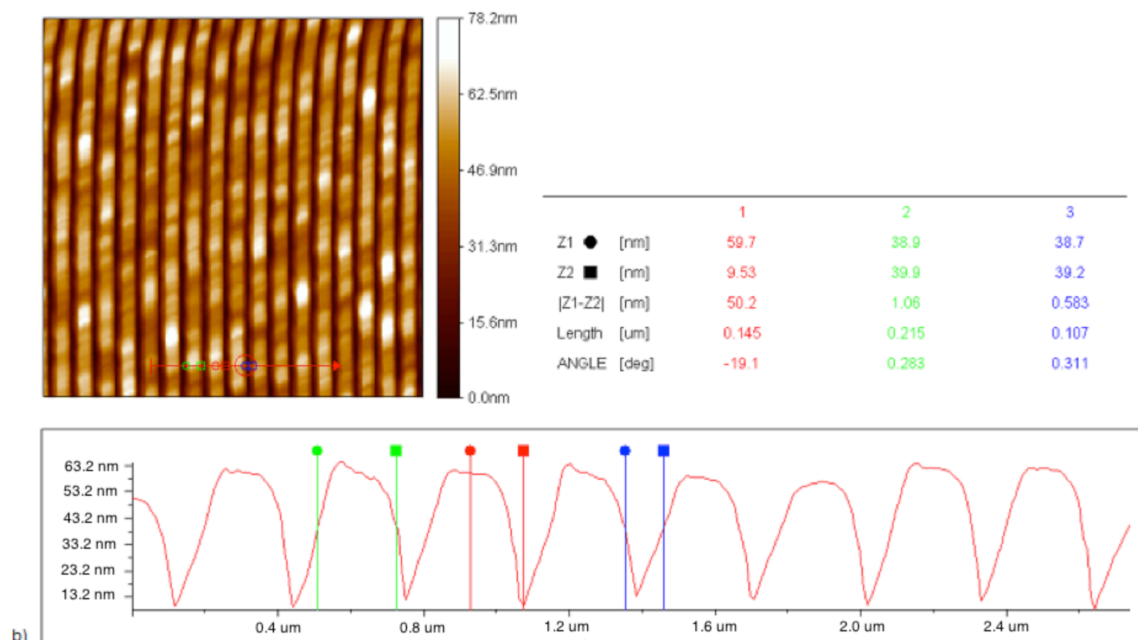

Figure 6.15 AFM images depicting the imprints on PEDOT:PSS films on a quartz substrate using the improved imprinting method.

6.5.3 Soft lithography

A new method to imprint polymers called plasticizer assisted imprint lithography (PAIL) was developed by Tan et al. [101, 102]. Most polymers used in NIL are thermoplasts as non-thermoplastic polymers are difficult to imprint as their mechanical properties are almost constant over a wide range of temperatures (20-200°C). Degradation occurs at 300°C. PEDOT does not have a distinct glass transition temperature T_g as normal imprint polymers and therefore PEDOT has no state when the viscosity is low enough to be imprinted. The addition of a plasticizer improves the imprintability of this polymer and increases the chain mobility of the polymers, lowering the viscosity thereby making the imprint possible at low temperature and pressure.

The glycerol doped PEDOT:PSS is softer as normal PEDOT:PSS and the viscosity can be changed by the amount of added glycerol. The mechanical stability of the imprinted structures may be reduced by the plasticizer residue between the polymer matrixes. Spin coated G-PEDOT:PSS films becomes softer and it remains soft over some hours.

The PEDOT:PSS dispersion is doped with glycerol in different concentrations and the solution is spin coated on a plasma cleaned glass substrate (1500rpm for 60 sec). The

glycerol does not evaporate during the spin coating but it stays in the film for several hours due to the low vapor pressure of glycerol (<0.1 kPa at 20°C).

The substrate is placed on a cool hotplate and a plasma cleaned PDMS stamp is placed upside down on top of it and loaded with a weight of ~ 900g. The substrate is heated in steps of 10°C every 5 minutes from room temperature to 80°C and left on the 80°C hotplate for three hours. The PDMS is gas permeable, this prevents the trapping of gas pockets at the mold-polymer interface. Glycerol and water also pass through PDMS mold and evaporate. The restructured polymer film hardens during the evaporation with a topographic pattern complementary to that of the PDMS mold. The time of three hours is needed for the glycerol to evaporate. If a shorter time is used, the glycerol remains still in the film and the structures are not completely imprinted. The PDMS stamp is water permeable and the water and glycerol can evaporate through it. After three hours, the substrate is removed from the hotplate and the weight is removed. The sample with the stamp on top is cooled down. After the complete cooling, the stamp is removed carefully without damaging the structures. The sample shows a negative imprint of the stamp. The hotplate is heated to 140°C and the sample is placed on it for 10 minutes. This annealing ensures that the remaining glycerol evaporates completely of the film. The structures appear also better after this annealing step. This imprint process is shown below in figure 6.16.

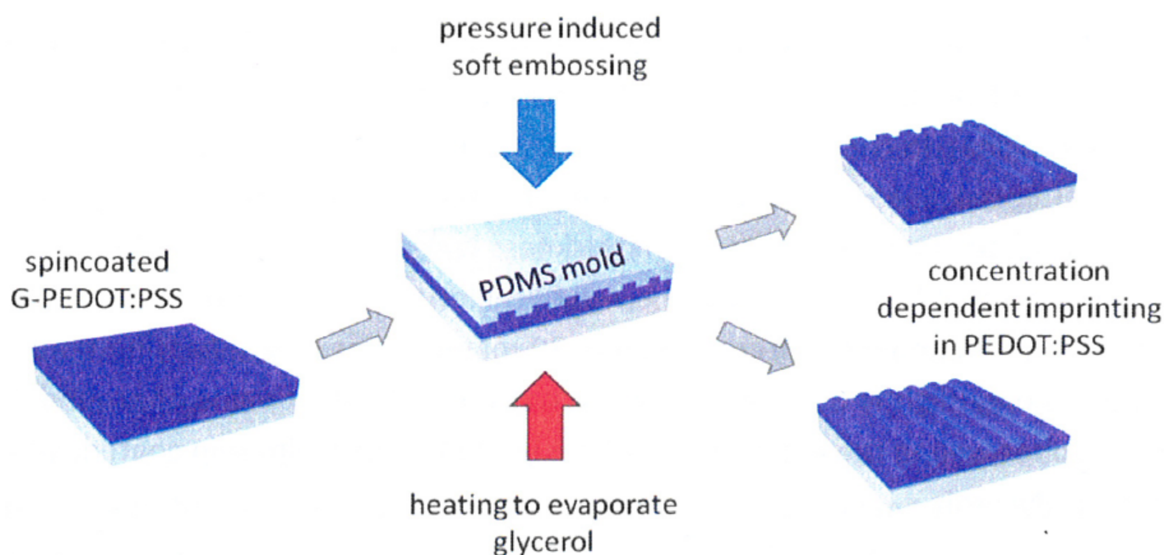

Figure 6.16 Process flow of the plasticizer assisted imprint lithography [103].

Figure 6.17 shows the evolution of the relative film thickness of spin coated G-PEDOT:PSS on a hotplate and at room temperature.

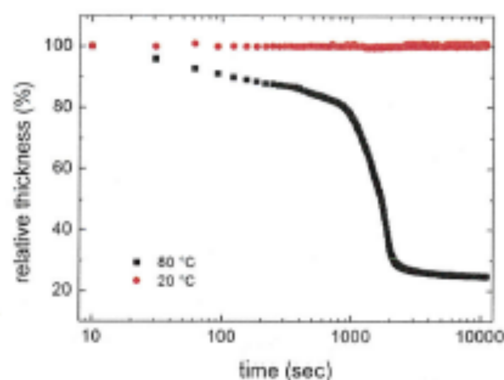

Figure 6.17 Evolution of the relative film thickness of spin coated G-PEDOT:PSS heated on a hotplate (black) and at room temperature (red) [103]

6.5.3.1 Soft lithography using DVD stamp

The PDMS stamp prepared from the DVD structures was used first for the imprints in G-PEDOT:PSS and figure 6.18 shows an AFM image of the imprint.

6.5.3.2 Soft lithography with nanometer structures in PDMS

Since the micrometer structures were imprintable, the process was shifted to the nanometer region. Figure 6.19 shows the imprint with a PDMS stamp (PDMS diluted with toluene). As can be seen from the AFM image, a small percentage of residual PDMS lines was left behind on the substrate where it got ripped off from the PDMS stamp upon demolding. This was only observed on stamps made with diluted toluene since the PDMS is not very stable after curing as the toluene concentration is too high. The height of the lines was observed to be ~ 40 nm.

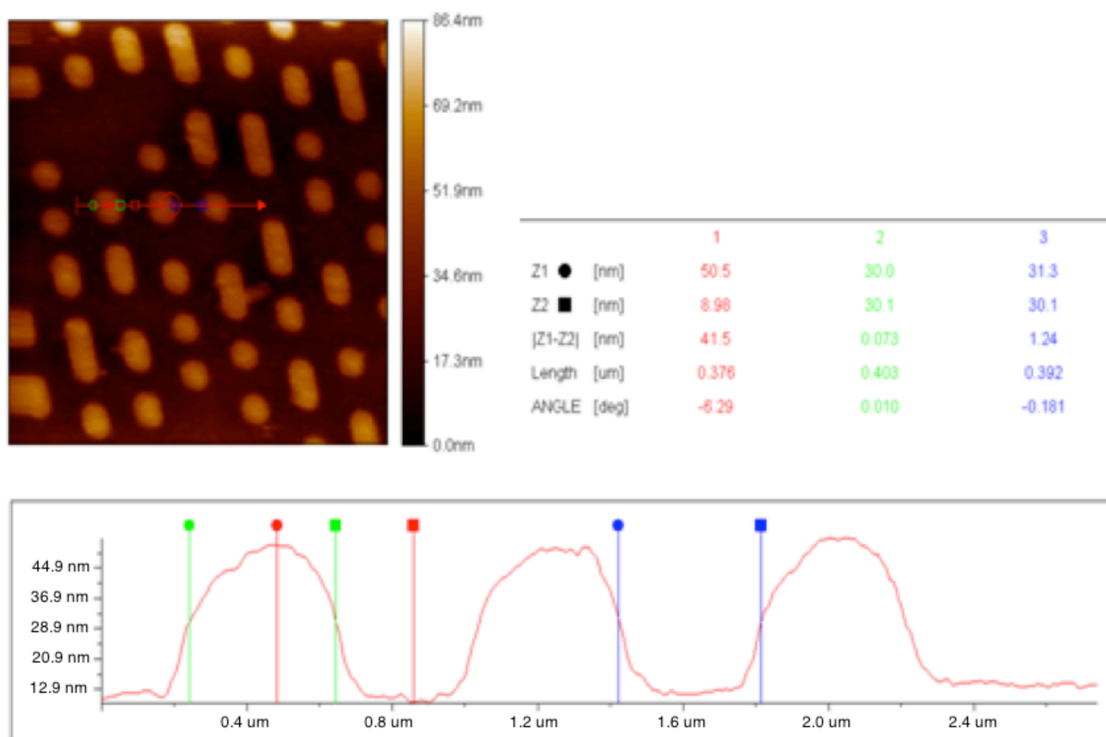

Figure 6.18 AFM image showing an imprint into G-PEDOT:PSS using a DVD stamp made in PDMS.

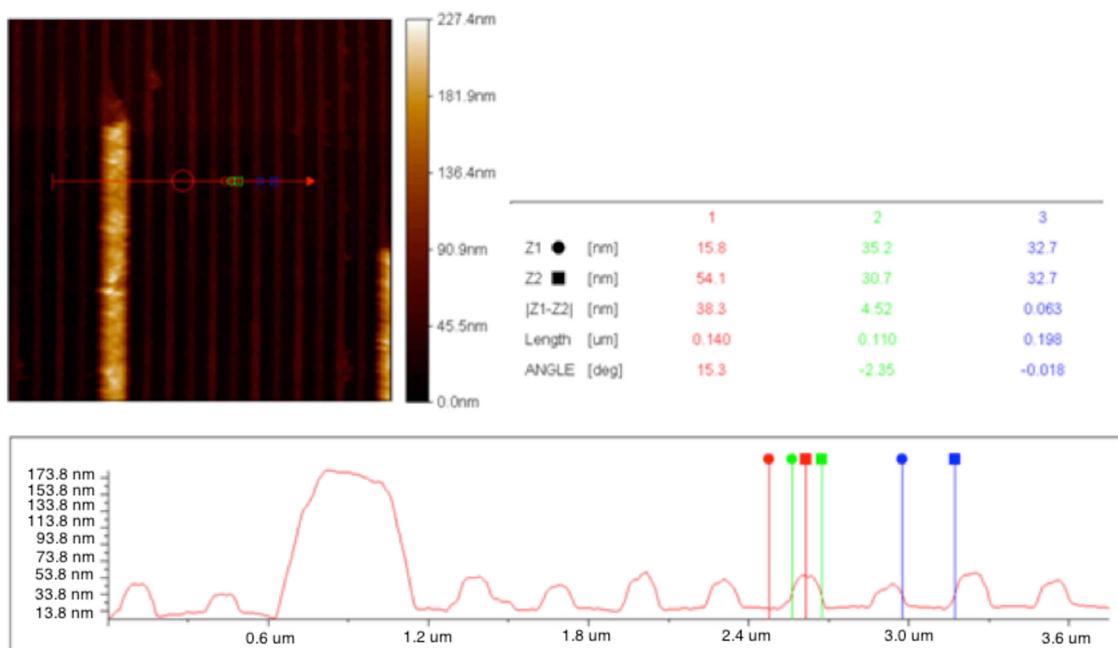

Figure 6.19 AFM image of an imprint into G-PEDOT:PSS using the PDMS stamp with nanometer structures.

6.5.3.3 Soft lithography with h-PDMS stamps

The next imprints were done with a h-PDMS stamp. The lines of the h-PDMS stamp merged or collapsed onto each other as mentioned in section 6.4.1.3. Therefore, upon imprinting some of the lines are ripped off which is visible in the surface profile in the AFM image of figure 6.20. The shape and height of the remaining lines is good.

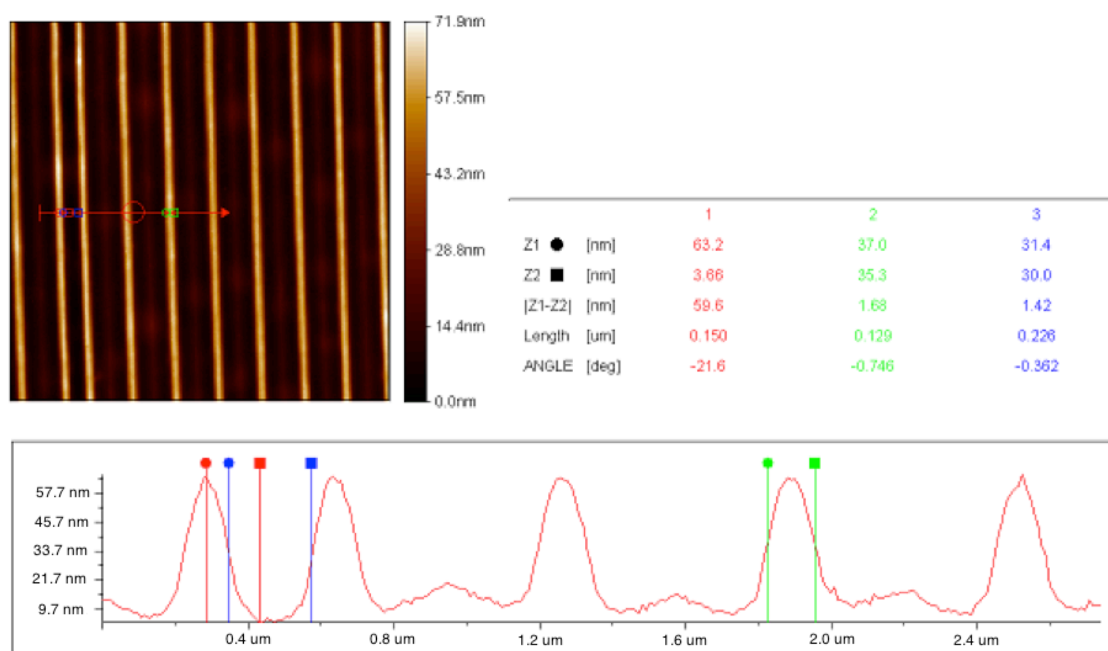

Figure 6.20 AFM image of an imprint on G-PEDOT:PSS using a nanometer resolution h-PDMS stamp.

6.5.3.4 Soft lithography on thermal imprint polymer

The soft lithography technique was also applied to thermal imprint resist mr-I 8000R to be able to compare the result with those of G-PEDOT:PSS. The imprinting time for this polymer is lower than for G-PEDOT:PSS as no glycerol has to evaporate and the solvent in the polymer evaporates faster.

The polymer mr-I 8010R or mr_I 8020R, depending on the height of the structures was spin coated at 3000 rpm for 30 seconds on a cleaned glass substrate. The sample was placed for 1 minute on a hotplate at 100°C to prebake it to evaporate residual solvent. The sample was then placed on a cold hotplate, the PDMS stamp was placed on top it and a weight of 900g was placed on it. The imprint was heated from 30°C to 160°C in

steps every 5 minutes and the temperature was held for one hour to ensure all the solvent has evaporated. When the imprint was done, the sample was cooled down and the PDMS stamp is removed. The results are shown in figure 6.21. This result is comparable with the result of the G-PEDOT:PSS imprinted sample, so the plasticizer assisted imprint with G-PEDOT:PSS shows good results. This can be used as a low cost process to pattern large areas or even curved surfaces.

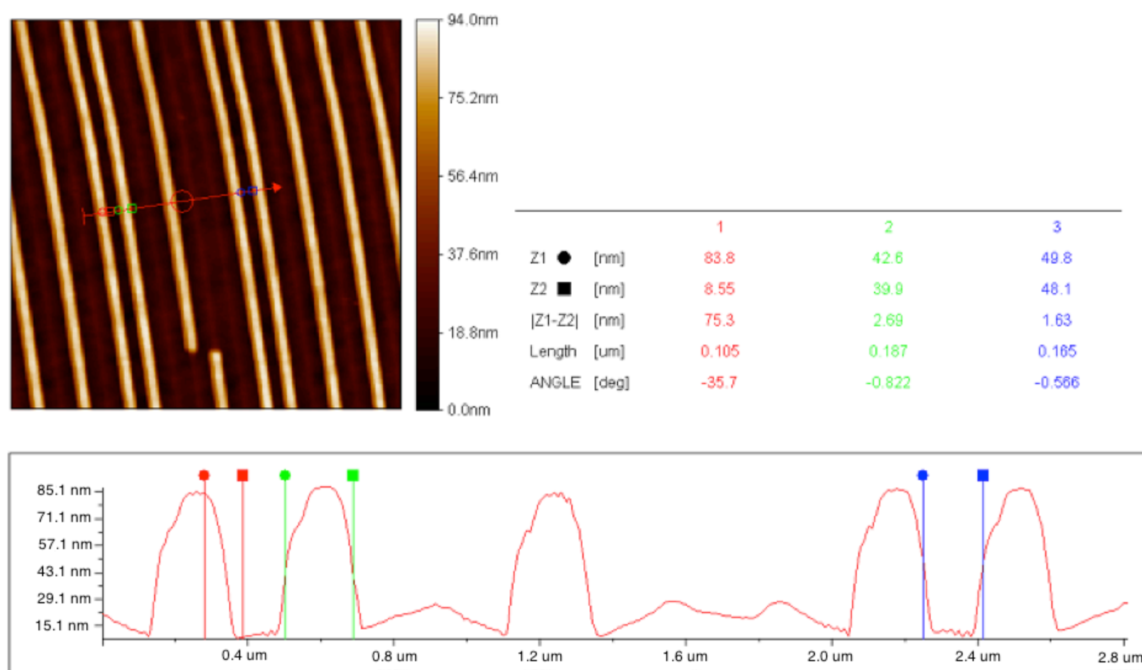

Figure 6.21 AFM image of an imprint on thermal polymer mr-I 8010R with a h-PDMS stamp.

6.6 Characterization

6.6.1 Sheet resistance measurements

To measure the surface resistivity of the material, the four-point probe method was used. Four probes are aligned linearly and contact the surface of the material with an equal space S between them. The thickness of the sample is t. The resistance is the ratio of voltage to current. A current is flowing between the outer two probes and the voltage between the inner two probes is measured. The resistance is the product of the sample resistivity and a geometrical factor.

$$R = \frac{V}{I} = \frac{\rho}{t} g$$

With the geometrical factor g

$$g = \frac{1}{\pi} \ln \left(\frac{sinh\,(t/S)}{sinh\,(t/2S)} \right)$$

The geometric factor depends on the ratio t/S. The resistance for thick wafers t/S>>1 is

$$R = \frac{\rho}{2\pi S}$$

And for thin wafer t/S <<1,

$$R = \frac{\ln\,(2)}{\pi} \frac{\rho}{t}$$

The resistance is calculated for a particular layer thickness. If it is used without a particular thickness, it is called sheet resistance.

$$R_s = \frac{\rho}{t}$$

Figure 6.22 depicts what a four-point measurement set-up looks like followed by the measured sheet resistance of PEDOT:PSS and G-PEDOT:PSS films. The resistance of G-PEDOT:PSS is lower than that of a plain PEDOT:PSS film. This means the conductivity is enhanced in G-PEDOT:PSS films as the conductivity is given by

$$\sigma = \frac{1}{\rho}$$

The measurements were done with a Keithley semiconductor four-point measurement set-up.

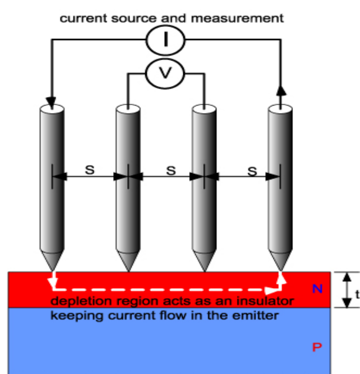

Figure 6.22 Four-point measurement set-up for measuring the sheet resistance.

Figure 6.23 Sheet resistance graphs of the three different versions of PEDOT:PSS and G-PEDOT:PSS.

6.6.2 Transmission measurements

The following measurements were measured with a monochromator (Newport optical instruments) and a silicon detector from Oriel. An aperture with a diameter of 3 mm was used for the light to pass through the sample. The distance between the sample and the detector was 40 mm. As a reference, a glass slide with a plain film of PEDOT:PSS or G-PEDOT:PSS was used.

Figure 6.24 shows the transmission of a plain film of PEDOT:PSS and G-PEDOT:PSS. The transmission is lower in the higher regions of the wavelength and the samples with G-PEDOT:PSS show an overall higher transmission.

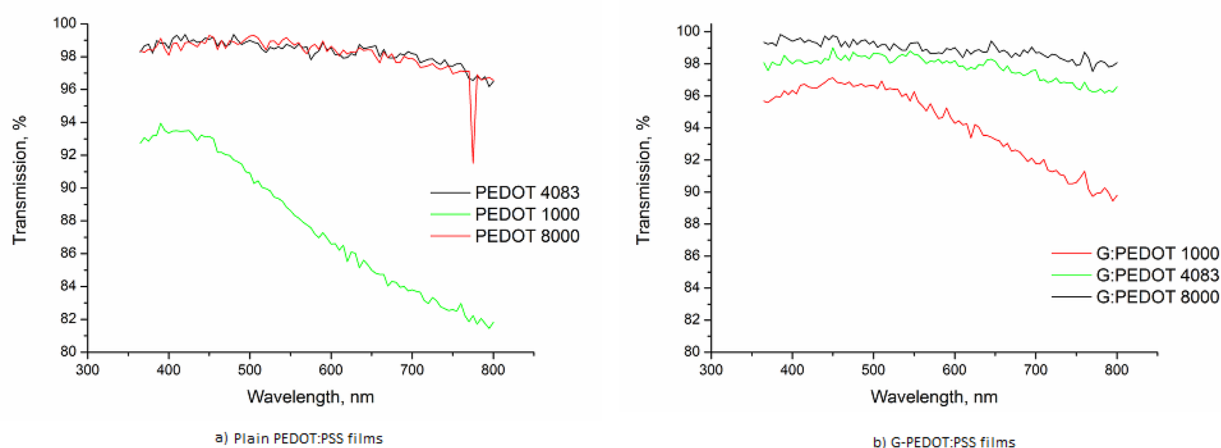

Figure 6.24 Transmission curves for plain PEDOT:PSS films as well as glycerol doped films.

The effect of gratings and waveguides should be analyzed properly to better understand the transmission phenomena in conjugated polymers as it not proven till now if plasmonic effects occur in conjugated polymers.

6.7 Summary

The research presented here shows the possibility of patterning plain PEDOT:PSS and glycerol doped polymer films with a simple nanoimprinting techniques and tools. The results presented produce high structures in PEDOT:PSS in the sub 100 nm region using easy lithographic techniques which has not been presented in other publications.

6 NIL FOR ORGANIC OPTOELECTRONIC DEVICES

The fabrication of PDMS stamps has been explained in detail from the micrometer to the nanometer range. The effects of diluting the PDMS prepolymer with solvents have also been analyzed in order to better replicate the nanometer structures. The resolution of the structures is limited by the material used but can be improved by altering the material from PDMS to Ormostamp (micro resist technology GmbH) or poly(urethane acrylate).

Using the standard obducat nanoimprinter tool, various imprints have been performed on different substrates as explained. A new improved imprint process has also been developed adapting to the material properties of PEDOT:PSS which can be performed using a standard nanoimprinter tool and is therefore much less complicated. Other lithographic techniques such as soft lithography have also been shown to work on patterning PEDOT:PSS layer doped with glycerol.

Some resistivity and transmission measurements were also done but more detailed research and simulations need to be performed in this area to have a better understanding of the effects of the grating structures on the PEDOT:PSS films.

Chapter 7

NIL for Metasurfaces

Till now we have seen how NIL has been used for fabricating structures for varied applications ranging from nanomagnets to nanowires to optoelectronic devices etc. In this last chapter of this thesis, we focus on yet another application of NIL: metasurfaces. What exactly is a metamaterial will now be explained. Almost all electromagnetic phenomena and devices result from interactions between waves and materials [104]. This means that in order to realize this phenomenon, the waves have to be manipulated in accordance with the geometries and structures of the available materials. However, this limits the diversity of electromagnetic devices purely based on the scope of the available materials used to build them. Therefore the term metamaterial was coined by Smith et al. in 2000 on negative permittivity and permeability at microwave frequencies [ref from book]. A metamaterial is defined as "an artificially structures material which attains its properties from the unit structure rather than the constituent materials. A metamaterial has an inhomogenity scale that is much smaller than the wavelength of interest and its electromagnetic response is expressed in terms of homogenized material parameters" [104]. The prefix 'meta' means 'beyond' thereby signifying systems that are beyond conventional materials.

The history of metamaterials dates back centuries ago when artists used metamaterials without fully understanding the physics behind it all. One such famous example is the Lycurgus cup: a Roman glass challis dating back to fourth century AD. It is made with

ruby glass embedded with gold nanoparticles making it appear green when viewed reflected light such as daylight and reddish with light transmitted through the glass as depicted in figure 7.1[105].

Figure 7.1 Lycurgus cup which appears green in reflected light and red in transmitted light [105].

We will now discuss how metamaterials are related to NIL and this chapter in general.

7.1 Introduction

The idea of metamaterials has been adopted in the optics community as well. Among all branches of metamaterials research, those materials exhibiting tailored electromagnetic responses at light frequencies known as optical metamaterials are by far the most fascinating and challenging topic. Light is the ultimate means of sending information to and from the interior structure of materials- it packages data in a signal of zero mass and unmatched speed. The electromagnetic properties of a material are determined by two material parameters: the permittivity ε and permeability μ, describing the coupling of a material to the electric and magnetic field components of an electromagnetic wave respectively [104].

We are aiming to combine the metamaterials or metasurfaces facet with optics to generate nanostructures which can be used for light bending applications. Optical

metasurfaces manipulate direction and \or polarization of light using an array of nano-structures or nano-antennas that introduces phase and\or polarization changes thus creating a new wavefront for the transmitted wave (secondary Hygen's surface). Some research has already been done before on using nanostructures such as nanoantennas in order to bend light. These nanoantennas can be of different dimensions and shapes. One such example is the V shaped antenna structures used for light bending [106] and also plasmonic elliptical nanoantennas whose spectral properties have been observed in the visible light region [107, 108]. Since these shapes of nanoantennas have already been researched upon, we will talk about fabricating another array of nanoantennas called the 'C' shaped nanoantennas. These antennas will be covered by a layer of metal-gold. The fabrication technology used here is again NIL although a lot of similar work has already been done using EBL and nanostencil lithography to fabricate the nanostrucutres or nanoantennas for plasmonic behavior [109, 110].

Up till now we have talked about fabricating 2D nano structures using NIL for various applications. In this research project we are aiming to fabricate quasi 3D nanoantennas using NIL as well as obtaining a double layer stack of the nanoantennas where the first layer is embedded in a dielectric. The reason for two layers is that we want to focus on a preliminary application of a polarizer. Therefore, the two layers of metallic C nanoantennas are fabricated with phase discontinuities between them such that at one time the antennas are parallel to one another in both the layers and at other times they are perpendicular to each other. This will be more clear in the schematic of the C shaped antennas shown in figure 7.4 in the next section The reason we chose the shape of a 'C' antenna is due to ease of its fabrication and the current loop the two open ends of the C generate. Also, when fabricating the second layer of C nanoantennas, due to the shape of the designed 'C', there will be at least some point at which the C antenna's will overlap in both the layers which is what we want. Therefore, having a C shape increases the chance of coverage and the overlap between the two layers is less than half the periodicity of the structures. The basic law of light propagation with phase discontinuities is given in the work done by Yu et. al. [111].

The polarizing filter used with most modern cameras is a circular polarizer. The first stage of the polarizer is a linear polarizer which filters out light in a specific direction, then circularly polarizes light before it enters the camera as shown in figure 7.2 [112]. This work has been derived from the research done by Zhao et. al where they show that the coupling between the twisted anistropic strong resonant layers can cause selectivity of one circular polarizer over the other [113]. We are trying to obtain similar polarization selectivity which is strongly dependant on the coupling between our

nanoantennas and using NIL to fabricate these structures which have till now been done by using EBL.

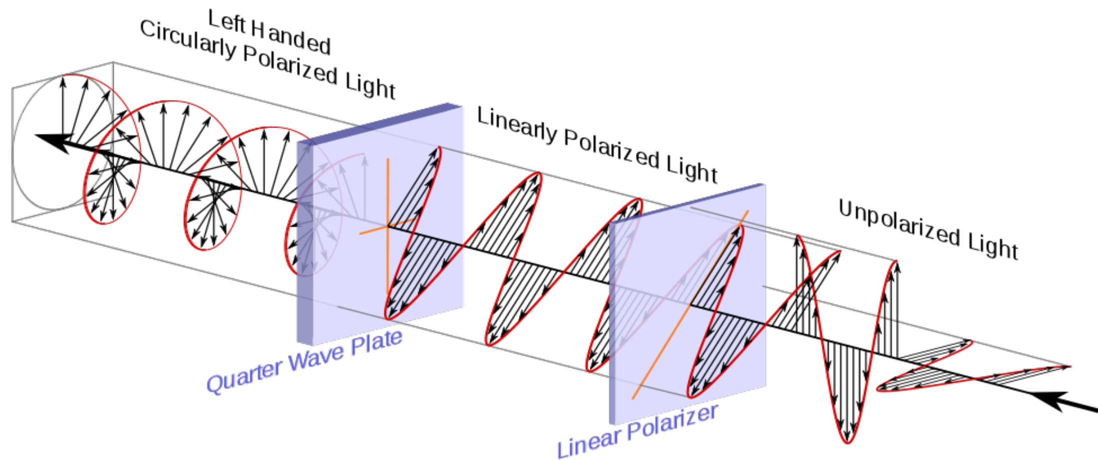

Figure 7.2 Standard circular polarizer

The research presented in this chapter has been done under the supervision of Professor Alexandra Boltasseva of the Birck Nanotechnology Center in Purdue University, Indiana in USA.

7.2 Fabrication Details

As already mentioned above, NIL has been used to fabricate a double layer of 'C' shaped nanoantennas. The two layers of imprinted antennas are separated by a dielectric layer of SU-8. Two different thicknesses of the dielectric spacer have been used- 150 nm and 300 nm in order to observe the coupling between the layers. Figure 7.3 depicts what we meant by a two layer structure of nanoantennas. In this case they are all shown to be aligned parallel to each other. We also fabricated nanoantennas which were twisted by 45° with respect to each other. Figure 7.3 b shows a depiction of the twisted nanoantennas.

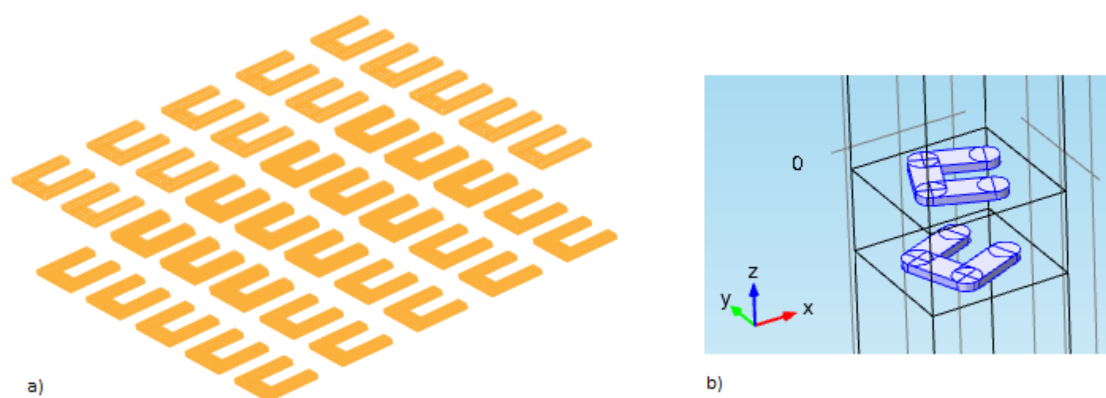

Figure 7.3 a) Double layer quasi 3D 'C' shaped nanoantenna structure b) twisted nanoantenna layers.

Figure 7.4 shows the dimensions of the C antenna which we have fabricated. It consists of 'C' structures placed in a 'L' design on the silicon with two cross marks or alignment marks on the side and bottom of the structures. Each square of structures is 750x750μm in size. Two of these squares have 'C' shaped antennas where one of them has a 'C' which has been rotated by 90° so it looks like a 'U'. This is designed because we want to align the second layer of antennas at 90° with the first one. The dimensions of the individual 'C' antenna is also given in the figure with the arm of the 'C' being 30 nm wide and 150 nm in length. The pitch is 250 nm.

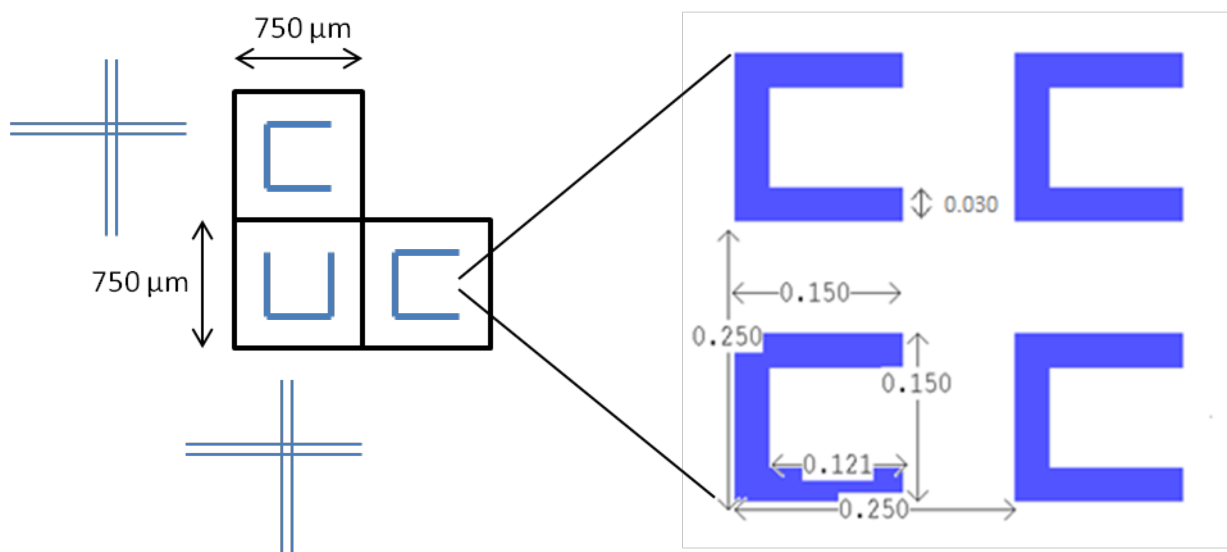

Figure 7.4 The image on the left shows a basic schematic of our stamp design and the dimensions of the individual 'C' antennas.

Certain simulations were also done in order to observe the coupling effect between the two layers depending on the dielectric spacing. Figure 7.5 depicts a graph of simulated spacer thickness dependence on coupling.

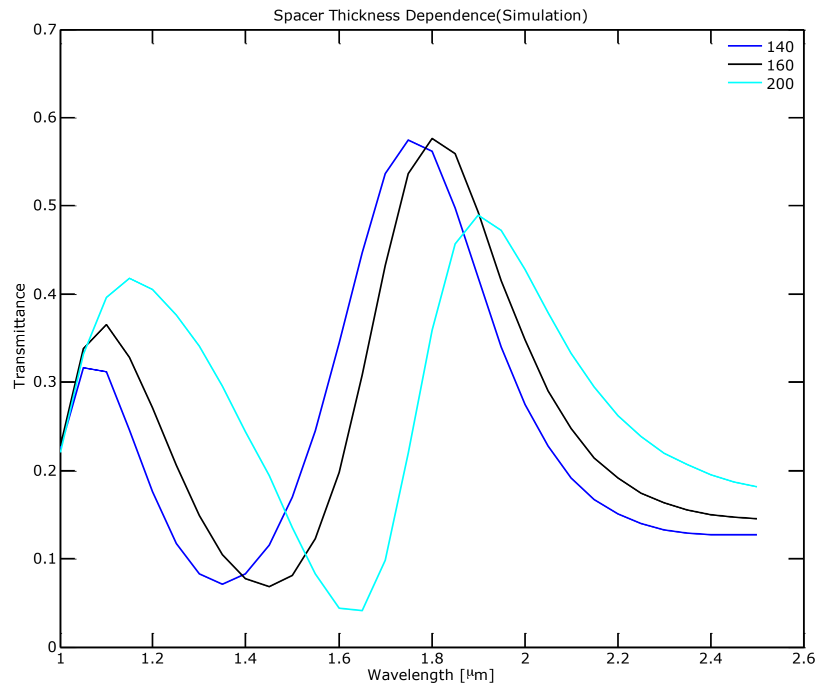

Figure 7.5 Simulation of spacer thickness dependence of coupling between the two layers of antennas.

The fabrication process flow consists of making a stamp first using EBL which will then be used for nanoimprinting. Further processes include removing the residual layer, metal evaporation and finally lift-off to achieve the metal nanoantennas. These will be explained in the following sections.

We use electron beam lithography (EBL) to pattern the desired structures on a silicon wafer. The e-bema resist used is ZEP DR 2.4 spin coated at 2000 rpm for 30 sec and soft baked at 180°C for 2 minutes. This gives an approximate height of 150 nm. The pattern is written in resist coated silicon and then developed for one minute. A metal, usually Alumina is evaporated on top of the written structures and a lift-off is done to remove excess polymer such that only the metallic structures are left behind. In order to have the stamp structures made in silicon, this alumina covered stamp is etched in a reactive ion etcher (RIE) and finally the stamp is cleaned in a piranha solution to remove the left over alumina on top. Finally our stamp is ready to be used for an imprint after coating it

with an anti adhesive layer of fluorocarbons. Figure 7.6 shows an SEM image of the stamp once it is ready for imprinting.

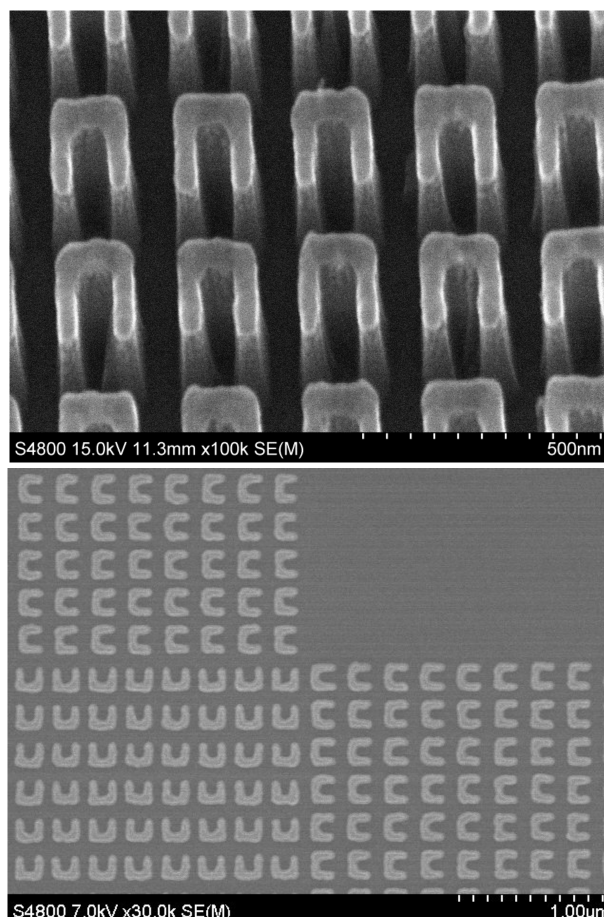

Figure 7.6 SEM images of the stamp once it is ready for imprinting. The height of the structures is 150 nm.

The nanoimprint resist used in this research was NXR 1025 (4% dilution) thermal resist bought from Nanonex. This was spin coated on a silicon wafer at 2000 rpm for 60 seconds and soft baked at 150°C for 2 minutes. This gives a height of approximately 100 nm. The wafer is imprinted with our newly made stamp in a NX-2000 nanoimprinter also bought from Nanonex. The imprint parameters are as follows: pre imprinting for 130°C at 50 psi, the actual imprint happens at 130°C at 300 psi for 3 minutes. The demolding temperature is kept at 50°C. After the imprint, the residual layer is removed by reactive ion etching before doing a metal evaporation. We use gold and titanium yet again- 15 nm of gold and 3 nm of titanium is used. A final step of lift-off is done to obtain the first layer of metallic nanoantennas as shown in figure 7.7.

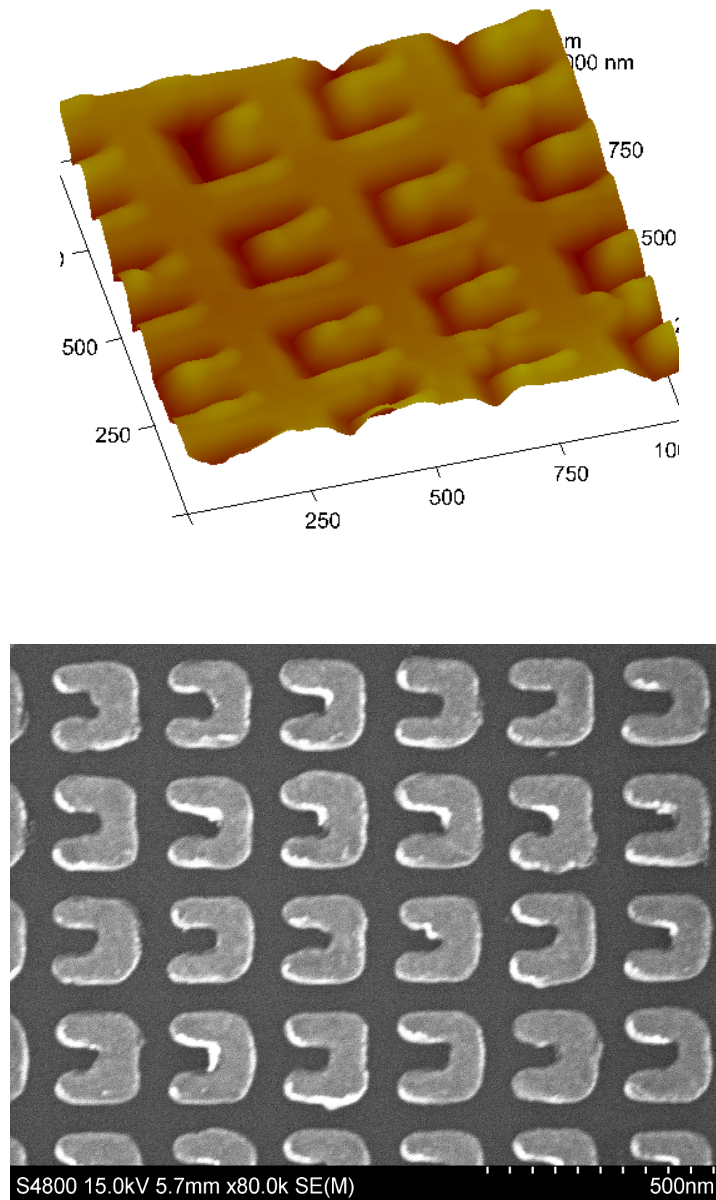

Figure 7.7 Top: AFM image of an imprint Below: first layer of metallic nanoantennas after lift-off.

After the first layer is done, a negative photoresist called SU-8 is used as a dielectric/spacer between the two layers of metallic nanoantennas. The SU-8 is spin coated at 1000 rpm to get a thickness of approx. 150 nm on one sample and a double spin coat at 500 rpm for 45 seconds to get a thickness of approx. 300 nm on another sample. This is then soft baked at 90°C for 1 minute followed by curing of the resist to harden it under UV light exposure for 20 seconds. The samples are baked again at

150°C for 10 minutes in order to complete the SU-8 hardening process. The obtained SU-8 layer is reasonably flat with a surface roughness of 2-3 nm.

The thermal imprint resist NXR 1025 is spin coated yet again for the second layer of imprints. Before performing the next imprint process, a critical step in between is the alignment of the two structured layers with each other such that we get the desired result after the imprint. In one batch of the samples, the nanoantennas of the second layer are aligned parallel to the first layer i.e. at 0° with each other whereas in the other batch, they are aligned at 90° with each other. Since we have used silicon as a substrate, the alignment is done with an infra red microscope whereby one can see through the silicon of the substrate and align the structures with the underlying stamp. This is a very critical step as if the alignment is not done properly, it can lead to discrepancies in the optical measurements. The alignment in this case was done manually which leaves room for human error and is a very slow and tiring process. Therefore, an automatic alignment system would be preferred but due to lack of one in our laboratory we had to do it manually. Figure 7.8 depicts microscopic images of the alignment before and after the imprint in linear as well as perpendicular configuration. An image was taken after the imprint as well just to be sure that the imprint stack does not shift during the imprint process thereby disrupting the alignment.

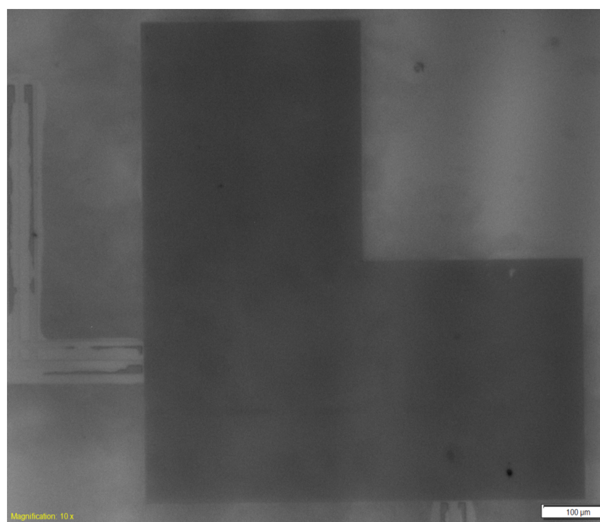

Before imprint

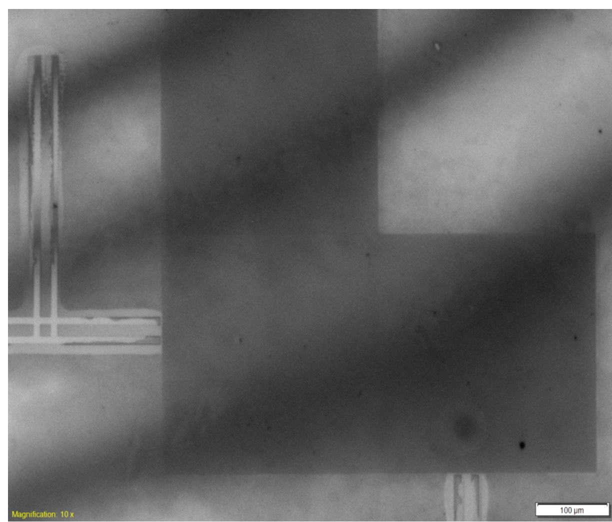

After imprint

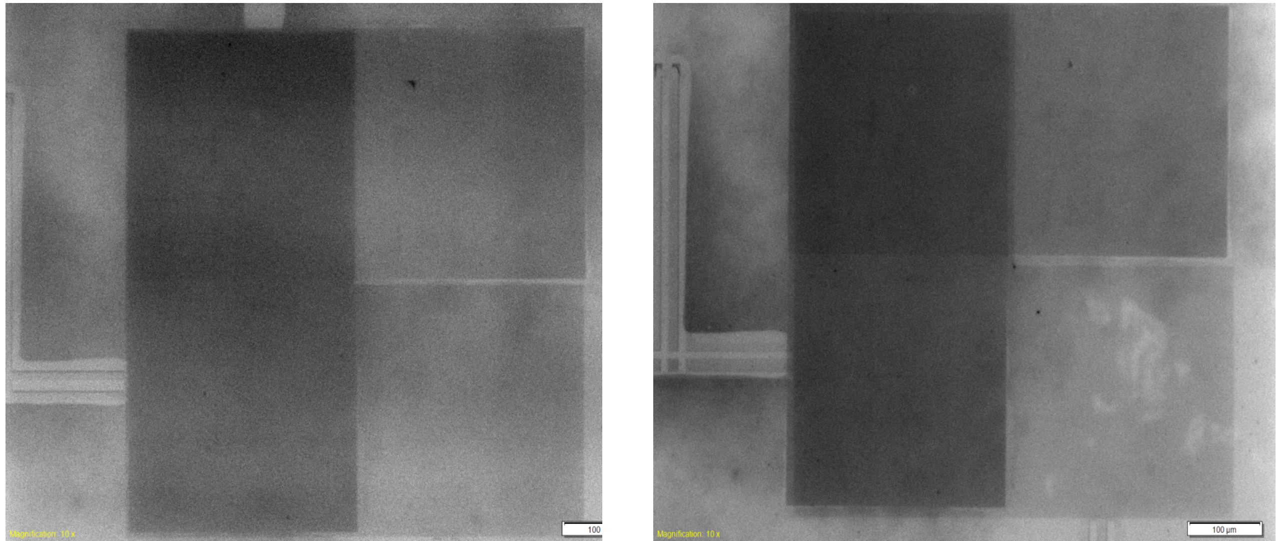

Figure 7.8 IR microscope images showing alignment before and after the imprint. The top two images are for linear configuration whereas the bottom two are for perpendicular configuration..

The same process steps of etching, metallization and lift-off were done to obtain the second layer of nanoantennas. Figure 7.9 shows SEM images of the second layer of metallic nanoantennas. as can be seen from the image, the underlying first layer of nanoantennas is also clearly visible. In the next section we will discuss the optical measurements done on these fabricated samples.

7.3 Results & Discussion

In all of the above experiments, the stamp design and the imprint process underwent a lot of changes in terms of the design, placement of C antennas, SU-8 thickness and also the thermal resist to be used for imprint. After the final nanoantennas were fabricated, some optical measurements were done on them to observe the transmission. The transmission is dependent on the coupling between the two layers which in turn is dependent on the spacer thickness. Figure 7.10 shows the transmission curve measured only after the first layer was fabricated.

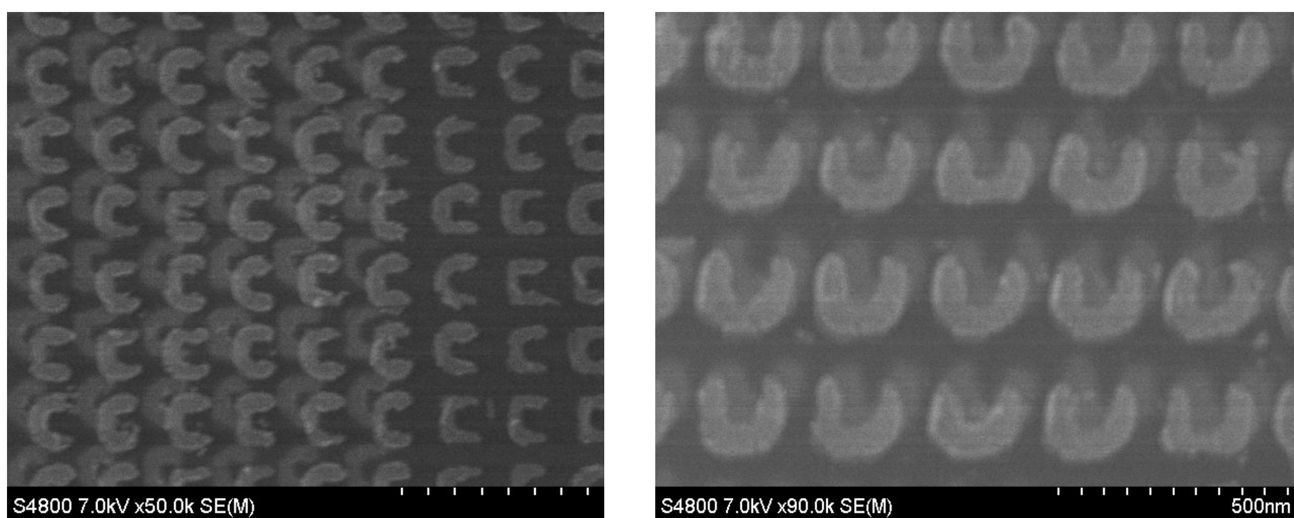

a)

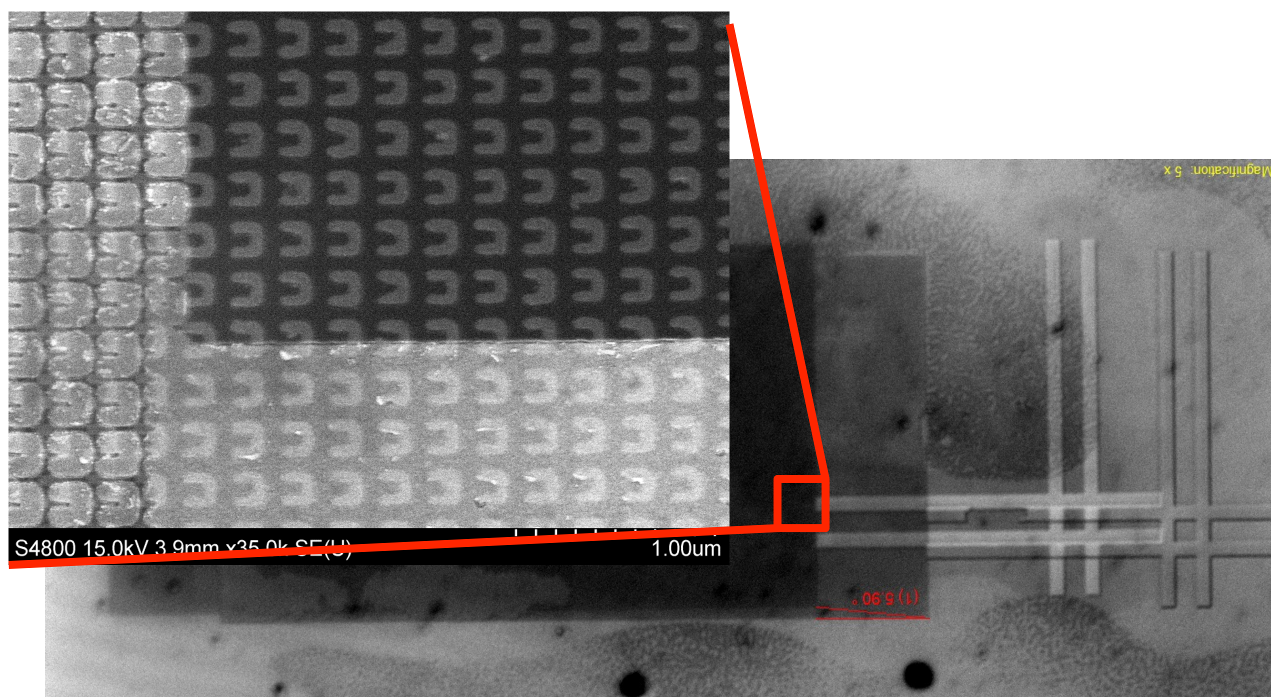

b)

Figure 7.9 a) Image showing the second layer of 'C' shaoed nanoantennas. b) At the interface, the underlying first layer can also be seen.

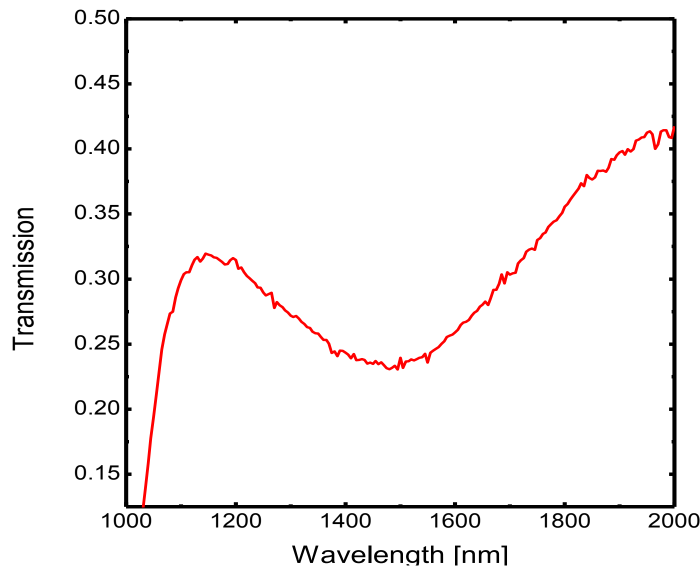

Figure 7.10 Transmission curve obtained after measuring the first layer of ‘C’ antennas.

The electric field is polarized along the gap of the ‘C’ antenna and both the layers have an overlapping ‘C’ orientation. This was another reason for choosing the structure shape as a ‘C’ as it gives us more of an area for an overlap between the two layers of the nanoantennas. FTIR measurements were done later on to get an idea of the optical spectra over a large wavelength region. Figure 7.11 depicts an FTIR graph showing the coupling between the two layers being dependent on the spacer thickness. The two curves are plotted for 150 and 300 nm of SU-8 dielectric.

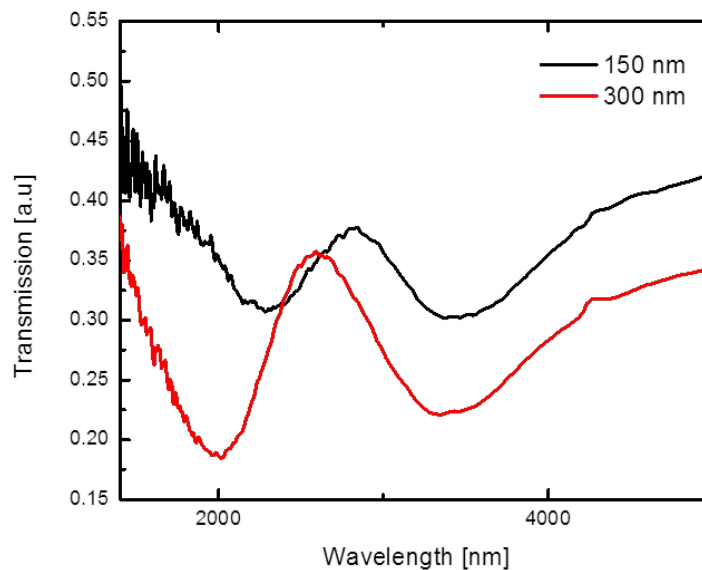

Figure 7.11 FTIR measurements for the coupling between the layers with varying spacer thicknesses.

Figure 7.12 shows three different graphs measuring the transmission and reflectance during the FTIR measurements. As can be seen another spacer thickness of 115 nm was also measured. The lowest transmission is for the 300 nm thick dielectric layer.

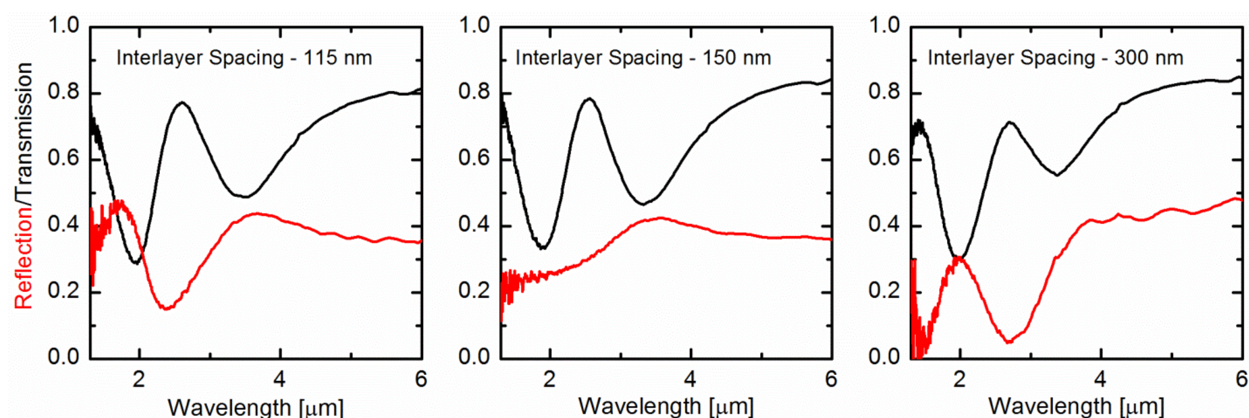

Figure 7.12 FTIR measurements showing the transmission/reflection for different spacer thicknesses.

7.4 Summary & Outlook

Yet another application of NIL has been shown as a polarization rotator. The fabrication of quasi 3D double layer of nanoantenna structures using NIL has been demonstrated. The alignment is a key issue which needs to be improved immensely for further enhancement and near perfect optical measurements. The manual alignment technique gives us an idea of the spectra. Even manually we get an angular alignment of about ~ 5°.

The 'C' antennas are used for their ease of fabrication as well as the advantage it offers in terms of the overlap between the layers. The overlap between the layers was less than half the periodicity of the structures.

Another key issue to be further worked upon is the lateral shift during the actual imprint process. A slight lateral shift is unavoidable in the current setup of the nanoimprinter. An improvement to this setup to avoid this shift would be highly beneficial for all further research on this topic.

We have also shown that the transmission is dependent on the coupling between the two layers of nanoantennas. The coupling in turn is dependent on the spacer thickness

of the SU-8 used. Bigger the spacing, lesser is the coupling and lesser is the transmission.

This work was done in a time frame of 6 months. A lot of improvement and further work can be done on this project given more time. Different structures can be fabricated instead of just 'C' or the previously researched 'V' or elliptical antennas. The dependence on the pitch can also be analyzed. EBL is being used to make layered structures- the same can be done by NIL by making more than a double layer structure. It would be cheaper and result in a higher throughput.

Chapter 8

Conclusion & Outlook

In this chapter, the conclusions to the research work done during the course of the PhD are given as well as some suggestions for future work presented. The main results are highlighted and summarized.

8.1 Conclusion

The entire thesis has been focused on one particular technology used for fabrication which is the Nanoimprint Lithography (NIL). The main advantages of NIL have been highlighted and brought out in terms of various applications explained in detail in the chapters before. It can be understood that NIL is one of the most cost effective, easy to use technology which generates a high throughput. It has been compared to other fabrication techniques as well and its positive aspects pointed out and researched during this thesis. This work is a collaboration of different types of applications in various fields, all falling under the banner of NIL.

One of the first applications explained was the fabrication of nanomagnetic logic (NML) circuits. With the advantages of low power consumption and robustness, NML has great potential in becoming the main technology for logic computation. It has been shown that the combination of NIL with NML could be used eventually at the industrial level due to the combined advantages of low coast and higher throughput.

Another application which was discussed was the fabrication of indium gallium arsenide nanowires using NIL to generate the holes through which the wires are grown in an MBE machine. The type of substrate used was Si/SiO_2 (111). Comparisons between site selective growth and self assembled growth were also shown which pointed in the clear direction that homogenous growth of periodic nanowires is a must to retain all the other properties.

Some optoelectronic applications were also discussed focusing on fabricating metallic grating structures with NIL used in organic photo detectors. Different dimensions and pitches were researched and coverage graphs plotted for the amount of metal covering the substrate to air. The optical spectra were also measured for the grating structures.

Carrying on with the optoelectronic devices, NIL was then used to pattern another organic layer of a photo detector called the PEDOT:PSS layer. Various techniques were analyzed for the same- all different forms of NIL after all. Hard as well as flexible stamps were used and an optimum method explained to pattern the organic layer of PEDOT:PSS which is much less complicated than using the processes mentioned in the literature.

Lastly, NIL in conjunction with metasurfaces has been explained to fabricate quasi 3D double layer of metallic antennas to be used as a polarization rotator. The dependence of transmission on coupling is explained which is in turn dependent on the spacer thickness used. A negative photoresist SU-8 was explained to be used as a dielectric between the two layers whose thickness was varied. Key steps involving the alignment of the two layers before the imprint was also discussed.

8.2 Outlook

There can be a lot of improvements to the above mentioned processes and applications given more time and resources. For example, more work can be done on improving the electrodeposition process for NML fabrication by using a potentiostat which gives a better voltage control. Also by designing stamps which have a better elongated shape instead of rounded which gives a better reading in an MFM imaging.

Instead of using PDMS for the stamp fabrication for optoelectronics applications, it can be replaced by using other chemicals such as ormostamp etc. More research and simulations can be done on the effect of grating structures on PEDOT:PSS films and to understand the optical spectra produced.

As for the metasurfaces application, the main thing to optimize and change would be the alignment system from the current manual one to an automatic one which would greatly lessen the fabrication time as well increase the quality of the layers imprinted. Some other work for future can be designing a different structure instead of a ‘C’ shape and trying to imprint more layers using NIL. Another optimization could be trying to fabricate nanoantennas with not just two spacer thicknesses but a range such that the spacer thickness dependence could be clearly seen.

There are numerous applications of NIL and only a few of them have been researched in the course of this PhD. Nanoimprint lithography can be and in a small way is already being used industrially for production line fabrication. The prospects and advantages far outnumber those of any other fabrication technique currently being used in the market.

References

[1] R. C. Jaeger,“Introduction to Microelectronic Fabrication: Volume 5 of Modular Series on Solid State Devices”, *Prentice Hall*, 2001.

[2] McCord, A. Mark and M. J. Rooks, “SPIE handbook of microlithography, micromachining and microfabrication”, *SPIE, Bellingham*, 2000.

[3] Tseng, K. Chen, C. D. Chen, K. J. Ma, “Electron beam lithography in nanoscale fabrication: recent development”, *IEEE Transactions on Electronics Packaging Manufacturing*, vol. 26, Issue 2, pp. 141-149, 2003.

[4] M. Altissimo, “E-beam lithography for micro-/nanofabrication”, *American Institute of Physics-Biomicrofluidics*, vol. 4, Issue 2, p. 026503, 2010.

[5] Mårtensson, Thomas, et al., “Nanowire arrays defined by nanoimprint lithography”, *Nano Letters,* vol. 4, no. 4, pp: 699-702, 2004.

[6] L. J. Guo, “Recent progress in nanoimprint technology and its applications”, *Journal of Physics D: Applied Physics,* vol. 37, no. 11, pp: R123, 2004.

[7] G. E. Moore, “Cramming more components onto integrated circuits”, *Electronics*, vol. 38, 1965.

[8] M. Malloy and L. C. Litt, “Technology review and assessment of nanoimprint lithography for semiconductor and patterned media manufacturing”, *Journal of Micro/Nanolithography, MEMS and MOEMS*, vol. 10, no. 3, p. 032001, 2011.

[9] S. Y. Chou, P. R. Krauss and P. J. Renstrom, "Nanoimprint Lithography", *Journal of Vacuum Science and Technology B:Microelectronics and Nanometer Structures*, vol. 14, no. 6, pp. 4129-4133, 1996.

[10] S. Y. Chou, P. R. Krauss and P. J. Renstrom, "Imprint of sub-25 nm vias and trenches in polymers", *Applied Physics Letters*, vol. 67, no. 21, p. 3114, 1995.

[11] M. C. McAlpine, R. S. Friedman and C. M. Lieber, "Nanoimprint Lithography for hybrid plastic electronics", *Nano Letters*, vol. 3, pp. 443-445, 2003.

[12] D. Pisignano, L. Persano, E. Mele, P. Visconti, M. Anni, G. Gigli, R. Cingolani, L. Favaretto and G. Barbarella, "First-order imprinted organic distributed feedback lasers", *Synthetic Metals*, vol. 153, pp. 237-240, 2005.

[13] L. J. Guo, "Nanoimprint Lithography: Methods and Material Requirements", *Advanced Materials*, vol. 19, pp. 495-513, 2007.

[14] M. D. Austin et al., "Fabrication of 5 nm linewidth and 14 nm pitch features by nanoimprint lithography", *Applied Physics Letters*, vol. 84, no. 26, 2004.

[15] R. L. Jones, T. Hu, C. L. Soles, E. K. Lin, R. M. Reano, S. W. Pang and D. M. Casa, "Real time shape evolution of nanoimprinted polymer structures during thermal annealing", *Nano Letters*, vol. 6, pp. 1723-1728, 2006.

[16] H. D. Rowland, W. P. King, A. C. Sun and P. R. Schunk, "Simulations of non-uniform embossing: The effect of asymmetric neighbor cavities on polymer flow during nanoimprint lithography", *Journal of Vacuum Science & Technology B: Microelectronics and Nanometer Structures*, vol. 23, no. 6, p. 2958, 2005.

[17] H. D. Rowland, A. C. Sun, P. R. Schunk and W. P. King, "Impact of polymer film thickness and cavity size on polymer flow during embossing: toward process design rules for nanoimprint lithography", *Journal of Micromechanics and Microengineering*, vol. 15, pp. 2414-2425, 2005.

[18] H.–C. Scheer and H. Schulz, "A contribution to the flow behavior of thin polymer films during hot embossing lithography", *Microelectronic Engineering*, vol. 56, pp. 311-332, 2001.

[19] S. Zankovych et al., “Nanoimprint lithography: challenges and prospects”, *Nanotechnology*, vol. 12, no. 2, 2001.

[20] W.-B. Young, “Analysis of nanoimprint lithography with a viscous model”, *Microelectronic Engineering*, vol. 77, pp. 405-411, 2005.

[21] H. Sugimara, A. Hozumi, T. Kameyama and O. Takai, “Organosilane self-assembled monolayers formed at the vapour/solid interface”, *Surface and Interface Analysis*, vol. 34, no. 1, pp. 550-554, 2002.

[22] T. Bailey, B. J. Choi, M. Colburn, M. Meissl, S. Shaya, J. G. Ekerdt, S. V. Sreenivasan and C. G. Willson, “Step and flash imprint lithography: Template surface treatment and defect analysis”, *Journal of Vacuum Science & Technology B: Microelectronics and Nanometer Structures*, vol. 18, no. 6, p. 3572, 2000.

[23] E. L. Hanson, J. Schwartz, B. Nickel, N. Koch and M. F. Danisman, “Bonding self-assembled, compact organophosphonate monolayers to the native oxide surface of silicon”, *Journal of the American Chemical Society*, vol. 125, pp. 16074-80, 2003.

[24] P. Müller-Buschbaum, “Influence of surface cleaning on dewetting of thin polystyrene films”, *The European Physical Journal. E, Soft Matter,* vol. 12, pp. 443-8, 2003.

[25] A. L. Demirel and S. Granick, “Glasslike transition of a confined simple fluid”, *Physical Review Letters*, vol. 77, 1996.

[26] H.-J. Lee, “Effect of initial resist thickness on residual layer thickness of nanoimprinted structures”, *Journal of Vacuum Science & Technology B*, vol. 23, no. 6, 2005.

[27] S. Lan, “Survey on Roller-Type Nanoimprint Lithography (RTNL) Process”, *International Conference on Smart Manufacturing Application*, pp.371-376, 2008.

[28] S. H. Ahn and L. J. Guo, “High-speed roll to roll nanoimprint lithography on flexible plastic substrates”, *Advanced Materials*, vol. 20, no. 11, pp. 2044-2049, 2008.

[29] S. H. Ahn and L. J. Guo, “Large-area roll-to-roll and roll-to-plate nanoimprint lithography: a step toward high-throughput application of continuous nanoimprinting”, *ACS Nano*, vol. 3, no. 8, pp. 2304-2310, 2009.

[30] L. Chen, X. Deng, J. Wang, K. Takahashi and F Liu, “Defect control in anoimprint lithography”, *Journal of Vacuum Science & Technology : Microelectronics and Nanometer Structures*, vol. 23, no. 6, 2933-2938, 2005.

[31] P. Deshpande, X. Sun and S. Y. Chou, “Observation of dynamic behavior of lithographically induced self-assembly of superamolecular periodic pillar arrays in a homopolymer film”, *Applied Physics Letters*, vol. 79, no. 11, pp. 1688-1690, 2001.

[32] S. Y. Chou and L. Zhuang, “Lithographically induced self-assembly of periodic polymer micropillar arrays”, *Journal of Vacuum Science & Technology B: Microelectronics and Nanometer Structures*, vol. 17, no. 6, pp. 3197-3202, 1999.

[33] A. George, D. H. A. Blank and J. E. ten Elshof, “Nanopatterning from the gas phase: high resolution soft lithographic patterning of organosilane thin films”, *Langmuir*, vol. 25, no. 23, pp. 13298-13301, 2009.

[34] M. J. Lee et al., “Antiadhesion surface treatments of molds for high-resolution unconventional lithography”, *Advanced Materials*, vol. 18, no. 23, pp. 3115-3119, 2006.

[35] E. Menard, L. Bilhaut, J. Zaumseil and J. A. Rogers, “Improved surface chemistries, thin film deposition techniques and stamp designs for nanotransfer printing”, *Langmuir*, vol. 20, no. 16, pp. 6871-6878, 2004.

[36] H. Lan and Y. Ding, “Nanoimprint Lithography”, 2010.

[37] K. Walus, G. A. Jullien, and V. S. Dimitrov, “Computer arithmetic structures for quantum cellular automata”, *Conference Record of the Thirty-Seventh Asilomar Conference on Signals, Systems and Computers,* vol. 2, 2003.

[38] D. B. Carlton et al., “Simulation studies of nanomagnet-based logic architecture”, *Nano Letters,* vol. 8, no. 12, pp. 4173-4178, 2008.

[39] G. Csaba, P. Lugli, A. Csurgay, and W. Porod, “Simulation of power gain and dissipation in field-coupled nanomagnets”, *Journal of Computational Electronics*, vol. 4, no. 1-2, pp. 105-110, 2005.

[40] G. Csaba, A. Imre, G. H. Bernstein, W. Porod, and V. Metlushko, “Nanocomputing by field-coupled nanomagnets”, *IEEE Transactions on Nanotechnology,* vol. 1, no. 4, pp. 209-213, 2002.

[41] W. Wu et al., “Large area high density quantized magnetic disks fabricated using nanoimprint lithography” *Journal of Vacuum Science & Technology B: Microelectronics and Nanometer Structures*, vol. 16, no. 6, pp. 3825-3829, 1998.

[42] M. Becherer et al., “Magnetic ordering of focused-ion-beam structured cobalt-platinum dots for field-coupled computing” *IEEE Transactions on Nanotechnology,* vol. 7, no. 3, pp. 316-320, 2008.

[43] M. T. Niemier and P. M. Kogge, “Logic in wire: using quantum dots to implement a microprocessor”, *The 6th IEEE International Conference on Electronics, Circuits and Systems*, vol. 3, 1999.

[44] K. Navi et al., “Five-input majority gate, a new device for quantum-dot cellular automata”, *Journal of Computational and Theoretical Nanoscience,* vol. 7, no. 8, pp. 1546-1553, 2010.

[45] G. Csaba, “*Computing with field-coupled nanomagnets”,* 2003.

[46] A. Imre, “*Experimental study of nanomagnets for magnetic quantum-dot cellular automata (MQCA) logic applications”,* University of Notre Dame, 2005.

[47] D. Young, “Introduction to Magnetochemistry”, Internet Resource.

[48] S. Y. Chou, M. Wei, P. R. Krauss and P. B. Fischer, “Study of nanoscale magnetic structures fabricated using electron-beam lithography and quantum magnetic disk”, *Journal of Vacuum Science & Technology B: Microelectronics and Nanometer Structures*, vol. 12, no. 6, pp: 3695-3698, 1994.

[49] S. Y. Chou, “Patterned magnetic nanostructures and quantized magnetic disks”, *Proceedings of the IEEE*, vol. 85, no. 4, pp: 652-671, 1997.

[50] S. Guan and B. J. Nelson, “Electrodeposition of low residual stress CoNiMnP hard magnetic thin films for magnetic MEMS actuators”, *Journal of magnetism and magnetic materials*, vol. 292, pp: 49-58, 2005.

[51] S. D. Leith and D. T. Schwartz, “High-rate through-mold electrodeposition of thick (> 200 µm) NiFe MEMS components with uniform composition”, *Journal of Microelectromechanical Systems,* vol. 8, no. 4, pp: 384-392, 1999.

[52] S. Getlawi et al., “Patterning of permalloy thin films by means of electron-beam lithography and focused ion-beam milling”, *Superlattices and Microstructures,* vol. 44, no. 4, pp: 699-704, 2008.

[53] S. U. Jen, Y. T. Chen, N. T. Yang and W. C. Cheng, “Mechanical and structural properties of Permalloy films on glass and/or Si (111) substrates”, *Applied Physics A,* vol. 94, no. 2, pp: 431-436, 2009.

[54] S. Sam, G. Fortas, A. Guittoum, N. Gabouze and S. Djebbar, “Electrodeposition of NiFe films on Si (100) substrate”, *Surface science,* vol. 601, no. 18, pp: 4270-4273, 2007.

[55] R. Girard, “The electrodeposition of thin magnetic permalloy films”, *Journal of Applied Physics*, vol. 38, no. 3, pp: 1423-1430, 1967.

[56] J. C. Shin, et al., "$In_xGa_{1-x}As$ Nanowires on Silicon: One-Dimensional Heterogeneous Epitaxy, Bandgap Engineering, and Photovoltaics", *Nano letters,* vol 11, no. 11, pp: 4831-4838, 2011.

[57] S. Hertenberger, et al., "Growth kinetics in position-controlled and catalyst-free InAs nanowire arrays on Si (111) grown by selective area molecular beam epitaxy", *Journal of Applied Physics,* vol. 108, no. 11, pp: 114316-114316, 2010.

[58] W. S. Chang, et al., "Fabrication of free-standing carbon nanotube electrode arrays on a quartz wafer", *Thin Solid Films,* vol. 518, no. 22, pp: 6624-6629, 2010.

[59] Y. Huang and C. M. Lieber, "Integrated nanoscale electronics and optoelectronics: Exploring nanoscale science and technology through semiconductor nanowires", *Pure and Applied Chemistry,* vol. 76, no. 12, pp: 2051-2068, 2004.

[60] C. R. Bolognesi, E. J. Caine, and H. Kroemer, "Improved charge control and frequency performance in InAs/AlSb-based heterostructure field-effect transistors", *Electron Device Letters, IEEE*, vol. 15, no. 1, pp: 16-18, 1994.

[61] Y. Kim, et al., "Influence of nanowire density on the shape and optical properties of ternary InGaAs nanowires", *Nano letters,* vol. 6, no. 4, pp: 599-604, 2006.

[62] S. Hertenberger, et al., "High compositional homogeneity in In-rich InGaAs nanowire arrays on nanoimprinted SiO_2/Si (111)", *Applied Physics Letters,* vol. 101, no. 4, pp: 043116-043116, 2012.

[63] E. Ozbay, "Plasmonics: merging photonics and electronics at nanoscale dimensions", *Science*, vol. 311, no .5758, pp: 189-193, 2006.

[64] H. Ditlbacher, et al. "Organic diodes as monolithically integrated surface plasmon polariton detectors", *Applied physics letters,* vol. 89, no. 16, pp: 161101-161101, 2006.

[65] D. M. Koller, et al. "Organic plasmon-emitting diode", *Nature Photonics,* vol. 2, no. 11, pp: 684-687, 2008.

[66] H. M. Stec, et al. "Ultrathin Transparent Au Electrodes for Organic Photovoltaics Fabricated Using a Mixed Mono-Molecular Nucleation Layer", *Advanced Functional Materials*, vol. 21, no. 9, pp: 1709-1716, 2011.

[67] I. Diukman, et al. "Controlling absorption enhancement in organic photovoltaic cells by patterning Au nano disks within the active layer", *Optics express,* vol. 19, no. 101 pp: A64-A71, 2011.

[68] K. Tvingstedt, et al. "Surface plasmon increase absorption in polymer photovoltaic cells", *Applied Physics Letters,* vol. 91, no. 11, pp: 113514, 2007.

[69] M. Xue, et al. "Absorption and transport enhancement by Ag nanoparticle plasmonics for organic optoelectronics", *Electronics, Communications and Photonics Conference (SIECPC), 2011 Saudi International*. IEEE, 2011.

[70] P. B. Catrysse, and S. Fan, "Nanopatterned metallic films for use as transparent conductive electrodes in optoelectronic devices", *Nano letters*, vol. 10, no. 8, pp: 2944-2949, 2010.

[71] K. Y. Yang, K. C. Choi, and C. W. Ahn, "Surface plasmon-enhanced spontaneous emission rate in an organic light-emitting device structure: Cathode structure for plasmonic application", *Applied Physics Letters,* vol. 94, no. 17, pp: 173301, 2009.

[72] H. Raether, "*Surface plasmons on smooth surfaces",* Springer Berlin Heidelberg, 1988.

[73] W. L. Barnes, A. Dereux, and Thomas W. Ebbesen, "Surface plasmon subwavelength optics", *Nature,* vol. 424, no. 6950, pp: 824-830, 2003.

[74] S. A. Maier, and H. A. Atwater, "Plasmonics: Localization and guiding of electromagnetic energy in metal/dielectric structures", *Journal of Applied Physics,* vol. 98, no. 1, pp: 011101, 2005.

[75] J. Frischeisen, et al., "Light extraction from surface plasmons and waveguide modes in an organic light-emitting layer by nanoimprinted gratings", *Optics Express,* vol. 19, no. 101, pp: A7-A19, 2011.

[76] M-G. Kang, et al., "Organic solar cells using nanoimprinted transparent metal electrodes", *Advanced Materials,* vol. 20, no. 23, pp: 4408-4413, 2008.

[77] G. Scarpa, et al., "Nanoimprint lithography for optical components."*Transparent Optical Networks, 2007. ICTON'07. 9th International Conference on*. Vol. 2. IEEE, 2007.

[78] J. Henzie, et al., "Large-area nanoscale patterning: chemistry meets fabrication", *Accounts of chemical research,* vol. 39, no. 4, pp: 249-257, 2006.

[79] D. Li and L. J. Guo, "Organic thin film transistors and polymer light-emitting diodes patterned by polymer inking and stamping", *Journal of Physics D: Applied Physics,* vol. 41, no. 10, pp: 105115, 2008.

[80] P. G. Taylor, et al., "Orthogonal patterning of PEDOT: PSS for organic electronics using hydrofluoroether solvents", *Advanced Materials,* vol. 21, no. 22, pp: 2314-2317, 2009.

[81] Y. Yang, et al., "Nanoimprinted polymer solar cell", *ACS nano,* vol. 6, no. 4, pp: 2877-2892, 2012.

[82] N. G. Semaltianos, et al., "Picosecond laser patterning of PEDOT: PSS thin films", *Synthetic Metals,* vol. 161, no. 5, pp: 431-439, 2011.

[83] J. Hwang, F. Amy, and A. Kahn, "Spectroscopic study on sputtered PEDOT· PSS: Role of surface PSS layer", *Organic electronics,* vol. 7, no. 5, pp: 387-396, 2006.

[84] X-Y. Deng, "Light-emitting devices with conjugated polymers", *International journal of molecular sciences,* vol. 12, no. 3, pp: 1575-1594, 2011.

[85] J. Ouyang, et al., "High-Conductivity Poly (3, 4-ethylenedioxythiophene): Poly (styrene sulfonate) Film and Its Application in Polymer Optoelectronic Devices", *Advanced Functional Materials,* vol. 15, no. 2, pp: 203-208, 2005.

[86] J. Ouyang, et al. "On the mechanism of conductivity enhancement in poly (3, 4-ethylenedioxythiophene): poly (styrene sulfonate) film through solvent treatment", *Polymer,* vol. 45, no. 25, pp: 8443-8450, 2004.

[87] H. J. Snaith, et al., "Morphological and electronic consequences of modifications to the polymer anode 'PEDOT: PSS'", *Polymer,* vol. 46, no. 8, pp: 2573-2578, 2005.

[88] D. Bagchi and R. Menon, "Conformational modification of conducting polymer chains by solvents: Small-angle X-ray scattering study", *Chemical physics letters,* vol. 425, no. 1, pp: 114-117, 2006.

[89] S. L. Lai, et al., "Concentration effect of glycerol on the conductivity of PEDOT film and the device performance", *Materials Science and Engineering: B,* vol. 104, no. 1, pp: 26-30, 2003.

[90] A. B. Rodriguez et al., "Structure of films of PEDOT:PSS crosslinked with glycerol", *J. Mater. Chem.,* vol. 21, pp: 19324, 2011.

[91] S. L. Lai, et al., "Concentration effect of glycerol on the conductivity of PEDOT film and the device performance", *Materials Science and Engineering: B,* vol. 104, no. 1, pp: 26-30, 2003.

[92] F. Zhang, et al., "Polymer photovoltaic cells with conducting polymer anodes", *Advanced Materials,* vol. 14, no. 9, pp: 662-665, 2002.

[93] K. Efimenko, W. E. Wallace and J. Genzer, "Surface modification of Sylgard-184 poly (dimethyl siloxane) networks by ultraviolet and ultraviolet/ozone treatment", *Journal of Colloid and Interface Science,* vol. 254, no. 2, pp: 306-315, 2002.

[94] H. Schmid and B. Michel, "Siloxane polymers for high-resolution, high-accuracy soft lithography", *Macromolecules,* vol. 33, no. 8, pp: 3042-3049, 2000.

[95] N. Koo, et al., "Improved mold fabrication for the definition of high quality nanopatterns by Soft UV-Nanoimprint lithography using diluted PDMS material", *Microelectronic Engineering,* vol. 84, no. 5, pp: 904-908, 2007.

[96] T. Chen, R. Jordan and S. Zauscher, "Dynamic Microcontact Printing for Patterning Polymer-Brush Microstructures", *Small,* vol. 7, no. 15, pp: 2148-2152, 2011.

[97] S. W. Lee and S. S. Lee, "Shrinkage ratio of PDMS and its alignment method for the wafer level process", *Microsystem technologies,* vol. 14, no. 2, pp: 205-208, 2008.

[98] T-W. Lee, O. Mitrofanov and J. W. P. Hsu, "Pattern-Transfer Fidelity in Soft Lithography: The Role of Pattern Density and Aspect Ratio", *Advanced Functional Materials,* vol. 15, no. 10, pp: 1683-1688, 2005.

[99] U. Lang, “Experimental Methods for Evaluating the Mechanical Properties of Thin Layers of Intrinsically Conductive Polymers”, Dissertation ETH Zurich, DISS. ETH NO. 17754, 2008.

[100] Y. Yang, et al., "Nanoimprint of dehydrated PEDOT: PSS for organic photovoltaics", *Nanotechnology,* vol. 22, no. 48, pp: 485301, 2011.

[101] L. Tan, et al., "Imprinting of polymer at low temperature and pressure", *Journal of Vacuum Science & Technology B,* vol. 22, no. 5, pp: 2486-2492, 2004.

[102] L. Tan, et al., "Plasticizer-assisted polymer imprint and transfer", *Microlithography 2004* International Society for Optics and Photonics, 2004.

[103] C. Birkenstock, "Structuring Polymer Films for Applications in Organic Photovoltaics", Master Thesis, Physik Department, TU München.

[104] W. Cai, V. Shalaev, "Optical Metamaterials", Springer, vol 10, 2010.

[105] D. J. Barber and I. C. Freestone, "An investigation of the origin of the colour of the Lycurgus Cup by analytical transmission electron microscopy", *Archaeometry,* vol. 32, no. 1, pp: 33-45, 1990.

[106] Ni, Xingjie, Naresh K. Emani, Alexander V. Kildishev, Alexandra Boltasseva, and Vladimir M. Shalaev, "Broadband light bending with plasmonic nanoantennas", *Science,* vol. 335, no. 6067, pp: 427-427, 2012.

[107] Liu, Zhengtong, Alexandra Boltasseva, Rasmus H. Pedersen, Reuben Bakker, Alexander V. Kildishev, Vladimir P. Drachev, and Vladimir M. Shalaev, "Plasmonic nanoantenna arrays for the visible", *Metamaterials*, vol. 2, no. 1, pp: 45-51, 2008.

[108] Bakker, Reuben M., Alexandra Boltasseva, Zhengtong Liu, Rasmus H. Pedersen, Samuel Gresillon, Alexander V. Kildishev, Vladimir P. Drachev, and Vladimir M. Shalaev, "Near-field excitation of nanoantenna resonance", *Optics Express*, vol. 15, no. 21, pp: 13682-13688, 2008.

[109] Aksu, Serap, Ahmet A. Yanik, Ronen Adato, Alp Artar, Min Huang, and Hatice Altug, "High-throughput nanofabrication of infrared plasmonic nanoantenna arrays for vibrational nanospectroscopy", *Nano letters,* vol. 10, no. 7, pp: 2511-2518, 2010.

[110] Dickson, W., G. A. Wurtz, P. Evans, D. O'Connor, R. Atkinson, R. Pollard, and A. V. Zayats, "Dielectric-loaded plasmonic nanoantenna arrays: A metamaterial with tuneable optical properties", *Physical Review B,* vol. 76, no. 11, pp: 115411, 2007.

[111] Yu, Nanfang, Patrice Genevet, Mikhail A. Kats, Francesco Aieta, Jean-Philippe Tetienne, Federico Capasso, and Zeno Gaburro, "Light propagation with phase discontinuities: generalized laws of reflection and refraction", *Science,* vol. 334, no. 6054, pp: 333-337, 2011.

[112] Feynman, Richard P., Robert B. Leighton, and Matthew Sands, "*The Feynman Lectures on Physics", Desktop Edition Volume I*. Vol. 1. Basic Books, 2013.

[113] Zhao, Y., M. A. Belkin, and A. Alù, "Twisted optical metamaterials for planarized ultrathin broadband circular polarizers", *Nature communications,* vol. 3, pp: 870, 2012.

Publications

Journal Papers

- M. A. Imtaar, A. Yadav, A. Epping, M. Becherer, B. Fabel, J. Rezgani, G. Csaba, G. H. Bernstein, G. Scarpa, W. Porod, P. Lugli, "Nanomagnet fabrication using Nanoimprint Lithography and Electrodeposition", IEEE Transactions on Nanotechnology, 2013, ISSN: 1536 125X.

- S. Morkötter, S. Funk, M. Liang, M. Döblinger, S. Hertenberger, J. Treu, D. Rudolph, A. Yadav, J. Becker, M. Bichler, G. Scarpa, P. Lugli, I. Zardo, J. J. Finley, G. Abstreiter, G. Koblmüller, "*Role of microstructure on optical properties in high- uniformity In_ {1− x} Ga_ {x} As nanowire arrays: Evidence of a wider wurtzite band gap*", Physical Review B, 2013.

- S. Hertenberger, S. Funk, K. Vizbaras, A. Yadav, D. Rudolph, J. Becker, S. Bolte, M. Döbinger, M. Bichler, G. Scarpa, P. Lugli, I. Zardo, J. J. Finley, M.-C. Amann, G. Abstreiter, G. Koblmüller, "*High compositional homogeneity in In-rich InGaAs nanowire arrays on nanoimprinted SiO2/Si (111)*", Applied Physics Letters, 2012, ISSN: 0003 6951

- G. Scarpa, A-L. Idzko, A. Yadav, S. Thalhammer; "*Organic ISFET Based on Poly (3- hexylthiophene)*", Sensors, 2010, ISSN: 1424 8220

Conference Proceedings

- G. Scarpa, A-L. Idzko, A. Yadav, E. Martin, S. Thalhammer; "*Towards Cheap Disposable Sensing Devices for Biological Assays*", IEEE Transactions in Nanotechnology, 2010, ISSN: 1536 125X

- Anandi Yadav, "*Anode Structuring in OPDs/LEDs Using Nano Transfer Printing*", 11th International Conference on Nanoimprint and Nanoprint Technology, Napa Valley, USA, October 2012- poster presentation.

Miscellaneous

- A. Yadav, "*Nanoimprint lithography as a promising technique for large-scale, high-periodicity growth of III-V nanowires*", TUM-IAS Focus Workshop on Nanowires, Oct 2013.

- A. Yadav, "*Nanoimprinting applications for polymeric devices*", IGSSE Forum Raitenhaslach, 2012

- A. Yadav, *"Entrepreneurship through prototyping and business planning"* ECKART GmbH with UnternehmerTUM, Business Plan, 2011.

- M. Bareiß, M. A. Imtaar, A. Yadav, K. Zhang, A. Hochmeister, B. Fabel, G. Scarpa, W. Porod, G. Koblmüller, G. Abstreiter and P. Lugli, "*Nanotransfer technology for device fabrication"* 4th IGSSE Forum, Raitenhaslach, Germany 2010.

- A. Yadav, M. A. Imtaar, M. Baraiess, G. Scarpa, "*A small scale footprint technology*" IGSSE Forum Raitenhaslach, June 2010.

- A. Yadav, "*Characterization of P3HT Organic Transistors for Biological Applications*", Master Thesis Presentation, Institute for Nanoelectronics, Technical University of Munich, 2009.

Acknowledgements

I would like to start by thanking my principal advisor, Prof. Paolo Lugli for giving me the opportunity to work in his department and be a part of the research group. His interest and encouragement in this cutting edge field led to the successful completion of the work presented in this thesis. I would like to thank him for his immense patience and guidance whenever I needed it. I would also like to thank Dr. Guiseppe Scarpa for being a great mentor by giving me his continuous support in my research and for all the discussions we had.

Moreover, I would like to thank my second advisor, Prof. Wolfgang Porod for his interest in my work and his feedback in the weekly meetings which helped me to do better work. I am extremely grateful to Prof. Alexandra Boltasseva and Prof. Vladimir Shalaev for giving me a wonderful opportunity to work in their research group in Purdue University as a visiting scholar. I would like to thank them for their encouragement and belief in my work.

Needless to say, my friends and colleagues played an important role in the entire research as well and my deepest regard goes to Alaa Abdellah, Ahmed AbdelAzeem, Muhammad Atyab Imtaar, Arsany Basta, Farid Shiekh, Indranil Bose, Sree Harsha Totakura, Garima Chaudhry and Gaurav Yadav for their support and always showing me a good time. I would also like to thank my colleagues in Purdue University, Naresh Emani and Paul West for their valuable discussions and feedback during my research there. Lastly and most importantly I would like to thank my family for their unconditional love, encouragement and faith in me.